ROYAUME DU MAROC
Université Mohammed V - RABAT -
جامعة محمد الخامس – الرباط –
Faculté des sciences
كلية العلوم
CENTRE D'ETUDES DOCTORALES - SCIENCES ET TECHNOLOGIES

N° d'ordre : 3679

THESE

En vue de l'obtention du: ***DOCTORAT***

Structure de Recherche*: Laboratoire de matière condensée et sciences Interdisciplinaires (LaMCScI)*
Discipline: *Sciences de la Matière Physique*
Spécialité: *Physique des matériaux et modélisation des systèmes*

Présentée et soutenue le 17/9/2022 par :
Widad BAZINE

A Monte Carlo simulation and DFT study of physical properties of the Chiral Intermetallic $LaMn_2Si_2$, $TbCu_2Si_2$, Mn_3Sn materials for Magnetic Refrigeration and spintronic applications.

JURY

Mohammed LOULIDI	*PES, Université Mohammed V, Faculté de science Rabat*	*Président*
Abdelmajid EL MANSOURI	*PH, Institut Supérieur des Métiers de l'Audiovisuel et du Cinéma*	*Rapporteur/Examinateur*
Boubker FARES	PH, *Université Mohammed V, Faculté de science Rabat*	*Rapporteur/Examinateur*
Abdeljalil RACHADI	*PH, Université Mohammed V, Faculté de science Rabat*	*Rapporteur/Examinateur*
Abdelaziz MHIRECH	*PES, Université Mohammed V, Faculté de science Rabat*	*Rapporteur/Examinateur*
Najim TAHIRI	*PA, Université Mohammed V, Faculté de science Rabat*	*Co-encadrant de thèse*
Omar EL BOUNAGUI	*PH, Université Mohammed V, Faculté de science Rabat*	*Co-Directeur de thèse*
Hamid EZ-ZAHRAOUY	*PES, Université Mohammed V, Faculté de science Rabat*	*Directeur de thèse*

Année Universitaire: 2021/2022

Acknowledgements

First and foremost, All praises are to almighty ALLAH (SWT) who guides me when I bewilder in the darkness of ignorance and enlighten my ways.

This thesis work has been conducted at the Laboratory of Condensed Matter and Interdisciplinary Sciences (LaMCScI) of the Faculty of Science, University Mohammed V-Rabat under the supervision of Professor ***Hamid EZ-ZAHRAOUY****.*

During my thesis work, I received a lot of support from many people in different ways. I would like to take this opportunity to express my gratitude.

It is my privilege to express my deep sense of gratitude to my Supervisor, Prof. ***Hamid EZ-ZAHRAOUY*** *for his constant persuasion, valuable suggestions, constructive criticism and efficient supervision at each and every stage during my thesis. I would particularly like to thank him for the freedom of action he has given me at every stage of this thesis. I hope that I have been able to prove that I am deserving his trust and that this work is finally fulfilling his expectations.*

I am indebted to Prof. ***Najim TAHIRI*** *and Prof* ***Omar ELBOUNAGUI*** *for his erudite discussion, valuable suggestions and constructive advice throughout the progress of this research work. He was always ready to provide a straightforward explanation of the various concepts involved in the thesis. I thank him for his encouragement and also for his daily good cheerfulness.*

I would like to thank the thesis committee for reviewing my work and giving their insightful and useful comments. It is an honor for me that they agreed to judge this work.

I would like to thank prof. ***Mohammed LOULIDI*** *from Faculty of Science Rabat, who agreed to be the president of the jury members of this thesis.*

I would like to thank prof. ***Abdelmajid EL MANSOURI*** *from Institut Supérieur des Métiers de l'Audiovisuel et du Cinéma, for reporting and reviewing this thesis.*

I would like to thank prof. ***Boubker FARES*** *from Faculty of Science Rabat, for reporting and reviewing this thesis.*

I would like to thank prof. ***Abdeljalil RACHADI*** *from Faculty of Science Rabat, for reporting and reviewing this thesis.*

I would like to thank prof. ***Abdelaziz MHIRECH*** *from Faculty of Science Rabat, for reporting and reviewing this thesis.*

I would like to express my apologies to anyone that I did not mention his name.

Thank you all for your support without expecting any return

DEDICACES :

Je dédie ce travail :

A ma très chère maman

Ma plus profondeur des sentiments que i'éprouve pour vous, vous m'avez tot donné sans compter. Ma plus grande supportrice, aucune dédicace très chère maman, ne pourait exprimer la amour éternel, votre générosité exemplaire et votre présence constante ont fait de moi ce que studes, vous n'avez pas cessé de me soutenir et de m'encourager, vos prières pour moi, Votre grâce a vous, ce travail a pu avoir lieu, grâce à vous, je deviens Docteur. Tout au long de mes je suis aujourd'hui. Puisse dieu, tout puissant vous comble de santé de bonheur et vous procure une longue vie.

A mon très cher père

En témoignage de ces années de sacrifices, de sollicitudes, d'encouragement et de prières. j'espère réaliser D'un de tes rêves. Aucune dédicace ne saurait exprimer mes respects, ma reconnaissance et mon profond amour. Puisse dieu te préserver et te procurer santé et

A ma sœur Hasnaa

Ces quelques lignes, ne sauraient traduire le profond amour que je te porte. Ta bonté tor précieux soutien, ton encouragement tout au long de mes années d'étude, ton amour et ton affection, ont été pour moi l'exemple de persévérance. Je trouve en toi le conseil du frère et le soutien de l'ami. Que ce travail soit T'expression de mon estime pour toi et que Dieu te protège, t'accorde santé, succès et plein de bonheur dans ta vie.

A mes collèges

Je vous dedie ce travail en témoignant des souvenirs passés ensemble. A tous ceux qui me sont chers, que je n'ai pas cité, mais je n'ai pas oublié.

Abstract:

Multiferroic materials have attracted a lot of interest from researchers around the world due to the properties of ferroelectricity, ferromagnetism, and ferroelasticity which are used in many technological, domestic, and industrial applications. Intermetallic are internationally recognized due to their many advantages of being non-toxic, less expensive, and low density. The present work focused on intermetallic "RT_2X_2" (R=rare earth, T= transition metal, and X= Si or Ge) and intermetallic Mn_3Z (Z=Ga, Sn or In). In the first part, we studied the structural, electronic, transport, magnetic and magnetocaloric properties of RT_2X_2 compounds with a combination of density functional theory and Monte Carlo simulation, the results obtained show this material can be used as a thermomagnetic regenerator because it benefits from a strong thermoelectric effect. Or as a rotating refrigerator due to the strong anisotropy. The second part is devoted to the study of the electronic, magnetic, ferroelectric, optical, and magneto-optical properties of Mn_3Z materials (Z=Ga, Sn, or In) using several method such as collinear density functional theory, non-collinear and phonon calculations. The purpose of this part is to perform non-collinear calculations to study the Dzyaloshinskii-Moriya interaction by introducing a strain effect in a thin film for the hexagonal ferrimagnetic Mn_3Sn. Furthermore, we present the results of the effect of non-collinear magnetism on the evolution of the magneto-optical effect.

Keywords: intermetallic, density functional theory, Monte Carlo simulation, thermomagnetic regenerator, Dzyaloshinskii-Moriya interaction, magneto-optic.

Résumé :

Les matériaux multiferroïques ont suscité beaucoup d'intérêt de la part des chercheurs du monde entier en raison des propriétés de ferroélectricité, ferromagnétisme, ferroélasticité qui sont utilisé dans de nombreuses applications technologiques, domestique et industrielles. Les intermétalliques sont reconnu à l'échelle international en raison de ces nombreux avantage étant non toxique, moins chères et de faible densité. Le présent travail s'est concentré sur les intermétalliques "RT_2X_2" (R=terre rare, T= métal de transition et X= Si ou Ge) et les intermétalliques de type Mn_3Z (Z=Ga, Sn ou In). Dans la première partie nous avons étudié les propriétés structurelles, électroniques, transport, magnétiques et magnétocaloriques des composé de type RT_2X_2 grâce à une combinaison d'étude théorie de la fonctionnelle de la densité et la simulation de Monte Carlo, les résultats obtenue montre que ce type des matériaux peut être utilisé comme un régénérateur thermomagnétique dû qu'il bénéfice d'un important effet thermoélectrique. Ou comme réfrigérateur tournant grâce à l'anisotropie importante qu'il possède. La seconde partie est consacré à l'étude des propriétés électronique, magnétique, ferroélectrique, optique et magnéto-optique des matériaux de type Mn_3Z (Z=Ga, Sn ou In) grâce à l'étude théorie de la fonctionnelle de la densité colinéaire, non colinéaire et calculs de phonons. Le but de cette partie est de réaliser des calculs non colinéaires pour étudier l'interaction Dzyaloshinskii-Moriya en introduisant un effet de déformation dans une couche mince pour le ferrimagnétique hexagonal Mn_3Sn. De plus, nous présentons les résultats de l'effet du magnétisme non colinéaire sur l'évolution de l'effet magnéto-optique.

Mots clés : intermétallique, théorie de la fonctionnelle de la densité, la simulation de Monte Carlo, régénérateur thermomagnétique, l'interaction Dzyaloshinskii-Moriya, magnéto-optique.

Résumé détaillé:

Les composés intermétalliques, qui ont de nombreuses applications utiles, sont définis comme une classe de composés impliquant des combinaisons de métaux et ayant des compositions définies et des structures ordonnées. Ils peuvent également inclure des combinaisons avec des métalloïdes ou des non-métaux (à condition qu'ils soient un composant mineur) tels que certains des éléments des groupes 13 et 14. Une classe intéressante de composés intermétalliques contient des combinaisons de terres rares et de métaux de transition, car les interactions complexes des électrons f et d peuvent conduire à des propriétés physiques intéressantes. Les matériaux à base intermétallique de terres rares ont été considérés comme une technologie mature nécessitant dans le domaine de la réfrigération magnétique ou spintronique. Bien que les composés intermétalliques aient eu un grand succès dans le domaine de la réfrigération, en raison de nombreux phénomènes intéressants qui les caractérisent tels que la supraconductivité, le magnétisme, la valence mixte, les fermions lourds et le comportement de kondo [14,15]. Ce type de structure forme un système multicouche naturel où les plans des ions de terres rares sont séparés des couches de métaux de transition. Par conséquent, les aimants sans terres rares ont suscité l'intérêt des groupes de recherche du monde entier en raison de ces nombreux avantages étant non toxiques, moins coûteux et à faible densité. L'objet principal de cette thèse est l'étude des propriétés du matériau magnétique frustré dans le but de comprendre l'origine de cet effet et l'application de ce matériau dans l'industrie en utilisant plusieurs méthodes théoriques telles que la théorie fonctionnelle de la densité et la simulation de Monte Carlo.

Cette thèse est présentée en deux grandes parties : La première partie concerne l'état de l'art et les concepts de base, qui contient deux chapitres :

- ***Chapitre 1 :*** Une introduction générale au magnétisme et les lignes directrices nécessaires pour comprendre et étudier les matériaux intermétalliques pour des applications possibles sont présentées dans ce chapitre.
- ***Chapitre 2:*** Ce chapitre se concentre, dans la première partie, sur le contexte nécessaire des méthodes de calcul, en particulier la théorie fonctionnelle de la densité, la théorie fonctionnelle de la densité d'un aimant non colinéaire et la simulation de Monte Carlo pour les calculs des propriétés structurelles, électroniques et magnétiques qui sont réalisés dans ce travail de thèse.

La deuxième partie concerne les résultats théoriques obtenus, présentés en trois chapitres :

- ***Chapitre 3:*** Dans ce chapitre, nous visons à étudier les propriétés structurales, électroniques, magnétiques et magnétocaloriques du composé intermétallique $TbCu_2Si_2$, en utilisant des méthodes théoriques telles que : Théorie de la Fonctionnelle de la Densité et Simulation de Monte Carlo. Les propriétés magnétiques du composé intermétallique $TbCu_2Si_2$ sont décrites par une transition de second ordre de l'état antiferromagnétique (AFM) à l'état paramagnétique (PM) autour de TN ~ 8 K, de plus, l'effet magnétocalorique géant a été observé sous l'application d'un champ magnétique de h =2.0T. Les valeurs maximales du changement d'entropie magnétique et de la puissance de refroidissement relative (RCP) sont respectivement de 40,78 J/Kg.K et 71,58 J/K. Cependant, les propriétés magnétocaloriques trouvées dans ce composé sont meilleures par rapport à celles du gadolinium [23]. Pour cette raison, ce matériau pourrait être proposé comme un bon candidat pour les applications de réfrigération magnétique autour de la température de Néel T_N.
- ***Chapitre 4:*** Le chapitre vise à étudier les propriétés magnétiques, magnétocaloriques et de transport dans le composé intermétallique $LaMn_2Si_2$ en utilisant des calculs Ab-

initio et Monte Carlo. Le composé intermétallique $LaMn_2Si_2$ est décrit par des transitions de second ordre de l'état ferromagnétique (FM) à l'état paramagnétique (PM) autour de TC ~ 319K, de plus, l'effet magnétocalorique géant a été observé sous l'application de différents champs magnétiques. Alors que les valeurs maximales du changement d'entropie magnétique et de la puissance de refroidissement relative (RCP) sont de 3,34 J/Kg.K et 127,3 J/K à h=7,0 T, respectivement. Cependant, les propriétés magnétocaloriques de ce composé sont meilleures par rapport à celles des études expérimentales [16] et les résultats indiquent que le modèle anisotrope de Heisenberg peut être utilisé avec compétence pour étudier le magnétique et le magnétocalorique des alliages non colinéaires.

- ***Chapitre 5:*** Le but de ce chapitre est d'effectuer des calculs non colinéaires pour étudier l'interaction Dzyaloshinskii-Moriya en introduisant un effet de déformation dans une couche mince pour le ferrimagnétique hexagonal Mn_3Sn. En outre, l'effet des contraintes de traction et de compression sur les propriétés structurelles, électroniques, magnétiques, ferroélectriques, optiques et magnéto-optiques du composé Mn_3Sn. Tout d'abord, les calculs des premiers principes révèlent un énorme effet ferroélectrique avec un comportement métallique. Deuxièmement, nous effectuons une analyse de l'effet Kerr magnéto-optique (MOKE) sur une couche mince, un effet MOKE important a été trouvé dans un état fondamental antiferromagnétique (AFM) suivant la direction [001] qui est en bon accord avec les études expérimentales. Nos résultats améliorent la compréhension théorique des interactions Dzyaloshinskii–Moriya (DM) induites par un grand effet Kerr magnéto-optique (MOKE). En outre, la relation entre ferroélectrique et ferromagnétique a été étudié et devrait fournir une base pour l'application expérimentale de dispositifs spintronique basés sur l'effet Hall anormal.

List of Publications:

Articles Accepted:

1- Bazine, W., Tahiri, N., El Bounagui, O., Ez-Zahraouy, H., Benyoussef, A., 2019. Structural, electronic, magnetic, and magnetocaloric properties in intermetallic compound $TbCu_2Si_2$. Journal of Magnetism and Magnetic Materials 481, 72–76. https://doi.org/10.1016/j.jmmm.2019.02.095

2- W. Bazine, N. Tahiri, O. El Bounagui & H. Ez-Zahraouy (2022) Magnetic, magnetocaloric and thermoelectric properties of the intermetallic $LaMn_2Si_2$ compound: a theoretical study, Phase Transitions, 95:5, 387-397, DOI: 10.1080/01411594.2022.2054808

3- W. Bazine, N. Tahiri, O. El Bounagui & H. Ez-Zahraouy (2022) Strain effect on physical properties of the multiferroic Mn_3Sn material: a first-principles calculations, Philosophical Magazine, DOI: 10.1080/14786435.2022.2043565

List of Table:

List of Figures :

List of abbreviations:

AFM antiferromagnetic

FM ferromagnetic

PM paramagnetic

SG spin glass

FE ferroelectric

PE paraelectric

FiM ferrimagnetic order

MOKE magneto-optical Kerr effect

MO magneto-optical

AHE anomalous Hall effect

ANE anomalous Nernst effect

TAHE terahertz anomalous Hall effect

PHE planar Hall effect

THE topological Hall effect

T_N Néel temperature

T_c Curie temperature

DMI Dzyaloshinskii-Moriya interactions

NCM non-collinear calculations

NC non-collinear

HES Heisenberg exchange interaction

MAE magnetocrystalline anisotropy

SOC spin-orbit coupling

MC Monte Carlo simulation

ΔS_M Magnetic entropy change

RCP relative cooling power

SU spin up

SD Spin down

DFT Density functional theory

KK Kramers-Kronig relation

KKR Korringa-Kohn-Rostoker

EC exchange-correlation

E_{xc} exchange and correlation energy

KSE Kohn-Sham equation

KS Kohn-Sham

EP effective potential

NR non-relativistic

SR scalar-relativistic

SEI super-exchange interaction

DEI double exchange interaction

FSM "fixed spin" approach

Table of Contents

CHAPTER 5: STRAIN EFFECT ON PHYSICAL PROPERTIES OF THE MULTIFERROIC MN3SN MATERIAL: A FIRST-PRINCIPLES CALCULATIONS

General Introduction

A growing requirement for speedier information retrieval and bigger storage capacity has pushed the quest for quicker and cheaper electronic equipment devices. Under these conditions, the spintronic technologies anticipated to offer speed, high density, and reduced consumption of energy, it provide a viable replacement for the CMOS processes . The most important technological domain where we anticipate significant effects of Spintronics, mainly after current-induced spin-orbit matching [1, 2], is the memory sector [3], wherein the topological spin structures like chiral field wall and especially skyrmions [4, 5] represent an exciting opportunity to support data in low power systems. However, the essential factor required for the stabilization of these exotical Chiral structures is the so-called interfacial Dzyaloshinskii-Moriya interaction (iDMI), which consists of antisymmetric exchange interactions associated to spin-orbit coupling (SOC) between nearby spins.

In this thesis the rare earth intermetallic based material has been considered as a mature technology that requires in spintronic or magnetic refrigeration. Although, Intermetallic materials have enjoyed considerable popularity in the cooling domain owing to several exciting characteristics which include superconductivity, magnetism, mixed valence, heavy fermions, and kondo behavior [14,15]. This kind of structure is formed by a natural layered arrangement where rare-earth ion planes are spaced from transition metal layers.

Therefore, rare earth free magnets have taken the interest of research groups worldwide due to these many advantages being non-toxic, less expensive and low density.

The main objet of this thesis is the study to properties of the chiral magnetic material in the intention to understand to origin of this effect and the application of this material in the industrial by using several theoretical methods such as DFT and MC.

This thesis is presented in two main parts:

The first part concerns the state of the art and basic concepts, which contains two chapters:

- ✓ ***Chapter 1:*** A general introduction to magnetism and the necessary guidelines to understand and study intermetallic materials for possible applications are presented in this chapter.
- ✓ ***Chapter 2:*** This chapter focuses, in the first part, on the needed background of the computational methods, especially, DFT of a noncollinear magnet and MC for the calculations of the structural, electronic and magnetic properties that are performed in this thesis work.

The second part concerns the obtained theoretical results, presented in three chapters:

- ✓ ***Chapter 3:***

In this chapter, we have investigated the structural, electronic, magnetic and magnetocaloric properties of the intermetallic compound $TbCu_2Si_2$, applying theoretical techniques including density function theory and MC. The magnetic properties of the intermetallic compound $TbCu_2Si_2$ were determined through a second order transition from its AFM state into the PM state near T_N ~8 K. In addition, the giant magnetocaloric effect was found under a magnetic field at h=2T. The highest values of ΔS_M and RCP were found to be 40.78J/Kg.K and 71.58J/K, respectively. On the other hand, the magnetocaloric properties obtained for this compound are best in comparison with those of gadolinium [23]. Based on this reason, it may be proposed as a suitable choice for applications in magnetic refrigeration near T_N.

- ✓ ***Chapter 4:***

The purpose of this chapter is to study the magnetic, magnetocaloric and transport properties of the intermetallic compound $LaMn_2Si_2$ through the use of Ab-initio and Monte Carlo calculations. The intermetallic compound $LaMn_2Si_2$ has been described by second-order transitions between the FM and PM states around T_C~319K, as well as a large magnetocaloric

effect being observed under applying various magnetic fields. The highest values of ΔS_M and RCP are 3.34 J/Kg.K and 127.3 J/K at h=7.0 T, respectively. On the other hand, the magnetocaloric properties obtained for this compound are improved over the experimental studies [16] and the findings suggest that the Heisenberg anisotropic model may be appropriately employed for studying the magnetic and magnetocaloric properties of NC alloys.

- ✓ ***Chapter 5:***

The objective of this chapter is to perform NCM in order to study the DMI introducing a strain effect in thin film for the FiM hexagon Mn_3Sn. Furthermore, we have investigated the effect of tensile and compressive stress on the structural, electronic, magnetic, FE, optical and MO properties of the Mn_3Sn compound. To begin with, first-principles calculations revealed an enormous ferroelectric effect with metallic behaviour. Secondly, we carry out an analysis of MOKE at the stained thin film, a significant MOKE effect were found in the AFM ground state AFM following the [001] direction, which agrees well with experimental investigations. The present results enhance a theoretical comprehension of DMI interactions leading to a large MOKE. Furthermore, the relationship between FE and FM was investigated and is expected to give a foundation for experimental applicability of spintronic mechanisms which are based on AHE.

CHAPTER 1:
State of the art and basic concepts

Introduction:

Intermetallic compounds, which have numerous useful applications, are defined as a class of compounds involving combinations of metals and having definite compositions and ordered structures. They can also include combinations with metalloids or nonmetals (provided that they are a minor component) such as some of the group 13 and 14 elements. An interesting class of intermetallic compounds contains combinations of rare-earth and transition metals, because the complex interactions of f- and d- electrons can lead to interesting physical properties, such as magnetism, heavy fermion behaviour, and superconductivity.[1] For example, U_2RhSi_3 exhibits long-range ferromagnetism below 24 K, $CeCoIn_5$ shows heavy-fermion superconductivity, and $CeCu_2Si_2$ is superconducting. The bonding in intermetallic compounds can also be quite diverse. [2-4] Given the large number of metallic elements in the periodic table, there are many intermetallic compounds that remain to be discovered, which may lead to materials with new properties and applications.

1- Study of the intermetallic RT_2X_2 compound:

Among the variety of materials with first-order transition, most of the intermetallic compounds are the RT_2X_2 family which has received considerable attention in recent years due to its various physical properties [5-9]. Depending on the T and X components, the intermetallic compounds have different phenomena such as superconductivity, complex magnetic ordering properties of Heavy fermion, valence fluctuation, and large MCE [10]. Particularly, the compounds of the RMn_2X_2 family present the coexistence of the 3d (manganese) and 4f magnetic subsystems (from the R ion). Exchange interactions between the R and Mn moments induce multiple transitions and anomalies in the magnetic properties of these materials. Due to their complexity, the magnetic properties of many compounds of this

family are not yet fully elucidated. In addition, another important property of this class of materials is the phenomenon called exchange bias that manifests itself as a shift in the magnetic hysteresis during the cooling process. This feature is due to unidirectional anisotropy in systems with FM ordering interface (FM)/(AFM) or (FM)/(SG). Such behavior makes these materials interesting for applications other than refrigeration magnetic field, for example in devices for spintronics (such as valves and magnetic junction) among others.

1.1- Crystal structure and chemical bonding:

Most RT_2X_2 phase ternary intermetallic materials crystallize in the structure body-centered tetragonal of the $ThCr_2Si_2$ type with space group I4/mmm [5], except for the materials containing Ir and Pt that crystallize in the tetragonal structure of the type $CaBe_2Ge_2$ with group P4/mnm [11]. The unit cells of these structures are illustrated in **Fig. 1**. An important feature of RT_2X_2 compounds that exhibit these structures are the arrangements of atoms in the form of layers, these being composed of rare earth, T, and X elements that are perpendicular to the tetragonal axis c. The sequence R-X-T-X-R-X-T-X-R is observed in $ThCr_2Si_2$ structures, while T-X-R-X-R-X-T is the sequence observed in $CaBe_2Ge_2$-like structures. In the case of the $ThCr_2Si_2$ type structure, adopted by the compounds studied in this work, each atom of R is surrounded by eight atoms of X and eight atoms of T, which are located on each of the edges.

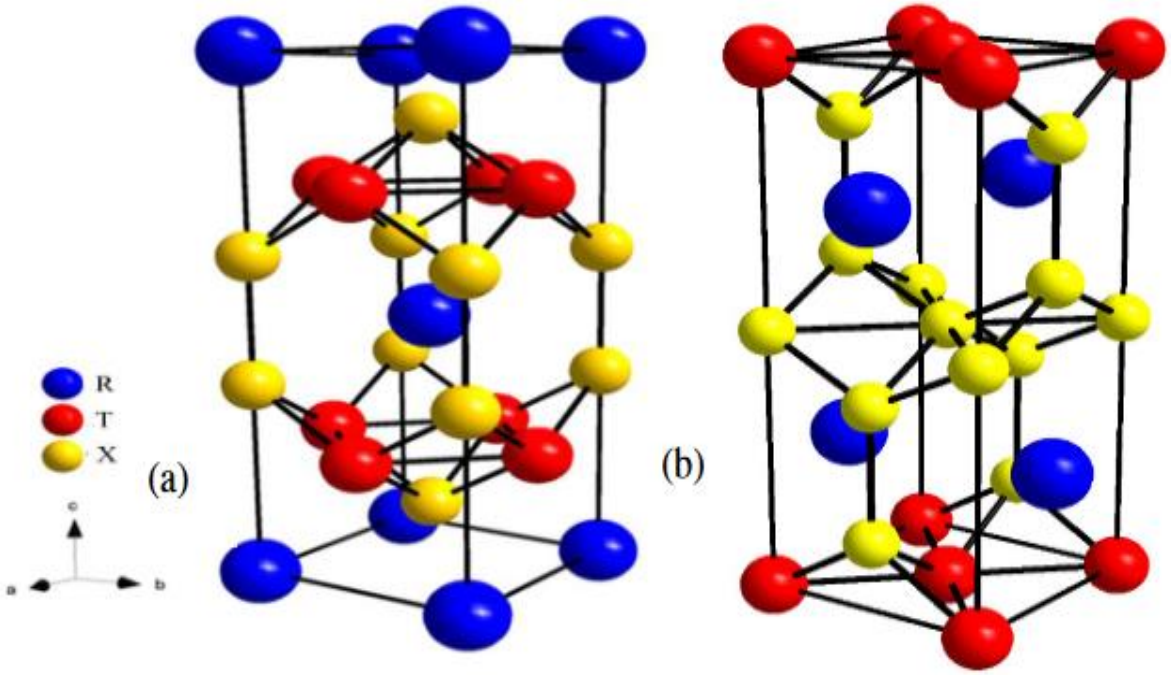

Figure 1: The crystal structure of the types : (a) ThCr2Si2 (b) CaBe2Ge2.

1.2- Magnetic structures:

The neutron diffraction reported in the literature indicates that rare earth or actinides present a wide variety of orders when inserted into compounds of type RT_2X_2. The magnetic structures already determined for this family are shown in **Fig. 2**. We can see in the figure below that in addition to a collinear structure (F, AF I, AF II, AF III, AF IV), there is also the presence of modular structures (LSW I, LSW II and LSW III, LSW IV). For the RT_2X_2 rare earth compounds, we observe the types of magnetic structures mentioned below, some of which retain a defined type of magnetic structure in the temperature region between 0 K and T_N or T_C.

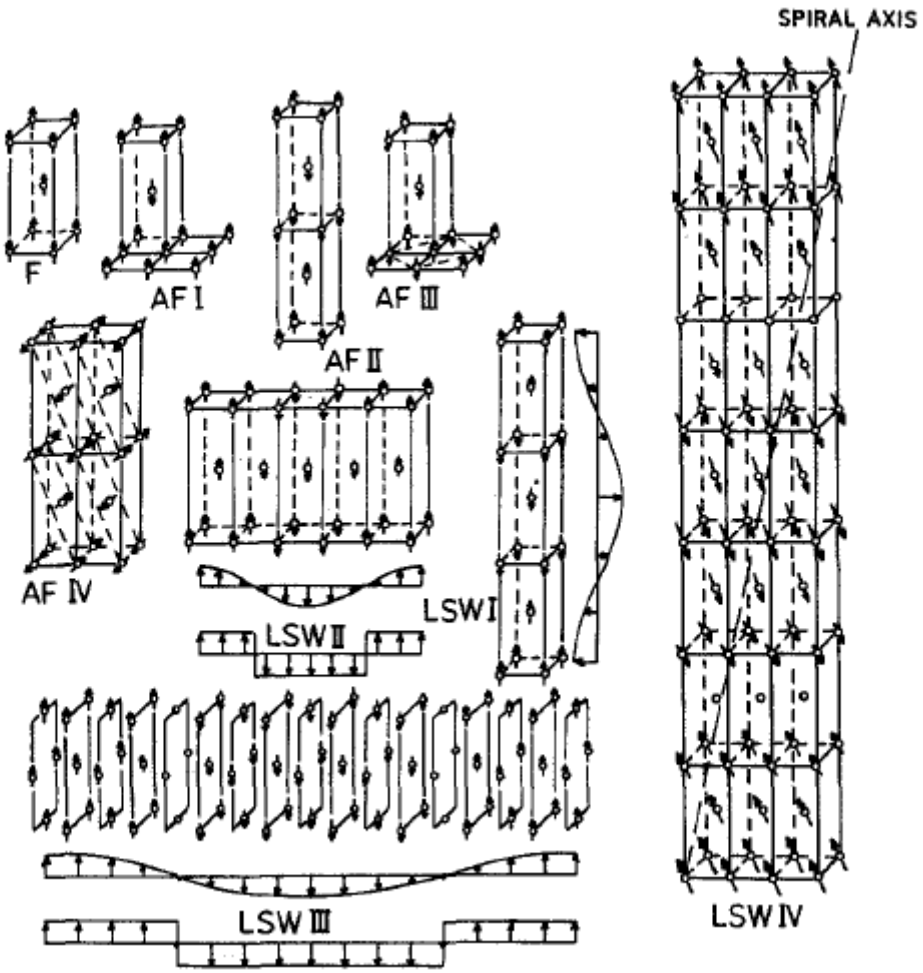

Figure 2: The magnetic structure of the rare earth and actinide sublattice in various RT2X2 compounds

1.3- Super-exchange Interaction (Mn-Si(Ge)-Mn) :

The SEI is an indirect interaction that occurs between the moments of two non-adjacent magnetic ions, so this interaction is mediated through an intermediate non-magnetic ion. For most AFM compounds, the direct exchange interaction is not favorable, as is the case with AFM oxides which are composed of transition metals, but which are separated by large ions of oxygen, so the direct interaction between the d orbitals is very unlikely and the interaction ends up occurring through an intermediary, which in this case would be a p orbital. A schematic diagram to explain this interaction can be seen in **Fig. 3** [12].

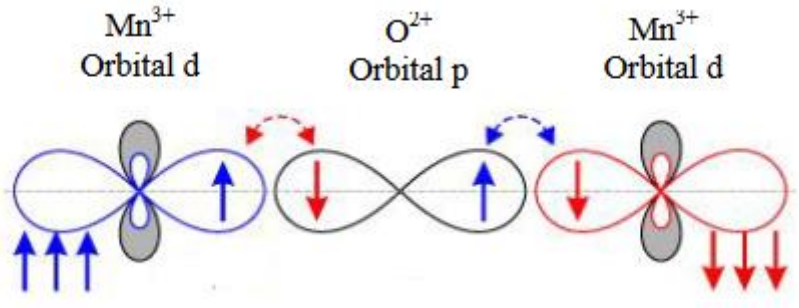

Figure 3: Scheme of the Super Exchange interaction between the d electrons mediated by the p orbital for the MnO compound.

To understand the SEI, one can consider two d orbitals and one p orbital between them, so there can be a jump between the d and p orbitals. when the ions magnets have antiparallel spins, two consecutive jumps occur and can be of two different possible types, and ends up resulting in either an empty p orbital or an empty p orbital. empty d orbital. In the case where the spins are aligned parallel, the process of a second hop does not occur and the orbitals end up being incomplete. **Fig. 4** illustrates schematically this mechanism. [12]

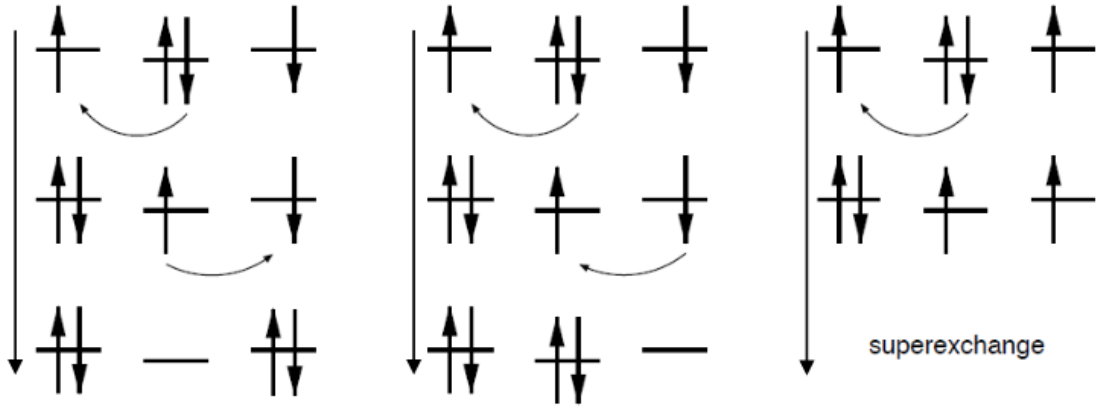

Figure 4: Scheme of the super exchange interaction in the case of magnetic ion spins be aligned antiparallel or parallel.

The SEI depends on the degree of hybridization, the occupation of the d orbitals of the transition metals and the bond angle between the half-filled orbitals. Thus, in the specific case of $RMn_2Si(Ge)_2$ compounds, illustrated in **Fig. 5**, the AFM and FM interaction can be observed. Since the electrons in the d orbital of Mn are mediated by the electrons in the p

orbital of Si or Ge. According to the electron occupancy and bond angle, the coupling can be AFM or FM type.

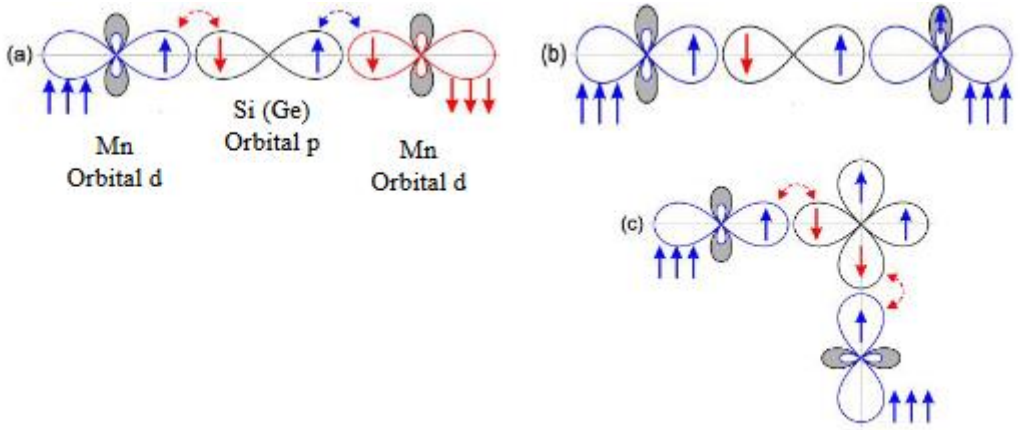

Figure 5: Schematic of bond angle dependence and occupancy for the Super Exchange interaction between the d electrons mediated by the p orbital

In the case where the interaction occurs at an angle of 180, as shown in **Fig. 4**, an AFM interaction would be energetically more favorable, in the case of a perpendicular interaction between the energetically half-filled orbitals is more favorable for the spins to couple ferromagnetically.

1.4- Double exchange interaction ("double exchange") :

The DEI was initially proposed by Clarence Zener [13] to explain the properties of Mn oxide ($LaMnO_3$), and was then reformulated by Anderson and Hasegawa, and De Gennes [14]. This interaction is based on the coupling of ions magnetic fields that have different valences, occurring through the transfer of an electron from the magnetic ion to the non-magnetic central ion and simultaneously to the other magnetic ion of different valence. In the mechanism proposed by Zener, the double exchange involves the transfer of electrons from the Mn^{3+} site to the central oxygen ion and, simultaneously, the transfer of an electron from the oxygen ion to the Mn^{4+} ion site, as can be seen in **Fig .6**.

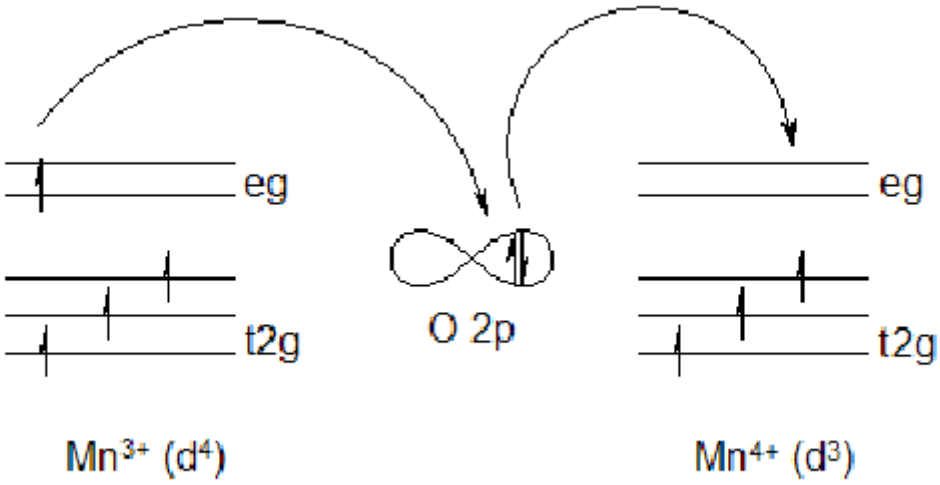

Figure 6: Schematic of the mechanism of the DEI between Mn3+ and Mn4+ ions via oxygen atom proposed by Zener

This mechanism is similar to the super exchange interaction mechanism, but in the super exchange FM or AFM coupling occurs between two atoms that have the same valence, unlike the case of double exchange, which can occur between atoms with different valences. But this mechanism is more favorable if the two Mn ions are ferromagnetically coupled, because the spin of the bouncing electron does not change from one ion to the other ion, favoring the FM ordering.

1.5- Indirect exchange interaction by the RKKY mechanism (Mn-Mn):

The RKKY indirect exchange interaction mechanism was developed by Ruderman and Kittel [15], Kasuya [16], and Yosida [17], and the name RKKY is due to the first letter of the names of these four authors. In general, this mechanism occurs in metals where atoms with well-localized magnetic moments exist, as in rare earth. These atoms polarize the electrons in the electron cloud (conduction electrons) that are next to them, the electrons in this cloud carry the information to another magnetic atom causing it to polarize as well. This interaction is far-reaching and has an oscillatory value with distance, causing the spins to align “up” or “down”, and a FM or AFM interaction may occur. That interaction is indirect because it does not

involve a direct coupling between the moments magnetic. [12, 18]. The polarization of the conduction electrons is maintained for a certain distance in the crystal. Relative to the first magnetic ion, but as electrons move away from it they gradually lose their spin alignment towards the first ion. That the process is repeated each time the conduction electrons pass through the sites Therefore, this polarization will have an oscillatory behavior in the crystal. For the specific case of the Mn ion, the d-shell spins are strongly coupled with the s electrons of the conduction band, thus coupling occurs, as can be seen in the mechanism of **Fig. 7**.

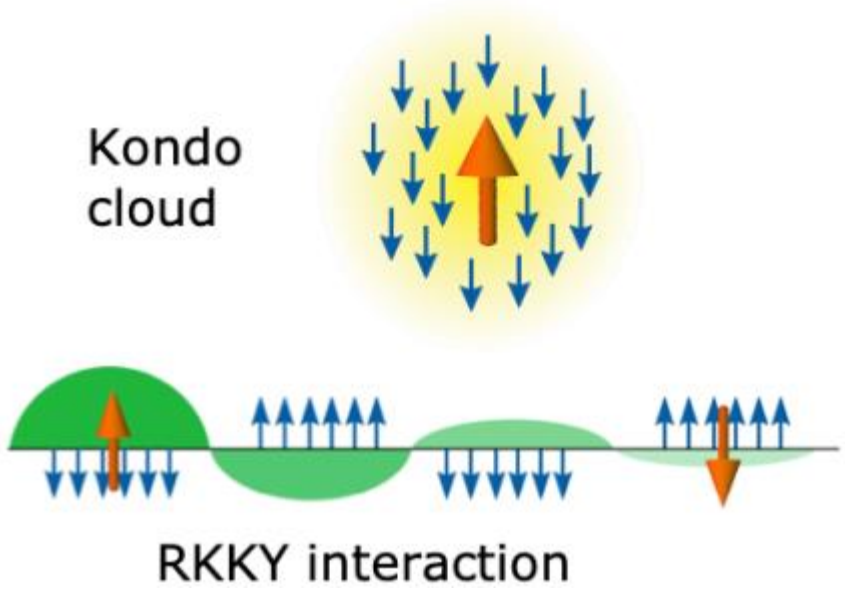

Figure 7:Model representations of indirect Mn-Mn burrow interaction. Interaction FM by RKKY coupling mechanism

The RKKY interaction decays as the moments move away resulting in non-uniform polarization. This polarization is repeated every time the electrons conduction passes through the magnetic sites, resulting in an oscillatory behavior inside the crystal. Thus, depending on the J_{ij} sign, the system can be FM for $J_{ij}>0$ or AFM for $J_{ij}<0$, as can be seen in fig.8 [12, 18].

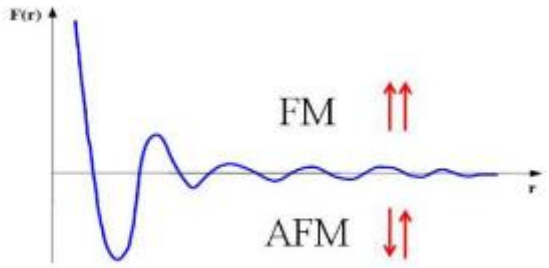

Figure 8: Schematic of the indirect exchange interaction between Mn ions via holes with uniform polarization of carrier ions (RKKY).

1.6- Exchange interaction by Campbell and Brooks model (R-Mn, R-R):

This is an alternative concept that was proposed by Campbell [19] and Brooks [20], it is based on heuristic arguments and first-principles calculations. Campbell and Brooks showed that indirect coupling can be provided by the exchange interaction inter-atomic between the 3d spin moment of a transition metal and a spin moment 5d of a lanthanide and is a ferrimagnetic interaction (fig. 9). Earth's 4f Moment rare is localized and cannot interact directly with its neighbors, but can be produced an intra-atomic FM exchange interaction with the earth's 5d momentum rare. The result is a lattice with FM coupling between the earth's 4f moment rare and transition metal 3d moment. This mechanism can occur for all rare earths except for Lu and Yb, as they are divalent and the 4f moment is zero. That mechanism occurs when an ion that is polarized, by exchange interaction, forces the alignment of the spin of another ion in the same direction as the first, as schematized in **Fig.8**.

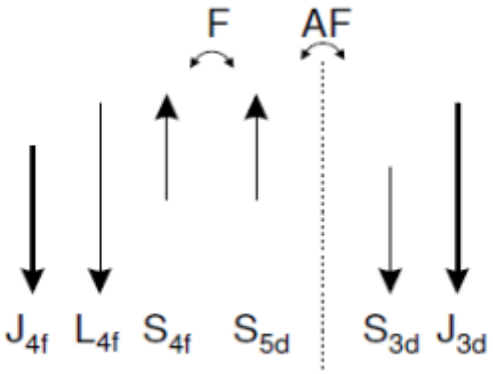

Figure 9: Representation of the model proposed by Campbell and Brooks of coupling intra-atomic 4f-5d FM and inter-atomic 5d-3d AFM between the moments.

1.7- Crystalline field:

In magnetic samples, the effect of the crystalline field interaction is to mix excited states which the ground state, which leads to a reduction at the moment angular. This attenuation effect (called "quenching") causes a reduction in the magnetization and the hyperfine field that acts on the nucleus of the respective ion. Thus, the crystalline field is responsible for removing the degeneracy by decreasing the moment orbital magnetic. Under the influence of the crystalline field, the orientation of the orbitals electronics varies continuously with time, which makes the moment projection orbital null along any direction. Briefly, the crystalline field is the electrostatic field that a crystal lattice creates on ions. This field influences the magnetic properties of materials and their effects are directly related to the crystal lattice symmetry [21].

The interaction of the Crystalline Field is classified into three intensities, as follows: form,

- Strong Crystalline Field Interaction that occurs in the elements of the series of 4d and 5d transition (not the case for this work).
- Average Crystalline Field Interaction that is observed in the 3d series (as in case of Mn). This crystalline field is stronger than the spin-orbit interaction and less

important than the interaction between the valence electrons of the free ion. For the specific case of Mn, the degeneration or separation of the crystalline field depends on the number of electrons in the d orbital, the oxidation state of the metal, and the arrangement of ligands around the metal ion. Mn has electrons that orbit the d shell and have degeneracy 5, such as, dz_2, d_{x2-y2}, d_{xy}, d_{yz}, d_{xz}, as shown in **Fig. 10**.

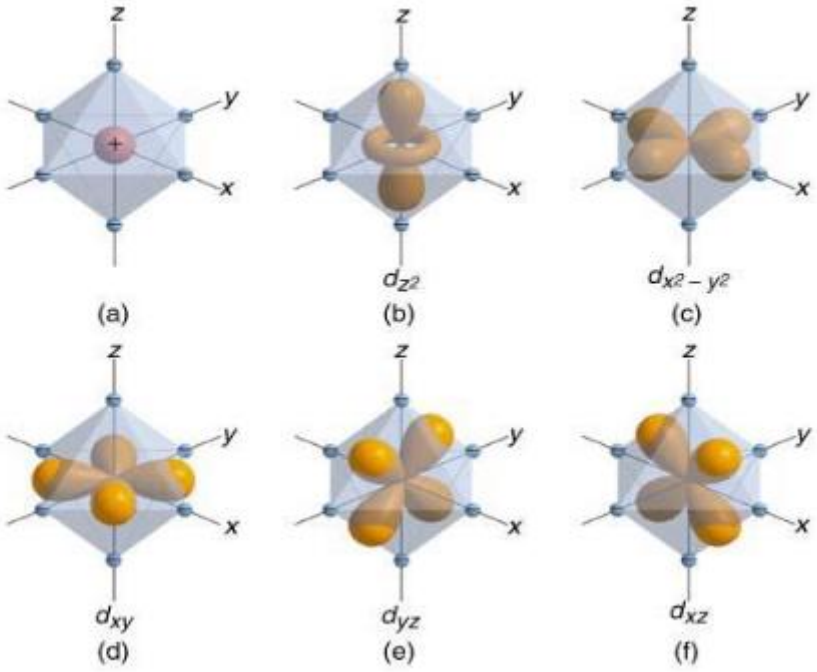

Figure 10: Octahedral matrix of negative charges approaching a metal ion. (b – f) Angular distribution of "d" orbitals

The crystalline field causes the d electron energies of the metal ion to increase, but the d orbitals do not all behave the same under the influence of crystal field, due to the shape of the orbitals and how their lobes are oriented in relation to the binder. Due to the orientation of the d_{z2} and d_{x2-y2} orbitals they will experience stronger repulsions than of the d_{xy}, d_{xz}, and d_{yz} orbitals as they approach the ligands. In this way, the crystalline field can act in different ways depending on the type of symmetry in which Mn will be incorporated .

- Weak Crystalline Field Interaction is observed in series 4f (rare earths). In that In this case, the crystalline field is generated by point charges that are found around of rare earths. The effect of the crystalline field on rare earths or systems with rare earths is weak, as the 4f layer of rare earths is sufficiently shielded by the ion's outermost layers [21].

The understanding of magnetic behaviors and possible mechanisms for allow the magnetic interactions to occur, which have been described in this chapter, will assist in the investigation of the mechanism of magnetic interaction that can occur with the compounds $RMn_2Si(Ge)_2$ intermetallic. This is the main motivation for carrying out the measurements. of hyperfine interactions, being of fundamental importance the understanding of each one of these exchange mechanisms, as well as the effects of the crystalline field and the behavior of the Brillouin function to help define the T_C and T_N.

2- Study of the intermetallic Mn_3Z compound:

Heusler materials Mn_3Z type (Z=Ga, Sn, and Ge), this material can exist in different structural phases, where each phase has its own magnetic properties. The hexagonal structure is well known for decades. The Mn elements in the hexagonal structure form a kagome array in a plane with the Z atom in the hex center. However, the Mn elements exhibit an AFM coupling with a low magnetic moment [22-28]. The cubic structure is the standard full Heusler structure. This phase is characterized by the presence of Mn atoms in two unique sites of the lattice, these different positions have magnetic moments of opposite directions, which leads to the FiM order [29-30]. Also, it has a high density of states at the Fermi energy, and thus a Peierls transition could occur [31]. The tetragonal phase can be considered a cubic phase with a distortion in the z-direction, This distortion causes the magnetic moments to favor the c-

axis, meaning that the system exhibits perpendicular MAE [32], thus offering a significant opportunity for future high-density spin transfer torque (STT) applications [33]. In several experiments, the Mn_3Z hexagonal phase (Z = Ga, Sn, and Ge) has been synthesized by high temperature annealing of the samples [31-33], whereas the Mn_3Ga and Mn_3Ge tetragonal phase has been obtained by low temperature annealing. The cubic phase was not observed until now, because it can be unstable as mentioned above. Also, the tetragonal phase of Mn_3Sn has not been reported in the literature yet, although it would be anticipated that it behaves similarly as the other two compounds. The probable transition between the phases hexagonal, cubic, and tetragonal has drawn considerable attention of researchers, but a comprehensive study remains to be undertaken.

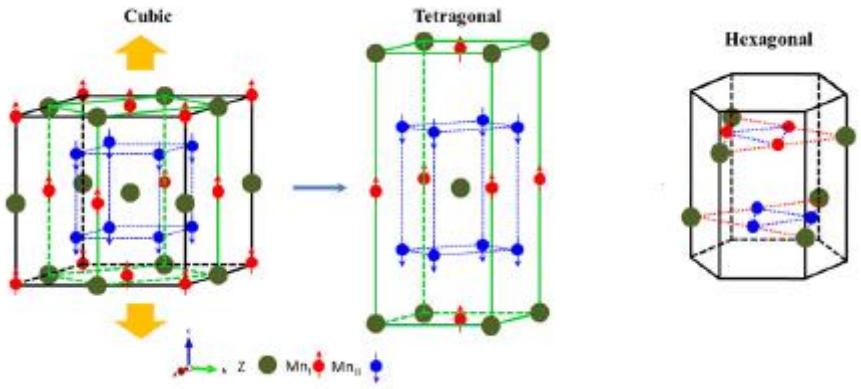

Figure 11: The crystal structure of the Mn3Z material.

3- Application of the intermetallic compound:

Intermetallic applications can be divided into two categories:

Category 1: application that use magnetocaloric effect. Some of these applications follow:

- Magnetic refrigeration
- In medicine in treatment of malign tumors by means of the hyperthermia treatment. The hyperthermia is a famous treatment process which is based on a different reaction

of the atypical (malignant) and the healthy cells to an elevated temperature; the former die under temperatures around 43°C, the latter can resist such conditions.

- Delivery and release of drugs. The delivery of drugs to the target organs of a human organism is one of the fundamental problems in treatment of various diseases, including the oncology, and in diagnosis. It is also often necessary to perform controlled release of one or more drugs into an organism.

Category 2: application of spintronic devices that use the AHE. Some of these applications follow:

- spin-transfer torque random access memory (STTMRAM)
- spin valves
- magnetic tunnel junction
- spin gapless semiconductor
- magnetic shape memory effect

Conclusion

To summarize, Intermetallic compound have taken an important part in our daily life. They are found in everywhere in modern technologies. In this chapter, we presented the basic concepts needed to understand the characteristics of an Intermetallic compound, some of their current applications and well commercialized families of Intermetallic materials.

CHAPTER 2: Computational methods

Part A:

The DFT theory

A.1- Introduction to Density Functional Theory:

DFT is a quantum computational method for studying electronic structure, in principle in an exact manner. The principle of DFT consists of a reformulation of the many-body quantum problem into a one-body problem (or, strictly speaking, two-body if we consider spin problems) with the parameter of the electron density. The central idea of DFT is that the sole electron density of the ground state of the system fully determines the average values of observables, such as energy [34]. The study of matter is carried out from quantum mechanics which consists in describing real systems by solving the Schrödinger equation [35]:

$$\mathbf{H\Psi = E\Psi} \qquad \text{(A. 2.1)}$$

Where H is the Hamiltonian of the system, $\boldsymbol{\Psi}$ is the wave function of the system and **E** is the eigenvalue of the Hamiltonian which corresponds to this system Since the total Hamiltonian $\hat{H}_{\boldsymbol{T}}$ associated with a system with several interacting particles (N Nuclei + M electrons) is the sum of the total kinetic energy operator $\widehat{\mathbf{T}}_{\mathbf{T}}$ and the operator describing the set of Coulomb interactions $\widehat{\boldsymbol{V}}_{\boldsymbol{T}}$ (potential energy):

$$\hat{H}_{\mathbf{T}} = \widehat{\mathbf{T}}_{\mathbf{N}} + \widehat{\mathbf{T}}_{\mathbf{e}} + \widehat{\mathbf{V}}_{\mathbf{N-e}} + \widehat{\mathbf{V}}_{\mathbf{N-N}} + \widehat{\mathbf{V}}_{\mathbf{e-e}} \qquad \text{(A.2.2)}$$

Where :

$\widehat{\mathbf{T}}_{\mathbf{N}} = -\frac{\hbar^2}{2}\sum_{\mathbf{i}}\frac{\nabla^2_{\mathbf{Ri}}}{\mathbf{M_N}}$: Kinetic energy of the N nuclei of mass $\boldsymbol{M_N}$

$\widehat{\mathbf{T}}_{\mathbf{e}} = -\frac{\hbar^2}{2}\sum_{\mathbf{i}}\frac{\nabla^2_{\mathbf{ri}}}{\mathbf{m_e}}$: Kinetic energy of the M electrons of mass $\boldsymbol{m_e}$

$\widehat{\mathbf{V}}_{\mathbf{N-e}} = -\frac{\mathbf{1}}{\mathbf{4\pi\varepsilon_0}}\sum_{\mathbf{i,j}}\frac{\mathbf{e^2 Z_i}}{|\mathbf{R_i - r_j}|}$: Attractive nucleus-electron Coulomb interaction

$\widehat{\mathbf{V}}_{\mathbf{e-e}} = \frac{\mathbf{1}}{\mathbf{8\pi\varepsilon_0}}\sum_{\mathbf{i\neq j}}\frac{\mathbf{e^2}}{|\mathbf{r_i - r_j}|}$: Repulsive electron-electron Coulomb interaction

$\widehat{\mathbf{V}}_{\mathbf{N-N}} = \frac{\mathbf{1}}{\mathbf{8\pi\varepsilon_0}}\sum_{\mathbf{i\neq j}}\frac{\mathbf{e^2 Z_i Z_j}}{|\mathbf{R_i - Rj}|}$: Coulomb repulsive nucleus-nucleus interaction

$$\hat{H}_T = -\frac{\hbar^2}{2}\sum_i \frac{\nabla_{Ri}^2}{M_N} - \frac{\hbar^2}{2}\sum_i \frac{\nabla_{ri}^2}{m_e} - \frac{1}{4\pi\varepsilon_0}\sum_{i,j}\frac{e^2 Z_i}{|R_i - r_j|} + \frac{1}{8\pi\varepsilon_0}\sum_{i\neq j}\frac{e^2 Z_i Z_j}{|R_i - R|} + \frac{1}{8\pi\varepsilon_0}\sum_{i\neq j}\frac{e^2}{|r_i - r_j|} \quad (A.2.3)$$

*** Problem :**

For a system with N nuclei and M electrons, the problem to be treated is a problem with (N+M) particles in electromagnetic interaction. Solving this equation in analytical form is impossible, so to solve this problem we apply a series of simplifications and successive approximation techniques.

A.1.1- Born-Oppenheimer approximation:

It consists in separating the movements of the electrons from those of the nuclei; this is justified because the speed of nuclei is very low compared to the speed of electrons. The above equation becomes [36]:

$$\hat{H}_T = \hat{T}_e + \hat{V}_{e-e} + \hat{V}_{N-e} \quad (A.2.4)$$

Where: $\hat{V}_{N-e} = \hat{V}_{ext}$:

$$\hat{H}_T = -\frac{\hbar^2}{2}\sum_i \frac{\nabla_{ri}^2}{m_e} + \frac{1}{8\pi\varepsilon_0}\sum_{i\neq j}\frac{e^2}{|r_i - r_j|} - \frac{1}{4\pi\varepsilon_0}\sum_{i,j}\frac{e^2 Z_i}{|R_i - r_j|} \quad (A.2.5)$$

The application of (ABO), brought us back to a problem of N interacting electrons subjected to an external field created by the nuclei (assumed to be fixed). Problem which remains too difficult to solve due to the electron-electron interaction so therefore other approaches have been proposed such as the Hartree, Hartree-Fock and DFT approximations.

A.1.2- Hartree approximation :

It is based on the independence between electrons (one electron is independent of the other). The total wave function Ψ is the product of the mono-electron wave functions ψ_i [37]:

$$\Psi(\mathbf{r_1}, \mathbf{r_2} \ldots\ldots\ldots \mathbf{r_n}) = \psi_1(\mathbf{r_1})\psi_2(\mathbf{r_2}) \ldots\ldots\ldots \psi_N(\mathbf{r_N}) \quad \text{(A.2.6)}$$

Each wave function ψ_i then corresponds to a Schrödinger equation:

$$-\frac{\hbar^2}{2m}\Delta\psi_i(\vec{r}) + V_{eff}\psi_i(\vec{r}) = \varepsilon_i\psi_i(\vec{r}) \quad \text{(A.2.7)}$$

These are the Hartree equations, of which $\boldsymbol{\varepsilon_i}$ represents the electronic level corresponding to $\boldsymbol{\psi_i}(\vec{\mathbf{r}})$:

$-\frac{\hbar^2}{2m}\boldsymbol{\Delta}$: Kinetic energy of the electron

V_{eff} : EP undergone by the electron under the influence of the nucleus as well as that of the other electrons. The latter takes into account the electron-nucleus interaction described by:

$$\mathbf{V_N}(\vec{\mathbf{r}}) = -\mathbf{Ze^2}\sum\frac{1}{|\vec{\mathbf{r}}-\vec{\mathbf{R}}|} \quad \text{(A.2.8)}$$

For the electron-electron interaction, we consider that the electron moves in a potential $V_H(\vec{r})$ such as:

$$\mathbf{V_H}(\vec{\mathbf{r}}) = -\mathbf{e}\int\frac{\mathbf{d^3}\vec{\mathbf{r'}}}{|\vec{\mathbf{r}}-\vec{\mathbf{r'}}|}\boldsymbol{\rho}(\vec{\mathbf{r}}') \quad \text{(A.2.9)}$$

This potential describes the interaction of an electron subjected to the other electrons represented by a density $\rho(\vec{r})$.

Thus the electron is subject to these two potentials:

$$\mathbf{V_{eff}}(\vec{\mathbf{r}})=\mathbf{V_H}(\vec{\mathbf{r}}) + \mathbf{V_N}(\vec{\mathbf{r}}) \quad \text{(A.2.10)}$$

The Eigen functions of the solution make it possible to calculate the new electron density:

$$\rho(\vec{r}) = \sum_i^{occu}\psi_i^*(\vec{r})\psi_i(\vec{r}) \quad \text{(A.2.11)}$$

Introducing the Poisson equation which makes it possible to make the link between the Hartree potential and the electron density:

$$\mathbf{V_H}(\vec{\mathbf{r}})= \mathbf{-4\pi\rho}(\vec{\mathbf{r}}) \quad \text{(A.2.12)}$$

It is a self-consistent process since the wave function, electron density and potential are interdependent. This process is also used in the other approaches.

A.1.3- Hartree-Fock approximation :

It is based on an important element: the Pauli principle of exclusion. The latter leads us to consider the antisymmetry of the wave function of a quantum electronic system such as [37]:

$$\psi_1(\vec{r}_1,.....\vec{r}_a,.....,\vec{r}_b.....\vec{r}_N) = -\psi_1(\vec{r}_1,.....\vec{r}_b,.....,\vec{r}_a.....\vec{r}_N) \qquad \text{(A.2.13)}$$

Introduction of this antisymmetric contribution in the Schrödinger equations.
The new wave function that we use makes use of Slater's determiner, so we obtain the following Schrödinger equation for an electron:

$$-\frac{\hbar^2}{2m}\Delta\psi_i(\vec{r}) + V_{eff}\psi_i(\vec{r}) - \sum_j\{\int\frac{d^3\vec{r}'}{\left|\vec{r}-\vec{r}'\right|}\psi^*_j(\vec{r}')\psi_i(\vec{r}')\}\psi_j(\vec{r}) = \varepsilon_i\psi_i(\vec{r}) \qquad \text{(A.2.14)}$$

The difference between the Hartree and Hartree-Fock equations is due to the presence of the third term which expresses the exchange potential and takes into account the antisymmetry of the wave function. This is a correction that makes the Hartree-Fock equations much harder to solve.

A.2- Principle of Density Functional Theory:

A.2.1- Hohenberg and Kohn theorem (H.K):

Hohenberg and Kohn's approach proved that for such a system the ground state wave function is a unique function of the electron density, $E = E[\rho(\vec{r})]$ so any observable $\hat{O}$ depends on the density functional [38]. The total energy of the system is written in the following form:

$$\mathbf{E(\rho) = F_{HK}(\rho) + V_{ext}(\rho)} \qquad \text{(A. 2.15)}$$

Where : $\mathbf{F_{HK}(\rho) = T(\rho) + V_{ee}(\rho)}$ and $\mathbf{V_{ext} = \int \hat{V}_{ext}(r)\rho(r)dr}$ $F_{HK}(\rho)$: H.K Universal Function.

$V_{ext}(\rho)$: extern potential

The term E (ρ) is minimal when the density ρ(r) corresponds to the electron density of the ground state.

The two theorems of Hohenberg and Kohn:

Theorem 1.

The ground state density uniquely determines an external potential.

Theorem 2.

The total energy functional of any multiparticle system has a minimum that corresponds to the ground state and the ground state particle density. Knowing the functional $F_{HK}[\rho(\vec{r})]$ in an exact way allows to determine the total energy of the system and the properties of the ground state. However, this function is difficult to determine exactly, we use the Kohn and Sham approximation.

A.2.2- Kohn-Sham theorem:

It was based on the use of a fictitious system of non-interacting electrons, replacing the repulsion by an EP and also based on the wave function to determine the density and one can rewrite equation (A.2.15) as the following form [39]:

$$\boldsymbol{E(\rho) = T_s(\rho) + V_{ext}(\rho) + V_c(\rho) + E_{XC}(\rho)} \qquad \text{(A.2.16)}$$

Where:

$\boldsymbol{T_s(\rho)}$: Kinetic energy of non-interacting electrons.

$\boldsymbol{V_c(\rho)}$: Coulomb electron-electron interaction energy.

$\boldsymbol{E_{XC}(\rho)}$: Correlation exchange energy.

By definition $\boldsymbol{T_S(\rho)}$is written in the following form:

$\boldsymbol{T_s(\rho)} = \sum_{i=1}^{N} \left\langle \boldsymbol{\Psi_i} \middle| -\frac{\nabla^2}{2} \middle| \boldsymbol{\Psi_i} \right\rangle$; We use Hartree atomic units ($m_e = \hbar = e = 1$)

$$\text{With} \quad \boldsymbol{\rho(r)} = \sum_{i=1}^{N} |\boldsymbol{\Psi_i(r)}|^2 \tag{A.2.17}$$

By minimizing $E(\rho)$ with respect to Ψ_i taking into account theorem 2 of H.K and by introducing the parameters of Lagrange $\in_i$ it comes:

$$\frac{\partial}{\partial \boldsymbol{\Psi_i^*(r)}} [\boldsymbol{E} - \in_i \int \boldsymbol{\Psi_i^*(r)\Psi_i(r)dr}] \tag{A.2.18}$$

After calculation:

$$\left[-\frac{\nabla^2}{2} + \boldsymbol{V_{eff}(r)}\right] \boldsymbol{\Psi_i(r)} = \in_i \boldsymbol{\Psi_i(r)} \tag{A.2.19}$$

Where :

$$\boldsymbol{V_{eff}(r)} = \boldsymbol{V_{ext}(r)} + \boldsymbol{V_H(r)} + \boldsymbol{V_{XC}(r)} \tag{A.2.20}$$

$\boldsymbol{V_H(r)} = \int \frac{\rho(r')}{|r-r'|} \boldsymbol{dr}$: Hartree potential.

$\boldsymbol{V_{XC}(r)} = \frac{\partial E_{XC}}{\partial \rho(r)}$: EC potential.

The elaboration of the KSE made it possible to highlight the fact that the only density functional remaining unknown within this formalism corresponds to the exchange functional – correlation $E_{XC}[\rho(\vec{r})]$, therefore recourse to LDA and GGA corrections…

These two types of major approximations have been developed:

In the 1980s: **Local Density Approximation (LDA)**

In the 1990s: **Generalized Gradient Approximation (GGA)**

A.2.3- Local Density Approximation (LDA):

It treats electron density locally as a uniform electron gas.

Hypotheses [40]:

-The EC effects are dominated by the localized density at $\vec{r}$,

- The density $\rho(\vec{r})$varies slowly with the position $\vec{r}$,

- The contribution of $E_{XC}[(\rho(\vec{r})]$ to the total energy of the system can be added cumulatively from each portion of the non-uniform gas as if it is locally uniform. Indeed, the EC part has for expression:

$$\boldsymbol{E_{XC}^{LDA}[\rho(\vec{r})] \approx \int \epsilon_{XC}^{LDA}[\rho(\vec{r})]\, \rho(\vec{r}) d\vec{r}} \quad \text{(A.2.21)}$$

Where: $\boldsymbol{\epsilon_{XC}^{LDA}[\rho(\vec{r})]}$ **:** EC energy

Hence an EC potential $V_{XC}^{LDA}(\overrightarrow{r})$ can be expressed by the following equation:

$$\boldsymbol{V_{XC}^{LDA}(\overrightarrow{r}) = \frac{\partial(\rho(\overrightarrow{r})\epsilon_{XC}^{LDA}[\rho(\vec{r})])}{\partial\rho(\vec{r})}} \quad \text{(A.2.22)}$$

For magnetic materials, taking into account the electronic spin which adds an additional degree of freedom to the LDA which extends to the approximation of the local spin density (LSDA: Local Spin Density Approximation) Hence the equations:

$$\boldsymbol{E_x^{LSDA}[\rho(\vec{r})] = -2^{1/3} C_x \int [\rho_{\downarrow}^{\frac{4}{3}}(\vec{r}) + \rho_{\uparrow}^{\frac{4}{3}}(\vec{r})]\ d\vec{r}} \quad \text{(A.2.23)}$$

$$\boldsymbol{\epsilon_x^{LSDA}[\rho(\vec{r})] = -2^{1/3} C_x [\rho_{\downarrow}^{\frac{1}{3}}(\vec{r}) + \rho_{\uparrow}^{\frac{1}{3}}(\vec{r})]} \quad \text{(A.2.24)}$$

Where $\boldsymbol{C_x = 3/4(3/\pi)^{\frac{1}{3}}}$

The LSDA formalism is identical to the LDA formalism when we have a system with closed layers. It turned out that this functional cannot study all systems whose electron density is highly variable with respect to $\vec{r}$.

A.2.4- Generalized Gradient Approximation (GGA):

The formalism of the GGA joins the formalism of the LDA, the contribution $E_{XC}[(\rho(\vec{r})]$to the total energy of the system seen in the LDA [41]. The GGA brings an improvement to the EC energy which consists in making the functional $E_{XC}[(\rho(\vec{r})]$dependent on the electron density and also on the gradient of this electron density $[\nabla\rho(\vec{r})]$.

This modification of the function $E_{XC}[(\rho(\vec{r})]$ accounts for the non-uniform character of electron gases. In other words, GGA functional cannot be considered as nonlocal methods since they only depend on the density at a given point $(\vec{r})$ and not on a volume of space. The expression of the functional GGA is written as:

$$\boldsymbol{E_{XC}^{GGA}[\rho(\vec{r})] \approx \int \epsilon_{XC}^{GGA}[\rho(\vec{r}), |\nabla\rho(\vec{r})|]\, \rho(\vec{r}) d\vec{r}} \qquad \text{(A.2.25)}$$

Where:

$\boldsymbol{\epsilon_{XC}^{GGA}[\rho(\vec{r}), |\nabla\rho(\vec{r})|}$: EC energy by an electron in a system of mutually interacting electrons of non-uniform density.

The massive use of the DFT is due to the functional of the GGA type. Indeed, the GGA could not correctly handle systems characterized by Van Der Waals interactions related to long-range correlations.

A.3- Solving the Kohn-Sham equations:

The methods based on the DFT are classified according to the representations which are used for the density, the potential and particularly the orbitals of Kohn and Sham. The choice of the representation is made to minimize the computational cost by maintaining a sufficient precision. Various methods can be used to solve the KSE. These methods are differentiated according to:

• The electron-nucleus interaction potential (V_{ext}).

• The potential for EC.

• The wave base on which the wave functions are developed. Considering the equation

$$\left\{ \underbrace{-\frac{\hbar^2}{2m}\nabla^2}_{a} + \underset{b}{V_{Ne}(\vec{r})} + V_{Hartree}(\vec{r}) + \underset{c}{V_{xc}(\vec{r})} \right\} \varphi i(\vec{r}) = \underset{d}{\varepsilon_i \varphi i(\vec{r})} \qquad \text{(A.2.26)}$$

(a) Kinetic energy determined by a relativistic calculation or not.

(b) electron-nucleus interaction potential V_{Ne} .

There are two major classes of potentials:

• Pseudo-potentials •

All-electron potentials: Muffin-tin type or Full Potential

(c) Potential for EC:

• LDA

• GGA

(d) Basis on which the wave function is developed:

• Plane wave type digital base.

• Optimized base: Linearized Muffin Tin Orbitals (LMTO),

• Augmented plane waves (LAPW).

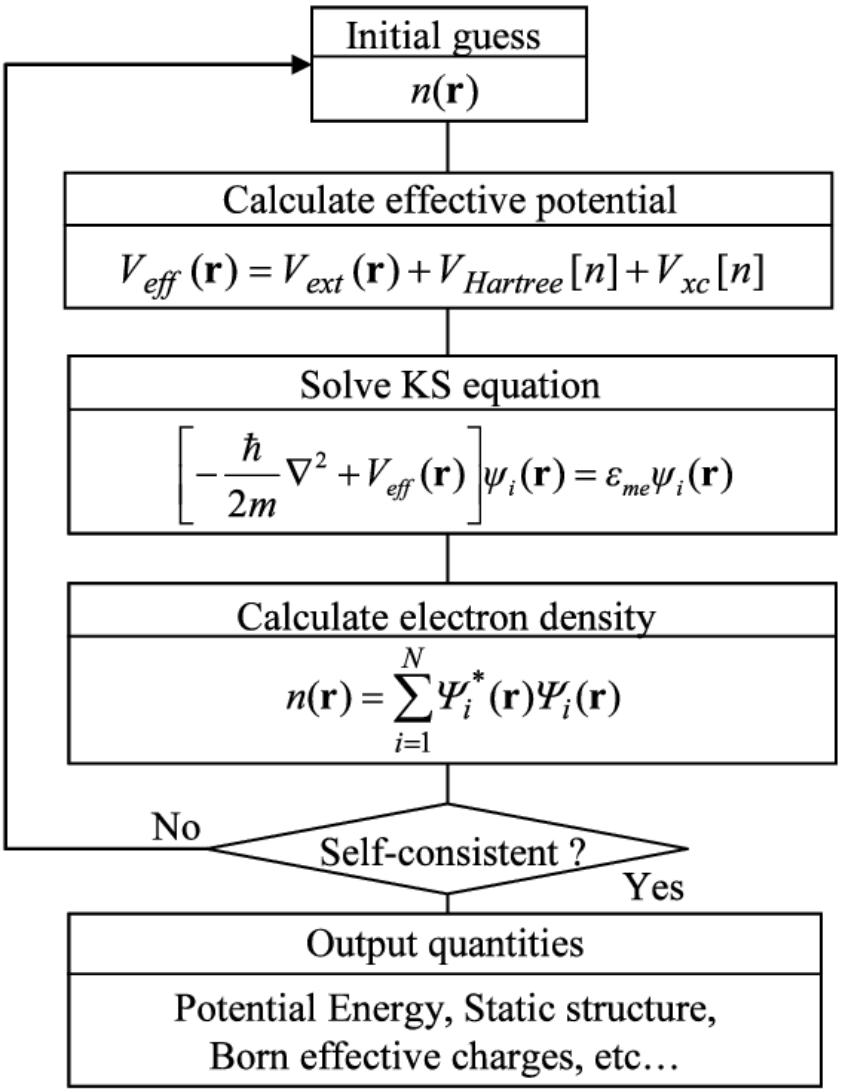

Figure 12: schematic representation of the resolution of KS equation

A.3.1- The pseudo potential method:

This method is based on the assumption that the physical and chemical properties of a system are essentially governed by the valence electrons (i.e. the outermost electrons) while the ionic cores can be considered to be frozen in their atomic configuration. The method of pseudopotentials thus consists in treating explicitly only the valence electrons, which then move in an effective external potential produced by these inert ionic cores called pseudopotentials.

A.3.2- The LCAO method:

Orbitals are used to find a better density (ρ) through the cycle self-consistent. A set of plane waves has the advantage that allows the rapid passage of Fourier "transforms" between direct and reciprocal spaces. A more efficient basis would of course be the KS orbitals. Unfortunately, these have the great disadvantage of being unknown at the start of the calculation. An alternative would be the use of a linear combination of atomic orbitals (LCAO).

A.3.3- The KKR-CPA method:

The Kohn-Korringa-Rostoker (KKR) method in 1954 for the calculation of the electronic band structure is a method using multiple scattering theory reformulated by the technique of Green's functions to solve the Schrödinger equation without resorting to the wave functions nor to the eigenvalues of the Hamiltonian of the system. In this approach, the properties of scattering by each scattering center (atom) are described by a scattering matrix, while multiple scattering by all atoms in the lattice is determined by the fact that the incident wave at each center is the sum of the outgoing waves from the other scattering centers.

A.3.4- The APW method:

The development of the APW method is based on Slater's observation which states that: Near the nuclei, the potential and the wave functions are similar to those of an atom. They vary strongly according to a spherical symmetry between the atoms. Both potential and wave functions are smoother, therefore space can be divided into two regions:

(i) spheres called "Muffin-Tin" encompassing the atoms and (ii) an interstitial region delimiting the residual space not occupied by the spheres.

A.3.5- The FP-LAPW method:

The “Full Potential Linearized Augmented Plane Wave (FP-LAPW)” method developed by the Schwarz team, [42-43] is based on the self-consistent resolution of the KSE in two arbitrarily defined regions of the lattice elementary. [39]

Region I corresponds to non-overlapping atomic spheres of radius Rmt (mt = muffin tin), where a series of linear combinations of radial and angular functions is used.

Region II is the interstitial region between the spheres. It is described by an expansion of plane waves. The two types of region, represented schematically in Figure (I-1).

The convergence of this base is controlled by a cut-off parameter Rmt*Kmax which is the product of the radius of the smallest muffin-tin sphere (Rmt) times the cut-off energy of the plane wave base . This method allows the consideration of a realistic potential (FP = Full Potential) which is not restricted to the spherical component. Unlike methods using pseudo-potentials, the core electrons are integrated into the calculation. This gives a correct description of the wave functions near the nucleus. This is the most accurate method, but it is computationally heavy.

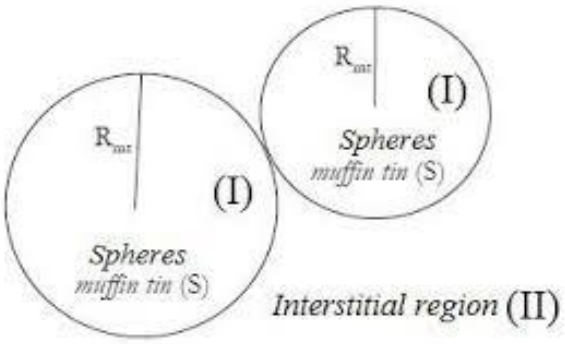

Figure 13: Schematic illustration of two atomic spheres A and B with radius RMT (region I) and the interstitial region between the spheres (region II).

Part B:

Noncollinear magnetism in itinerant-electron systems: theory and applications

B.1- Introduction to the Density functional theory of a noncollinear magnet:

More than 40 years ago, the first NC magnetic structures were experimentally uncovered [44-45]. However, the physical mechanism was studied almost totally within model Hamiltonians that assumed localized atomic moments [45], in opposition to collinear magnets that have been extensively explored with first principles computing frameworks from DFT [46-48]. This may be because NC magnetic order appeared to be rather rare and more exotic, but received a boost of interest during the late 1970s and the beginning of 1980s, as it became apparent that the theory of Stoner, which provides a reasonably good description of the ground state properties, was unable to explain the temperature behaviour of itinerant magnets. The rationale for this failure was identified as being the disregard of fluctuations in the magnetization density, which is considered as arising from the well-defined atomic moments, and is equivalent to disregarding fluctuations in the orientations of these atomic moments (for example [49]). Detailed examinations of notable NC magnetic arrangements were initiated by Heine and al [50], with the cluster recursion method applied to a simplified tight-binding Hamiltonian. Furthermore, the continuation of this study was done through the use of the KKR approach for a periodic solid (for example [51]). A detailed discussion about the DFT for a NC magnet was then presented in [52] and implemented to study the ground state and electronic and magnetic arrangement of Mn_3Sn. The discovery of a spiral magnetic structure in Fe fcc [53] has made it an attractive object for theoretical research [54, 55]. During the last several years, research on NC magnetism has grown. As a result, some successful investigations about amorphous systems [56-58] and also about multilayers [59, 60] were published and a notable and exciting progress has been achieved in defining the spin

dynamics in itinerant electron systems [61]. Despite its relatively brief history of NC magnetism theory employs a variety of approaches and applies to several physical problems.

B.2- Basic theorems and Kohn-Sham equation:

A key difference between NC and collinear magnets is that in the NC case the natural axis for quantization of the common spin across the crystal is absent. As a consequence, each one-electron state in a noncollinear magnet should be considered as a two-component spin function. $\begin{pmatrix} \psi_1(r) \\ \psi_2(r) \end{pmatrix}$. With the help of the standard spin $-\frac{1}{2}$ rotation matrix

$$\boldsymbol{U}(\theta,\phi)=\begin{bmatrix} \cos(\theta/2)e^{i\phi/2} & \sin(\theta/2)\,e^{-i\phi/2} \\ -\sin(\theta/2)\,e^{i\phi/2} & \cos(\theta/2)e^{-i\phi/2} \end{bmatrix} \tag{B.1}$$

the spinor wavefunction can be represented as:

$$\begin{bmatrix} \psi_1(r) \\ \psi_2(r) \end{bmatrix}=U(\theta(\mathrm{r}),\,\phi(\mathrm{r}))\begin{bmatrix} 1 \\ 0 \end{bmatrix}, \tag{B.2}$$

The polar angles θ(r) and ϕ (r) identify the spin moment orientation for the given state at the r point. As a result, the density matrix for the crystal is not diagonal in the NC case:

$$\rho(\mathrm{r})=\begin{bmatrix} \rho_{11}(r) & \rho_{12}(r) \\ \rho_{21}(r) & \rho_{22}(r) \end{bmatrix}, \tag{B.3}$$

The summation of the diagonal components of ρ(r) produces the charge density and the difference between the diagonal components in the projection of the magnetization density onto the overall quantization axis. The non-diagonal components on the matrix define the element of the magnetization density that lies on the quantization axis and lead to the noncollinearity character of the magnetic structure. It was demonstrated in an earlier paper that the density matrix is an essential physical property which determines in a singular way all the ground state characteristics of a magnetic electron system [62] Specifically, the total energy becomes a feature from the density matrix and it takes the lowest for the ground state value of the density matrix. Firstly, we determine the total energy as a function of the density

matrix and then use the variation procedure to determine the smallest value of this functional. Usually, the shape of the functional is only found in specified approximations. A standard expression of the energy functional is the following:

$$E[\rho] = T[\rho] + \iint \frac{n(r)n(\acute{r})}{|r-\acute{r}|} dr\, d\acute{r} + \sum_{\alpha\beta} \int \mathrm{w}_{\alpha\beta}(r)\rho_{\alpha\beta}(r)\, dr \; + E_{xc}\,[\rho] \qquad \text{(B.4)}$$

Or T denotes the kinetic energy of the non-interacting electrons, The second term corresponds to the classical Coulomb energy of the charge distribution n = Tr , and the 3rd term represents the energy of the interaction of the electronic system for the external field, $\mathrm{w}_{\alpha\beta}$. Finally, the E_{xc} include the remaining energy. According to Kohn and Sham's concept, this density matrix may be expressed as effective one-electron states:

$$\rho(r) = \sum \begin{bmatrix} \psi_1(r) \\ \psi_2(r) \end{bmatrix}_i [\psi_1(r)\, \psi_2(r)]^* = \sum \begin{bmatrix} \psi_1(r)\,\psi_1(r)^* & \psi_1(r)\,\psi_2(r)^* \\ \psi_2(r)\,\psi_1(r)^* & \psi_2(r)\,\psi_2(r)^* \end{bmatrix}_i \qquad \text{(B.5)}$$

The change relative to the elements of the density matrix can be replaced by the variation in terms of wave functions for the one-electron spinor. The modification leads to the one-electron Schrodinger equation:

$$\left(-\nabla^2 I + \begin{bmatrix} \mathrm{v}_{11}^{eff}(r) & \mathrm{v}_{12}^{eff}(r) \\ \mathrm{v}_{21}^{eff}(r) & \mathrm{v}_{22}^{eff}(r) \end{bmatrix}\right) \begin{bmatrix} \psi_1(r) \\ \psi_2(r) \end{bmatrix}_i = \varepsilon_i \begin{bmatrix} \psi_1(r) \\ \psi_2(r) \end{bmatrix}_i \qquad \text{(B.6)}$$

Where **I** is the second order unit matrix; the elements of the EPare defined as follows:

$$\mathrm{v}_{\alpha\beta}^{eff}(r) = \mathrm{w}_{\alpha\beta}(r) + 2\delta_{\alpha\beta} \int \frac{n[\acute{r}]}{|r-\acute{r}|} d\acute{r} + \mathrm{v}_{\alpha\beta}^{ex}(r) \qquad \text{(B.7)}$$

The potential for EC is as follows:

$$\mathrm{v}_{\alpha\beta}^{ex}(r) = \frac{\delta E_{xc}\{\rho_{\alpha\beta}\}}{\delta \rho_{\alpha\beta}} \qquad \text{(B.8)}$$

Under the local approximation, the spatial variation of the magnetization direction has no effect over the exchange correlation potential at a specific point. Consequently, for any point we may identify the potential shape in a local system. In this case, it is useful to consider such system along the *z* axis lying to the magnetization direction around this point. Author take the non-diagonal elements of the density matrix null than we may use this finding [62] to define

the shape of the EC potential. Transformation of the density matrix from the global coordinates system to the local system may be performed using the function spin $-\frac{1}{2}$ rotation matrices (B.1):

$$\begin{bmatrix} \rho_{11}(r) & \rho_{12}(r) \\ \rho_{21}(r) & \rho_{22}(r) \end{bmatrix} = U(\theta(\mathrm{r}), \phi(\mathrm{r})^{+} \begin{bmatrix} \rho_{+}(r) & 0 \\ 0 & \rho_{-}(r) \end{bmatrix} U(\theta(\mathrm{r}), \phi(\mathrm{r})), \qquad \text{(B.9)}$$

Where the polar angles θ(r) and ϕ (r) identifying the direction of the local magnetization around r point are described by the elements from the density matrix of the global system:

$$\tan[\phi(r)] = -\frac{Im[\rho_{12}(r)]}{Re[\rho_{12}(r)]}, \qquad \text{(B.10)}$$

$$\tan[\theta(r)] = \frac{2(\{Re[\rho_{12}(r)]\}^2 + \{Im[\rho_{12}(r)]\}^2)^{\frac{1}{2}}}{\rho_{11}(r) - \rho_{22}(r)} \qquad \text{(B.11)}$$

Lastly, the EP (B.7) may be expressed as:

$$V^{eff}(r) = \left(\sum_{nv} \frac{2Z_{\mathrm{v}}}{|r_{nv}|} + \int 2\frac{n(\acute{r})}{|r-\acute{r}|}\right)\mathbb{I}$$

$$+U(\theta(\mathrm{r}), \phi(\mathrm{r})^{+} \begin{bmatrix} \mathrm{v}^{eff}(\rho_{+}(r), \rho_{-}(r)) & 0 \\ 0 & \mathrm{v}^{eff}(\rho_{+}(r), \rho_{-}(r)) \end{bmatrix} U(\theta(\mathrm{r}), \phi(\mathrm{r}))$$

$$= U(\theta(\mathrm{r}), \phi(\mathrm{r}))^{+} \begin{bmatrix} \mathrm{v}_{+}^{eff}(r) & 0 \\ 0 & \mathrm{v}_{-}^{eff}(r) \end{bmatrix} U(\theta(\mathrm{r}), \phi(\mathrm{r})) \qquad \text{(B.12)}$$

Where

$$\mathrm{v}_{\sigma}^{eff}(r) = \sum_{nv} \frac{2Z_{\mathrm{v}}}{|r_{nv}|} + \int 2\frac{n(\acute{r})}{|r-\acute{r}|} dr + \mathrm{v}_{\sigma}^{ex}(\rho_{+}\acute{}(r), \rho_{-}(r)), \qquad \sigma=\pm 1 \qquad \text{(B.13)}$$

Without any external applied field into the crystal, the field **w** from equation (B.7) is deceased to the Coulomb field of the nuclei, Z_{v} is the atomic number of the atom which is located at the center of

$$R_{nv} = R_n + a_{\mathrm{v}}; \qquad \text{(B.14)}$$

Here R_n are the lattice vectors, a *t* the atomic positions within a unit cell;

$$r_{nv} = r - R_{nv} \qquad \text{(B.15)}$$

The EP obtained from equation (B.12) is mainly related to the density matrix. Concurrently, a new form of the density matrix (B.5) is given through the solutions of equation (B.6) using the potential (B.12). As a result, we are confronted with a self-consistent density matrix computational problem. In comparison with the case of the collinear magnet, the current problem is considerably more complicated owing to the added degree of freedom related to the spatial variation of the magnetization direction. For simplification purpose, the approximation of the atomic sphere for the direction of magnetization is generally adopted; it is supposed that inside the atomic sphere of a particular atom, the direction of magnetization is fixed and the non-collinearity of its magnetic structure is minimized at the various magnetic moment orientations of the atoms. At this point, these angles θ and ϕ are determined by formulas similar to equations (B.10) and (B.11), except for the use of integrated density matrices:

$$\rho_{nv} = \int_{\Omega\, nv} \rho(r) dr, \tag{B.16}$$

Once the integration is done on the (nv) th atomic sphere with a diameter of S_v . (Consider that, in an early manuscript, Nordstrom and Singh [63] have succinctly described the earliest investigation of the non-collinearity nature of the magnetization density in atomic spheres.) Under the assumption of spherical symmetry of the potential in the inside of the atomic spheres, we might describe the potential (B.12) in the following final form.

$$v^{eff}(r) = \sum_{nv} U(\theta_{nv}, \phi_{nv})^{+} \begin{bmatrix} v^{eff}_{+,nv}(|r_{nv}|) & 0 \\ 0 & v^{eff}_{-,nv}(|r_{nv}|) \end{bmatrix} U(\theta_{nv}, \phi_{nv})\, \Theta_v(|r_{nv}|) \tag{B.17}$$

Where $\Theta_v(r)$ is unity for $r < S_v$ and zero for $r > S_v$.

The self-consistent density matrix determination issue is commonly solvable through an iteration process employing one of modern approaches to solving the KSE (B.6) with an EP (B.17). In the next section, we briefly describe one of these methods, the ASM method [52, 64].

B.3- Augmented-spherical method:

All modern ways of calculating eigenstats and eigenvectors of the KSE are derived according to variational reasoning and they differ mainly in the choice of the trial functions. The trial functions of the ASW method have the following definition [52]. Suppose that we take an ASW to be centered on R_{nv}. It has various appearances at three distinct areas of space: the atomic sphere around R_{nv} , each of the other atomic spheres, and the interstitial volume. Inside the interstitial volume, the function would be given as follows:

$$\eta_{Lnv\sigma}(r_{nv}) = h_L(r_{nv})\chi_{nv\sigma} \,, \tag{B.18}$$

Where h_L is a spherical Hankel function of some small energy (e.g. - 0.015 Ryd for convenience) and

$$\chi_{nv\sigma} = U_{nv}^{+}\chi_{\sigma} \tag{B.19}$$

Here

$$U_{nv} = (\theta_{nv}, \phi_{nv}), \qquad \chi^{+} = \begin{bmatrix}1\\0\end{bmatrix}, \qquad \chi^{-} = \begin{bmatrix}0\\1\end{bmatrix}, \tag{B.20}$$

This feature (B.18) has a spin projection set σ to the local spin axis of the atom (nv).

A similar property typifies the ASW in the atomic sphere (nv):

$$\eta_{Lnv\sigma}(r_{nv}) = \tilde{h}_{Lnv\sigma}(r_{nv})\chi_{nv\sigma} \qquad \text{if } |r_{nv}| < S_v, \tag{B.21}$$

Where $\tilde{h}_{Lnv\sigma}$ is the solution of the equation

$$\left[-\nabla^2 + v_{\sigma,nv}^{eff}(r)\right]\Phi(r) = E\Phi(r), \tag{B.22}$$

Correlate to the boundary of the sphere r = S_v the magnitude and gradient of the Hankel function $h_L(r)$.

The shape of the ASW at every other sphere is determined by using the expansion [65] from the Hankel function in terms of spherical Bessel functions that are centered on a different atomic position:

$$h_L(r_{nv}) = \sum_{\acute{L}} B_{\acute{L}L}\left(R_{m\mu} - R_{nv}\right) j_{\acute{L}}\left(r_{m\mu}\right) \tag{B.23}$$

For $|r_{m\mu}| < S_\mu$ and $R_{m\mu}$ other than R_{nv}. In equation (B.23), $B_{\acute{L}L}$ are the well known KKR structure factors. Bessel's spherical functions provide a different set of boundary conditions for equation (B.22). Matching solutions will be listed as $\tilde{j}_{Lnv\sigma}$. Now it is possible to define ASW in atom spheres other than (nv):

$$\eta_{Lnv\sigma}(r_{nv}) = \sum_{L\sigma} B_{\acute{L}L}(R_{m\mu} - R_{nv})(U_{m\mu}U^{+}_{nv})_{\acute{\sigma}\sigma}\, \tilde{j}_{\acute{L}m\mu\acute{\sigma}}(r_{m\mu})\chi_{m\mu\acute{\sigma}} \quad \text{if } |r_{m\mu}| < S_\mu \quad \text{(B.24)}$$

The definition of ASW is supplemented by equation (B.24) and equations (B.18) and (B.21). ASW provide an efficient set of basic functions in which to develop solutions of the KSE (B.6):

$$\Psi(r) = \sum_{Lnv\sigma} \mathrm{C}_{Lnv\sigma}\eta_{Lnv\sigma}(r_{nv}) \quad \text{(B.25)}$$

In order to determine the eigenenergies ε and the corresponding expansion coefficients $\mathrm{C}_{Lnv\sigma}(\varepsilon)$ appearing in equation (B.25), we use the Rayleigh-Ritz variational procedure leading to the secular equation.

$$\sum_{\acute{L}\acute{n}\acute{v}\acute{\sigma}}\left(\langle Lnv\sigma|H|\acute{L}\acute{n}\acute{v}\acute{\sigma}\rangle - \varepsilon\langle Lnv\sigma|H|\acute{L}\acute{n}\acute{v}\acute{\sigma}\rangle\right)\mathrm{C}_{\acute{L}\acute{n}\acute{v}\acute{\sigma}}=0, \quad \text{(B.26)}$$

Where $\langle ... | ... \rangle$indicates integration over all space and according to equations (B.6) and (B.17).

$$\mathrm{H}=-\nabla^2 I + \sum_{nv} U(\theta_{nv},\phi_{nv})^{+}\begin{bmatrix} \mathrm{v}^{eff}_{+,nv}(|r_{nv}|) & 0 \\ 0 & \mathrm{v}^{eff}_{-,nv}(|r_{nv}|) \end{bmatrix} U(\theta_{nv},\phi_{nv})\Theta_{\mathrm{v}}(|r_{nv}|) \quad \text{(B.27)}$$

The subsequent derivation of matrix elements in equation (B.26), while simple, leads to rather complex expressions that do not need to be reproduced in this thesis. The general structure of the expressions is close to that of the standard ASW [64]. Notice that in equation (B.25), no periodicity in magnetic structure has been assumed. The presence of periodicity satisfies the requirements of the Bloch theorem and makes it possible to use the Bloch sums of the ASW as trial functions. This results in the factoring of the secular matrix and an essential simplification of the calculations.

B.4- Constrained magnetic moments

The standard DFT calculation provides information on the state of a system at a minimum total energy. Among other things, we obtain the equilibrium value of the atomic magnetic moments. Also, despite a wide range of applications, it is of great interest to estimate the total energy depending on the length and direction of the magnetic moments. Dederichs *et al.* [65] proposed that as part of the DFT the total functional energy (B.4) could be minimised subject to the stress imposed on the spin density:

$$\int m(r)dr = m_{nv}\,, \tag{B.28}$$

It refers to the vector of the atomic moment which has a specific value (Ω_{nv} is the atomic volume of the (nv) th atom). This results in functional minimization

$$\tilde{E}[\rho] = E[\rho] - \sum_{nv} B_{nv}(\int m(r)dr - m_{nv}), \tag{B.29}$$

Where $E[\rho]$ is given by equation (B.4); B_{nv} are Lagrange multipliers. The Euler-Lagrange equation for this function results in a single-particle Hamiltonian effective form.

$$\mathrm{H}=-\nabla^2 I + \sum_{nv}\left[\frac{1}{2}\left(\mathrm{v}^{eff}_{+,nv}(|r_{nv}|) + \mathrm{v}^{eff}_{-,nv}(|r_{nv}|)\right) I + \frac{1}{2}\left(\mathrm{v}^{eff}_{+,nv}(|r_{nv}|) - \mathrm{v}^{eff}_{-,nv}(|r_{nv}|)\right) e_{nv}\cdot\sigma - B_{nv}\cdot\sigma\right]\Theta_{\mathrm{v}}(|r_{nv}|), \tag{B.30}$$

Where we employed a notation of the potential with a form that differed from the equation (B.27) by introducing exactly the unit vector e_{nv}, along the direction of atomic momentum; σ is the vector of the Pauli spin matrices. With the exception of the word $B_{nv}\cdot\sigma$, this refer to Hamiltonian (B.27). So in order to minimize the constrained function (B.29), we have to find the value of the vectors B_{nv} which equalize the magnetic arrangement determined from equation (B.28). Since usually both the directions of the vectors e_{nv} and B_{nv} are not coinciding, the supplementary term $B_{nv}\cdot\sigma$ may bring fundamental obstacle of the computational scheme [66], This is not necessarily do this once the symmetry of the problem oppress the e_{nv} and B_{nv} vectors are collateral.

For the latter, equation (B.27) shall be changed to

$$H = -\nabla^2 I + \sum_{nv} U(\theta_{nv}, \phi_{nv}) \begin{bmatrix} \mathrm{v}_{+,nv}^{eff}(|r_{nv}|) - B_{nv} & 0 \\ 0 & \mathrm{v}_{+,nv}^{eff}(|r_{nv}|) + B_{nv} \end{bmatrix} U(\theta_{nv}, \phi_{nv}) \Theta_{\mathrm{v}}(|r_{nv}|),$$

(B.31)

and the ASW scheme is allowed to apply to this case directly following an inflexible shifting of local potentials. The values of B_{nv} have to be varied once the desired value of the atomic momentum length is attained. Considering the most simple shape of a constrained length through a magnetic moment into a ferromagnet state, such problem may be resolved by the so-called FSM [67]. The FSM employs to the effect that in ferromagnetics the spin projection has a good quantum number and all electron states may be partitioned as SU and SD states. Moreover, due to the parallelism of the atomic moments, all the stabilizing fields are aligned along a common direction. We may therefore consider the situation as a global field B related to the entire crystal. The B field leads to simply a relative displacement of the SU and spin-down states. The required magnetic moment m may be attained by fixing B = 0 while calculating the band structure but by separately the SU Fermi energy $E_{\mathrm{F}+}$ and the SD Fermi energy $E_{\mathrm{F}-}$, so that the following is obtained:

$$\int N_+(\varepsilon) d\varepsilon - \int N_-(\varepsilon) d\varepsilon = m, \tag{B.32}$$

This is because the left integral sum of the cell is neutral. Here, N+ and N- represent the spin density of states (DOS) to be obtained from a self-consistent method. For the fundamental ground-state value of the magnetic moment, both Fermi energies are equal, naturally. Consequently, in order to apply the FSM, it is necessary to satisfy two criteria: the separation of the SU and SD states and the parallel nature of the local constraining fields. These conditions are not satisfied in the case of a NC magnetic structure (or even AFM). As a result, there is no possibility of reducing of the effect of constraining fields into the rigid shift of the DOS computed with no fields. Thus, the work with the Hamiltonian incorporating the B_{nv}

fields is required (A more extensive discussion and a few technical hints may be found in [55, 65]).

B.5- Relativistic effect :

We have excluded in the above sections the relativistic effects that can be highly significant in terms of heavy magnetic element properties. The fundamental principles of NR DFT can be applied easily in this context. The actual energy state of the relativistic system is found as a function of the four-current density [68, 69]. A simple variational procedure can obtain a straightforward derivation of the Kohn-Sham-Dirac equations. Regrettably, there is no local approximation available for the current density functional [70] and the resulting equations after modification are very complicated. The conventional approximation agreed in nearly every DFT application for relativistic magnetic electron systems has relied on Gordon's decay of current and ignoring of terms yielding to diamagnetic effects. While no major obstacles arise in using the Kohn-Sham-Dirac equation to study NC magnetism, this schematic necessitates the extensive redesign of software packages.

As a consequence, the majority of calculations have been carried out by using another schema that relies on the breakdown of Dirac's equation according to the 1/c where c is the velocity for light and dealing individually with SOC and all other relativistic corrections. This is done with the SR equation containing the entire relativistic correction excluding SOC. It offers the benefit of keeping the "NR" quantum numbers that is spin projection σ, orbital quantum number *l*, and magnetic quantum number *m*, as the proper quantum numbers for the electron states in spherically symmetric potential.

Now, it is necessary to add the SOC coupling. This correction for a spin-polarized spherically symmetrical potential may be described in the following form [71]:

$$H_{so} = \frac{1}{(2)^2}\frac{1}{r}\left(\begin{bmatrix} \frac{1}{M_+^2}\frac{dv_+}{dr} & 0 \\ 0 & \frac{1}{M_-^2}\frac{dv_-}{dr_v} \end{bmatrix}\sigma_z\hat{L}_z + \frac{1}{M_{av}^2}\frac{dv_{av}}{dr_v}\left(\sigma_x\hat{L}_x + \sigma_y\hat{L}_y\right)\right) \quad \text{(B.34)}$$

Where

$$v_{av}(r) = \frac{1}{2}[v_+(r) + v_-(r)] \quad \text{(B.35)}$$

And

$$M_\alpha = \frac{1}{2}(1 - c^2 v_\alpha), \qquad \alpha = av, +, - \quad \text{(B.36)}$$

The form of the spin-orbit Hamiltonian from [72] has been used in Eqs. (B.34)- (B.36), slightly changed to take into consideration that the electrons are spin-polarized. If important, such a term can be discussed in the context of the perturbation theory or more consistently as part of this Hamiltonian at the stage of the variational determination of crystal states with the trial functions ascertained in the SR mode. All computations discussed below were done under the variational framework.

The calculations performed for different U composites (e.g., [73]) revealed that the traditional form of the DFT, taking the SOC into consideration, was unable to replicate experimental atomic moments for the U atom. This is due to the underprediction of the orbit part of atomic momentum. This is explained by the underestimation of the orbital part of the atomic moment. According to Eriksson et al [73], in calculations of U compounds, we add to the Hamiltonian of the problem the term

$$\hat{H}_{orb}=I_{orb}L_z\hat{L}_z, \quad \text{(B.37)}$$

This accommodates interactions that are responsible for Hund's second rule requiring maximization of the orbital moment. At this point, *L z* represents the atomic orbital moment projection upon the local atomic *z* axis. The I_{orb} parameter, employed through the following sections, was assumed to be equal to 2.6 mRyd in order to reproach the 5f atomic data [72].

Part C :

Monte Carlo simulation

MC is fundamentally defined as a problem-solving technique that admits probabilistic interpretation. It is part of a package of computational algorithms based on repeated random sampling to obtain equilibrium numerical results. This type of simulation has proven its usefulness in the study of systems with many coupled degrees of freedom, such as strongly coupled solids, fluids and disordered materials. It is interesting to note that MC are commonly used in other fields than physics such economics, medicine, and others.

The main goal of MC is to track the evolution of a model as a function of time, this time dependence is directly related to the MC step, which forms the basis of the process in which the model evaluates to the equilibrium state according to a sequence of random numbers generated during the simulation. MC is based on the numerical resolution of systems by using a stochastic process, and is therefore, the most important class of numerical techniques used to solve problems in statistical physics in either equilibrium or out-of-equilibrium cases.

C.1- basic concept of the Monte Carlo method:

Consider a spin system described by the Hamiltonian H. The mean value of a quantity A can be written as:

$$\langle A \rangle = \frac{\sum_x A(x) e^{-\beta E(x)}}{Z}$$

Where the sum is carried out over all the configurations x of energy E(x) and $\beta = 1/kT$, k being the Boltzmann constant and T representing the temperature. Z is the system partition function, it is given by:

$$Z = \sum_x e^{-\beta E(x)}$$

The simplest way to calculate the partition function is to attempt to generate all possible spin configurations of the system, step by step, on a computer. But what must be remembered is

that even for an Ising spin 1/2 model, the number of possible configurations is 2^N where N is the N number of sites. This procedure has been adopted by several authors, but it could only be implemented for small sizes reaching N = 3 x 3 x6 = 54 [74].

But when dealing with critical phenomena, we are mainly interested in the thermodynamic limit N →∞, since finite systems do not exhibit a phase transition. Systems with size N < 64 are certainly very small to give useful information about phase transitions. It is therefore only possible to generate a number, as large as possible, of configurations, but not all of them. The general idea behind MC is to randomly choose (sampling), points in the configuration space and performing the desired sums. We obtain therefore, a Monte Carlo approximation ⟨A⟩ of a thermodynamic quantity A by:

$$\langle A \rangle = \frac{1}{M} \frac{\sum_{i=1}^{M} A(x_i) e^{-\beta E(x_i)}}{\sum_{i=1}^{M} e^{-\beta E(x_i)}}$$

Where M is the number of configurations generated by the MC method. Another difficulty arises at this level. Because of the very large variation of the exponential in 2.3, the majorities of the generated configurations have only a negligible contribution and are therefore not characteristic of the state in question.

C.2- Description of the method:

The Monte Carlo method introduced by Metropolis et al. [75] is based on the idea of importance sampling [76-77] as opposed to random sampling. The states x_i are not taken randomly, but are selected from the region of the phase space from which the most important contributions of the sum 2.3 come. It would then be more convenient to choose the configurations with a probability equal to their Boltzmann weights:

$$p(x_i) = \frac{e^{-\beta E(x_i)}}{Z}$$

This gives the estimate:

$$\overline{A} = \frac{1}{M}\sum_{i=1}^{M} A(x_i)$$

The problem is that the partition function Z in equation 2.4 is not known. The usual solution consists in forming what is called a Markov chain of configurations x_t by introducing an active dynamic with a "time" t (the real statistical system is in equilibrium and independent of time). This approach gives, in the limit M→∞, configurations with probabilities 2.4.

Let P(X,t) be the probability for the system to be in state X at time t and W(X →Y) the probability of transition from configuration X to configuration Y . So it can write as:

$$P(X, t+1) = P(X, t) + \sum_{Y} [W(Y \to X)P(Y, t) - W(X \to Y)P(X, t)]$$

For t sufficiently large, i.e. when we move away from the initial configuration, we can assume that P(X,t) →P(X). And we can write a sufficient condition to have a probability of equilibrium that we call condition of the detailed balance in the form:

$$W(X \to Y)P(X) = W(Y \to X)P(Y)$$

If we choose for P(X) the Boltzmann distribution 2.4, we obtain:

$$\frac{W(X \to Y)}{W(Y \to X)} = \frac{P(Y)}{P(X)} = \frac{e^{-\beta E(Y)}}{e^{-\beta E(X)}}$$

This becomes, by setting $\Delta E = E(Y) - E(X)$:

$$\frac{W(X \to Y)}{W(Y \to X)} = e^{-\beta \Delta E}$$

It is a condition in its general form, and any transition probability $W(X \to Y)$ which satisfies it can be considered in MC. However, few expressions obeying equation 2.8 are used in the literature and we will see some of them in the next section.

C.3- Metropolis algorithm:

As mentioned above, the condition of the detailed balance can be satisfied by several choices of the transition probabilities W. In this regard, Metropolis et al. offered a very simple choice

$$W(X \to Y) = \begin{cases} e^{-\beta \Delta E} & \text{if } \Delta E > 0 \\ 1 & \text{if } \Delta E \leq 0 \end{cases}$$

So if $E(Y) > E(X)$,

$$\frac{W(X \to Y)}{W(Y \to X)} = \frac{e^{-\beta(E(Y)-E(X))}}{1} = e^{-\beta \Delta E}$$

And in the case $E(Y) \leq E(X)$:

$$\frac{W(X \to Y)}{W(Y \to X)} = \frac{1}{e^{-\beta(E(X)-E(Y))}} = e^{-\beta \Delta E}$$

So in both cases Metropolis choice 2.9 satisfies the detailed balance condition.

Other possible choices of $W(X \to Y)$have been adopted by other authors. For example, Glauber [78] used the expression:

$$W(X \to Y) = 1 - \tanh[2\beta(E(Y) - E(X))]$$

In general, an MC simulation procedure can be said to constitute a valid Monte Carlo algorithm if it satisfies the following two crucial conditions:

- Have a way to generate any configuration Y from another configuration X such that the transition probability $W(X \to Y)$ satisfies the detailed balance condition.
- The process of generating configurations from each other must be ergodic, i.e. each configuration can be reached from any other configuration by performing a finite number of iterations.

The Metropolis algorithm satisfies the first condition for all systems. While the second condition depends on the model and is not always satisfied. In fact, the Metropolis algorithm does not specify how the transition from one configuration to another should be done. It only imposes that any change proposed must be accepted with a probability that depends on the

variation of energy. For the Ising model, the obvious change in configuration is to flip (flip) a spin. If we try to flip several spins at the same time, the value of ΔE would be large and the probability of accepting the change $e^{-\beta\Delta E}$ would be very low. For the one-spin flip, ΔE depends only on the spin of the current site and its neighbors. So the update of the spins takes on a local character. This characteristic of the Metropolis algorithm poses several problems in the vicinity of the transition points as we will see later.

CHAPTER 3
Structural, electronic, magnetic, and magnetocaloric properties in intermetallic compound TbCu2Si2

Introduction

The area of cooling occupies a prominent position, whether in domestic or commercial applications; it is employed in numerous tasks like food and medical storage, which results in a growing requirement of refrigeration [79]. Traditional technologies utilized for refrigeration have been based on thermodynamics principles. Despite being a cheap and robust technology, it is environmentally hazardous owing to the usage of coolants which include hydrofluorocarbons (HFCs), chlorofluorocarbons (CFCs) and ammonia (NH3) [80,81]. Consequently, from an environmental friendly point of view, future cooling research is turning to other alternative technologies, like magnetic cooling, which is based on the magnetocaloric effect that is an intrinsic feature of magnetic materials. It is based on the concept of heating or cooling of a material by means of a magnetic field [82, 83]. In addition, there are economic, ecological and environmental benefits of this technology; it has no air pollutants or noise, and offers significantly energy efficiency otherwise the Peltier effect or a conventional thermodynamic cycle [84]. Also, some materials like Heusler alloys [85], $LaMnO_3$ [86], $TbCo_2$ [87], $Mn_5Ge_{3-x}Si_x$ [88], MnNiGa [89], Mn_3XC (X=Al, Ga) [90-91], have been the focus of intense research in this area owing to their intense magnetocaloric effect, as well as because of their temperature transition near to room temperature, and to their low cost compared to gadolinium [85]. Currently, there has been considerable popularity in the field of refrigeration for the ternary intermetallic compounds of series RT_2X_2 (R= rare earth, T= transition metal, X= Si or Ge) because of several advantageous characteristics including: superconductivity, magnetism, mixed valence, heavy fermions and kondo behavior. Such a structure is forming as a natural layered structure where the planes of rare earth elements are separate of the layers containing the transition metals [92,93]. Those compounds which belong in this group are believed as the successful applicants in the magnetic refrigeration process engineering [95-101].

In this chapter, we have investigated the structural, electronic, magnetic and magnetocaloric properties of the intermetallic compound $TbCu_2Si_2$, applying theoretical techniques including density function theory and MC. The magnetic properties of the intermetallic compound $TbCu_2Si_2$ were determined through a second order transition from its AFM state into the PM state near T_N ~8 K. In addition, the giant magnetocaloric effect was found under a magnetic field at h=2T. The highest values of ΔS_M and RCP were found to be 40.78J/Kg.K and 71.58J/K, respectively. On the other hand, the magnetocaloric properties obtained for this compound are best in comparison with those of gadolinium [85]. Based on this reason, it may be proposed as a suitable choice for applications in magnetic refrigeration near T_N [94].

3.1- Crystalline Structure of intermetallic $TbCu_2Si_2$ compound:

The $TbCu_2Si_2$ intermetallic materials are characterized by a tetragonal crystalline structure similar to the compound $ThCr_2Si_2$-type, see **Fig. 14.** The computed lattice and atom position parameters are presented below in Table 4. It is apparent that the achieved result agrees well within experimental parameters [100].

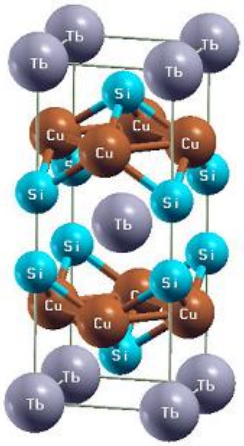

Figure 14: Unit cell structure of TbCu2Si2

3.3- Electronic properties of the intermetallic $TbCu_2Si_2$:

On the basis of these data, the density of states reveals the metallic aspect of the composite; the atom Tb possesses a powerful magnetic moment because of the unsymmetry between the spin-up and spin-down states. Meanwhile, the majority of the spins in the Fermi level are downward. (see **Fig. 15**).

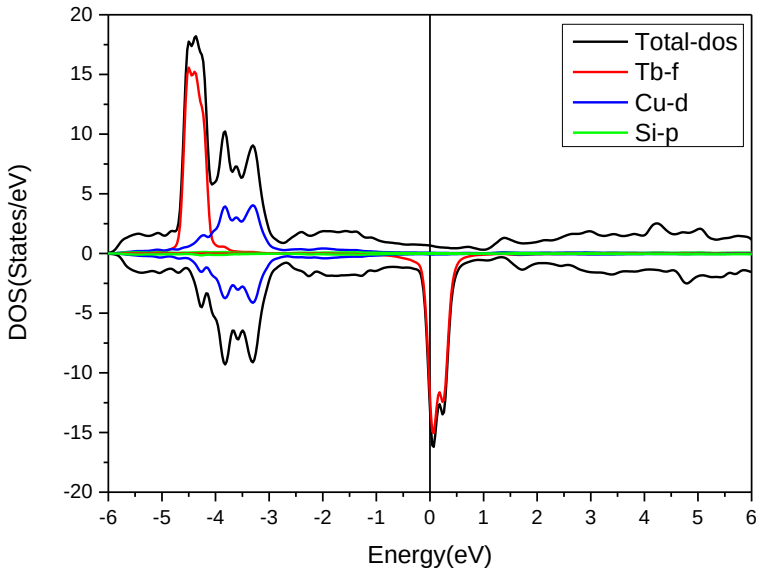

Figure 15: Total and partial electronic DOS of TbCu2Si2 compound

The band structure calculation of the intermetallic $TbCu_2Si_2$ compound have been performed by using GGA along the high symmetry **GAMMA**, **H**, **N**, **GAMMA**, **P** directions of Brillouin zone for SU and SD (see **Fig. 16**) [102-104]. There is no energy gap in the Femi level, which indicates the metallic behavior; the spins down states are closer to each other than the spin-up states in the Fermi level (see **Fig 16** (a) and (b)). However, the intermetalicity for this system is due to Tb-4f states. We can conclude that the close states allow an easy mobility of electrons which influence the conductivity of the system.

The values of magnetic moment of Tb, Cu and Si atom are found to be $5.93\mu_B$, $0.01\mu_B$ and $-0.005\mu_B$ respectively. The Tb atom's magnetic moment ($\mu_{eff}=5.93\mu_B$) is far away with the experimental value ($\mu_{eff}=8.6\mu_B$) his discrepancy is maybe originated to the DMI [94].

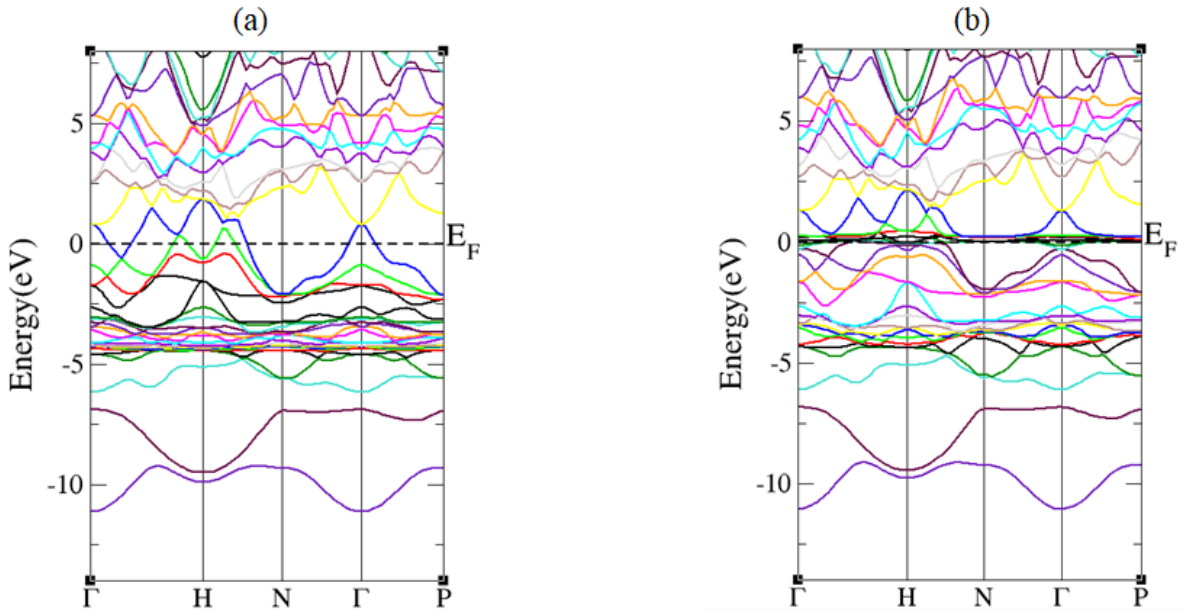

Figure 16: Band structures of TbCu2Si2 compound with GGA approximation. (a) SU and (b) SD

3.4- Magnetic ground state:

Firstly, we begun by magnetic Calculation, four magnetic configurations have been calculated FM, AFM1, AFM2, AFM3) (see **Fig. 17**). As can be seen in **Table 1**, the AFM1 states more stable than FM state.

	Total energy (Ry)
FM	-249749.68820881
AFM1	-249749.68850159
AFM2	-249749.68666943

AFM3	-249749.68500345

Table 1:Magnetic configurations and total energy of each magnetic configuration

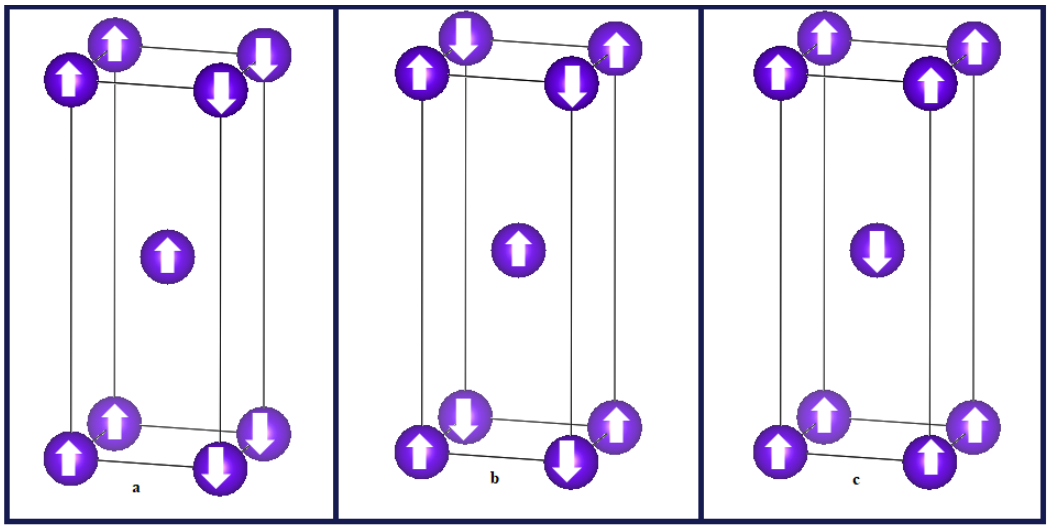

Figure 17: Considered magnetic states of TbCu2Si2: (a) AFM 1, (b) AFM 2 and (c) AFM 3

3.5- Magnetic Hamiltonian:

We used the Ising model to describe the magnetic structure of **$TbCu_2Si_2$**. Our Hamiltonian takes into interest the magnetic exchange couplings between nearest neighbors and an external magnetic field as shown in **Fig. 18**:

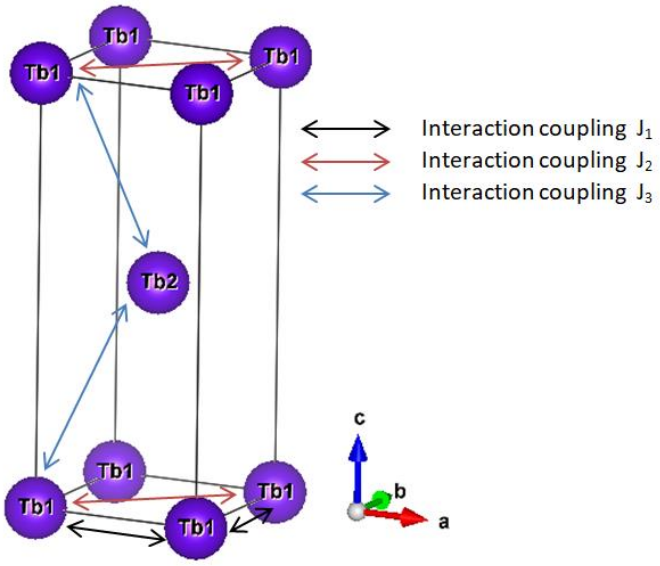

Figure 18: the magnetic structure of TbCu2Si2

The Hamiltonian of the system is given by:

$$H = -J_1 \sum_{<i,j>} S_i S_j - J_2 \sum_{<i,j>} S_i S_j - J_3 \sum_{<i,k>} S_i S_k - \Delta \sum_i (S_i)^2 - h \sum_i S_i \quad (3.1)$$

Where <i,j> and <i,k> represent the first, second and third neighbors between $S_i - S_j$ and $S_i - S_k$, which take the values $\pm 3; \pm 2; \pm 1; 0$. The exchange coupling interactions : $J_1, J_2 \; and \; J_3$ are the parameters between the first, second and third nearest neighbors respectively. Δ and h are the crystal field and the external magnetic field, respectively.

The parameters (J_1, J_2 and J_3) and the crystal field (Δ) have been investigated using Ab-initio calculations with applying the following Eqs. (3.2, 3.3)[90, 91].

$$J_1 = \frac{E_{anti2} - E_{ferro}}{Z_1 S_i S_j} \qquad J_2 = \frac{E_{anti1} - E_{anti2}}{Z_2 S_i S_j} \quad (3.2)$$

$$J_3 = \frac{E_{anti3} - E_{ferro}}{Z_3 S_i S_j} \qquad \Delta = \frac{E_a}{\sum_i (S_i)^2} \quad (3.3)$$

where $E_{ferro}, E_{anti1}, E_{anti2} \; and \; E_{anti3}$ are the energies of FM, AFM type 1, AFM type 2 and AFM type 3 configurations (see Fig. 17(a), (b) and (c)), respectively, $Z_1 = 4, Z_2 = 4 \; and \; Z_3 = 8$ are the numbers of first, second and third nearest neighbors, respectively.

E_a is the magnetic anisotropic energy which is equal to the difference of the energy between the low and high energy positions.

On the other hand, we have performed the exchange coupling interactions (J_1,J_2,J_3) and the crystal field (Δ) of the intermetallic $TbCu_2Si_2$ compound using Ab-initio calculation with the following values J_1=0.58 meV, J_2=-0.69 meV and J_3=0.41 meV $\Delta = 0.003$ meV.

3.6- Magnetocrystalline anisotropy :

The most significant metric of the rare earth intermetallic material RT_2X_2 is the MAE. This is the energy needed to realign magnetization from the desired direction toward another possible direction in space. Throughout this study, the SOC was incorporated into ab initio calculations of total energy for spin re-directed alongside both the easy axis magnetization (Ea) and the hard axis magnetization (Ha) within the second variational framework. In order to determine MAE, we applied the DIPAN tool implemented inside WIEN2K (see Table 2). On the whole, the minimal energy range is found to be along the [110], [100], and [010] directions, as might expect from a tetragonal symmetry. The magnetic moment has been found lying on the basal plane, perpendicular to the tetragonal c-axis, which is consistent with the experimental guidance [105-106].

Direction			Energy (J/m^3)
X	Y	Z	
0	0	1	$0.1741515\ 10^{05}$
0	1	0	$-0.8707574\ 10^{04}$
1	0	0	$-0.8707574\ 10^{04}$
1	1	0	$-0.8707574\ 10^{04}$
1	1	1	$0.1107757\ 10^{05}$
0	1	1	$0.1380891\ 10^{05}$

1	0	1	0.1380891E+05

Table 2:Energies for the different directions of TbCu2Si2.

3.7- Magnetocaloric effect:

The first records on the magnetocaloric effect start in 1881, where it was discovered by German physicist Emil Gabriel Warburg (1846-1931). In these studies with iron-containing alloys (Fe) it was observed that in the presence of the field, the sample released heat, on the other hand, when removed the field absorbed heat. Thus, from a change in the field a change in thermal energy was obtained. A few years later (specifically in 1905) it was demonstrated by the French physicist Paul Langeving that by making a change in the PM magnetization a reversible change in temperature was obtained. But it was only in 1918 when Pierre Weiss and August Piccard published the first publications that scientifically explained the magnetocaloric effect. It was only to be expected that the alignment and misalignment of the spins when in the presence of an external magnetic field would be the main reason for the magnetocaloric effect. We now know that the explanation for the ability of magnetic materials to absorb and release heat goes beyond the alignment and misalignment of the spins; it must also be taken into account the changes in the lattice of atoms. Therefore, a well-accepted explanation is that when materials are subjected to a magnetic field under adiabatic conditions (thermally isolated from the environment) the electron spins align in the same direction as the applied field. This ordering implies a decrease in entropy or disorder in the physical system. As there is no heat exchange with the environment, the total entropy of the system must remain constant. On the other hand, under these conditions, the atoms or molecules of the material tend to shake to compensate for the alignment of the spins. So, by the second law of thermodynamics, we have that the greater the disorder, the greater the atomic agitation, and the temperature of the material increases. Thanks to all these discoveries, more recently, in

1976, the prototype of a magnetic refrigerator operating at room temperature has been designed. This is an important step in the history of magnetic refrigeration. The creator Gerald V, brow of NASA proposed in his classic article "Magnetic heat pumping near room temperature" the use of rare earth gadolinium (Gd) as the cooling material. This prototype operated in isothermal steps at room temperature under the action of a magnetic field of 70 kOe. Another magnetic refrigeration prototype was developed in 1987 by researcher Lance Kirol of the Idaho National Engineering Laboratory in the United States of America. His machine used 270 grams of pure Gd subjected to a magnetic field of 10 kOe. After four cycles, the temperature was reduced, thus proving once again the possibility of having a magnetic refrigerator operating at room temperature. However, the obstacle to the continuation of these projects was the production of electromagnets which are very expensive and difficult to transport. At a later time, researchers Gschneidner and Pecharky made an important discovery of new material with better properties compared to pure gadolinium (Gd). This novel material, Gd_5SiGe_2, became widely known for being the first among several new classes of materials with giant EMC, which exhibited the entropy change of 20 J/kg.K and the temperature change of 15 K at H= 50 kOe. This study was supported by several investigations involving other materials for application in the field of magnetic refrigeration. After this initial work, Gschneidner and Pecharky obtained greater effects by varying the concentration of Si and Ge. Some of the compounds already studied that showed a giant EMC include $Tb_5Si_2Ge_2$, $La_{0.5}Pr_{0.5}Fe_{11.5}Si_{1.5}$, MnAs, and derived compounds such as $MnAs_{1-x}Sb_x$, $Mn_{1-x}Fe_xAs$, and also Heusler alloys such as Ni-Mn-In-(Co), Ni-Mn-In and $Ni_2Mn_{0.75}Cu_{0.25}Ga$. Another aspect to note is that in addition to room temperature magnetic cooling, another application of EMC would be low-temperature cooling which would have countless other applications, for example in the liquefaction of various gases as well as in advanced quantum computing technology. This would allow the development of refrigerators capable of

operating at increasingly lower temperatures, which would significantly reduce the costs of current cryogenic refrigerators used in laboratories and space applications. Thus, among the variety of materials studied for application in magnetic refrigeration, in different temperature ranges, we may highlight binary and ternary compounds, which exhibit transitions of RT_2, RT_5, RTX, and RT_2X_2 where R = rare earth, T = transition metal, and X = semi-metal. All these results indicate that research in the field of magnetocaloric is far from saturated.

3.8- The thermodynamics of the Magnetocaloric effect:

The EMC may be quantified by two parameters, they are the adiabatic temperature variation (ΔT_{ad}) and the isothermal entropy variation ($-\Delta S_M$). Although, the only ΔT_{ad} may be obtained from experimental measurement that provides the variation of temperature that a magnetic material has under an adiabatic process. However, it is difficult to idealize in this condition. An alternative way of obtaining $-\Delta S_M$ is by indirect measurements via calorimetric techniques. On the other hand, it may be gained from both magnetic and calorimetric measurements. Furthermore, it is important to notice that the magnetocaloric effect and even the barocaloric effect (in this case the external parameter is pressure) are the result of the first and second principle of thermodynamics. In this perspective, in order to determine the quantities that characterize the magnetocaloric effect, a thermodynamic description is necessary. Suppose that a material is subject to a variation of field and a reversible heat exchange which results in a magnetic work. Therefore, in that process, the entropy of the material (S), changes over time as a function of temperature (T), magnetic field (H) and pressure (p). In this case:

$$S=S\,(T, H, p) \tag{3.4}$$

By taking the differential of the entropy over T, H and p we obtain eq. (3.5):

$$dS(T,H,p) = \left(\frac{\partial S}{\partial T}\right)_{H,p} dT + \left(\frac{\partial S}{\partial H}\right)_{T,p} dH + \left(\frac{\partial S}{\partial p}\right)_{T,H} dp \quad (3.5)$$

During isothermal and isobaric processes in which dT = 0 and dp = 0, eq. (3.5) can be represented as follows:

$$dS = \left(\frac{\partial S}{\partial H}\right)_{T,p} dH \quad (3.6)$$

By using one of Maxwell's fundamental relations the following equation is obtained:

$$\left(\frac{\partial S}{\partial H}\right)_{T,p} = \left(\frac{\partial M}{\partial T}\right)_{H,p} \quad (3.7)$$

By substituting it in equation (3.6) we obtain:

$$dS_M = \left(\frac{\partial M}{\partial T}\right)_{H,p} \mathrm{dH} \quad (3.8)$$

By varying the magnetic field from H_i to H_f, upon integrating eq. (3.8) it provides the variation of entropy of the total system, which is given by:

$$\Delta S_M(T,\Delta H) = S_T\left(T,H_f,p\right) - S_T(T,H_i\,,p) = \int_{H_i}^{H_f}\left(\frac{\partial M}{\partial T}\right)_{H,p} dH \quad (3.9)$$

So according with Pecharsky and co-workers with the resolution of eq. (3.9) we will obtain the isothermal variation of entropy by numerical integration approach which is described as:

$$\Delta S_M(T_{av})_{\Delta H} = \int_{H_i}^{H_f}\left(\frac{\partial M(H)_{T_{av}}}{\partial T}\right)_H dH = \frac{1}{2\,\partial T}\left(\partial M_1 \partial H_1 + \sum_{k=2}^{n-1} \partial M_k \partial H_k + \partial M_n \partial H_n\right) \quad (3.10)$$

where ΔH denotes the magnetic field change, T_{av} is the average of the temperatures T_u and T_v of two isothermal magnetization curves, $\partial H = H_k - H_{k-1}$, is the spacing of measurements, $\partial T = T_v - T_u$ and $\partial M_k = M\ (H_k,T_v)$ -, $M\ (H_k,T_u)$ is the change in magnetization between temperatures T_u and T_v measured with H_k and n is the number of points measured for each of

two isotherms. Furthermore, from eq. (3.9) we can see that the amplitude of ΔS_M is larger near the magnetic phase transitions.

Another way to obtain EMC is by indirect measurements of specific heat (C_p) in two different magnetic fields, at H_i and H_f. According to the second law of thermodynamics, the specific heat can be described as follows:

$$C_p(T,H) = T\left(\frac{\partial S}{\partial T}\right)_{H,p} \tag{3.11}$$

By integrating eq. (3.11) over temperature, we obtain the entropy under a magnetic field H at an isobaric process (dp = 0) as follows:

$$S(T,H) = \int_0^T \frac{C_p(\acute{T},H)}{\acute{T}}_{H,p} d\acute{T} + S_0 \tag{3.12}$$

In this way, we obtain:

$$\Delta S_M(T,\Delta H) = \int_0^T \left(\frac{C_p(\acute{T},H_f) - C_p(\acute{T},H_i)}{\acute{T}}\right)_{H,p} d\acute{T} \tag{3.13}$$

Thus, the value of ΔT_{ad} can be determined by means of the difference between the curves of entropy per temperature at H_i and H_f that are given by:

$$\Delta T_{ad} = T(S)_{H_f} - T(S)_{H_i} \tag{3.14}$$

Figure 19 shows in a general way the total entropy curves as a function of temperature for the magnetic fields Hi and Hf (in this case we consider Hi the null field represented by the red line and Hf as being a non-zero field in the black line).

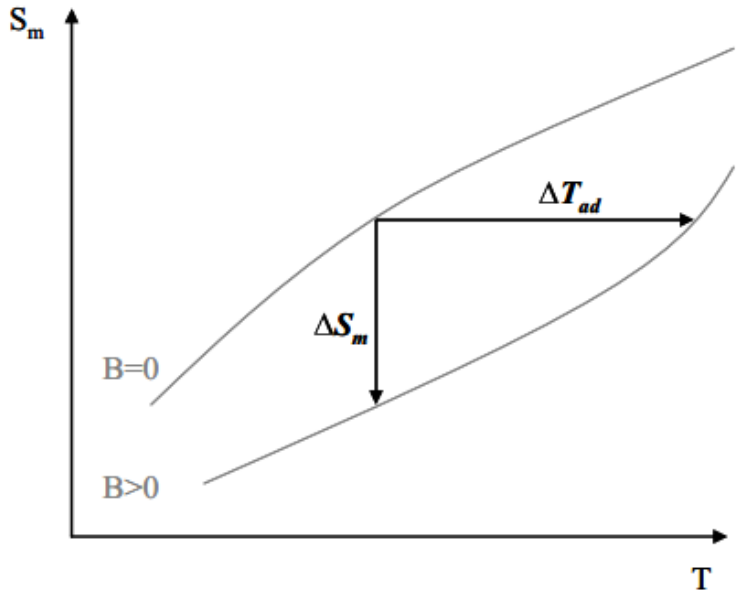

Figure 19: Representation of the thermodynamic principle of the magnetocaloric effect

The ΔS and ΔH indicate the entropy and magnetic field variations between the two phases. Thus, the Clausius-Clapeyron equation is written as follows:

$$\Delta S = -\Delta M \frac{dH_i}{dT_i} \tag{3.15}$$

But for the case of the indirect measurements from magnetization data, the EMC can be calculated by numerically solving eq. (3.16):

$$\Delta S_M(T,H) = \int_{H_1}^{H_2} \left(\frac{\partial M}{\partial T}\right) dH = \sum_i \frac{\Delta M_i \Delta H_i}{\Delta T_i} \ (J/Kg.K) \tag{3.16}$$

The product of the numerator is the area between two consecutive isotherms on an M-H graph and is the temperature difference between them. In this way, we find where T' is the measure of temperatures between two isotherms.

In addition to $-\Delta S_M$ and ΔT_{ad}, other important EMC quantities are relative cooling capacity (RCP) and refrigerant capacity (RC). These quantities are used to analyze the efficiency of a material magnet in a thermomagnetic cycle. Therefore, RC and RCP will give us quantitatively the amount of heat transferred between the hot and cold sources in an ideal

cooling cycle. According to Gschneidner et al, the RC is calculated from the area of the peak under the curve of ΔS_M vs T as:

$$RC = \int_{T_1}^{T_2} |-\Delta S_M(T)|\ dT\ \left(\frac{J}{Kg}\right) \quad (3.17)$$

Where T_1 and T_2 are the temperatures of the hot and cold sources, respectively, and ΔS_M is the variation of magnetic entropy with temperature. The RCP is defined as. The product of the maximum peak value of $|-\Delta S_M|^{max}$ by full width at half maximum δT_{FWHM} as:

$$RCP = |-\Delta S_M|^{max}.\delta T_{FWHM}\ \left(\frac{J}{Kg}\right) \quad (3.18)$$

3.9- Result and discussion:

Here on **Fig. 20**, we draw the susceptibility change vs temperature, for given values of the exchange coupling interactions: J_1=0.58 meV, J_2=-0.69 meV, J_3=0.41 meV, Δ=0.003 meV and h =0.0T. This figure displays a significant peak near T_N ~8K, which agrees very well with the results of experiments [107, 108] (see **Table 3**).

	Experimental studies	MC simulations
T_N of $TbCu_2Si_2$ compound	13K[105]	8K[94]
	12K[106]	

Table 3: The comparison between the experimental critical temperature and that obtained by using the MC

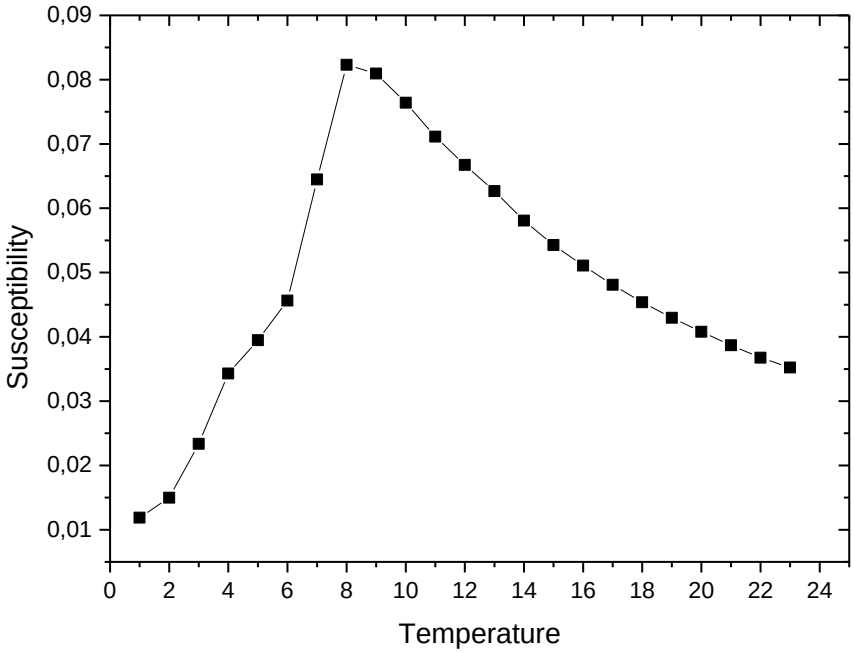

Figure 20: The behavior of the susceptibility as a function of the temperature of the TbCu2Si2 compound, for h= 0.0 T, J1=0.58 meV, J2=-0.69 meV and J3=0.41 meV

Figure 21 illustrates the temperature response of $-\Delta S_{mag}$ under various magnetic fields of h=1.0 T, 1.5 T and 2.0 T. Evidently, as we are raising h, there is progressive increasing in the value of $-\Delta S_{mag}$ and it achieves the maximum value about 47.80 J/kg. K for h=2.0 T. It can clearly see that as we Increase magnetic field, T_N shifts toward the lowest temperature, such behavior has been found on [107], where T_N shifted from 19K to 16K, being in good accordance to experimental reported result. Whereas, as we increase this field of 0.5 steps, the value of ΔS_{mag} grows, proving the importance of that material being a good applicant towards a magnetocaloric application, thus we would not have the need of using a high external field to obtain a great magnetocaloric effect.

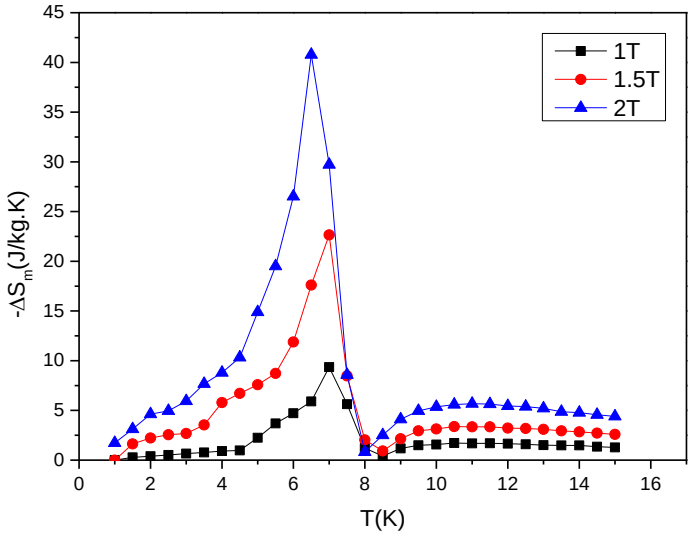

Figure 21: ΔS_M of TbCu2Si2 compound as a function of temperature under different Magnetic fields of 1.0 T, 1.5 T and 2.0 T.

In **Fig. 22**, it presents the RCP against the external magnetic field for the compound $TbCu_2Si_2$ at varying magnetic fields from 1.0 T, 1.5T and 2.0 T. It is observed that RCP grows in a monotonic way upon a rising level of magnetic field, and it attains the value of 71.58 J/kg, for h= 2.0 T.

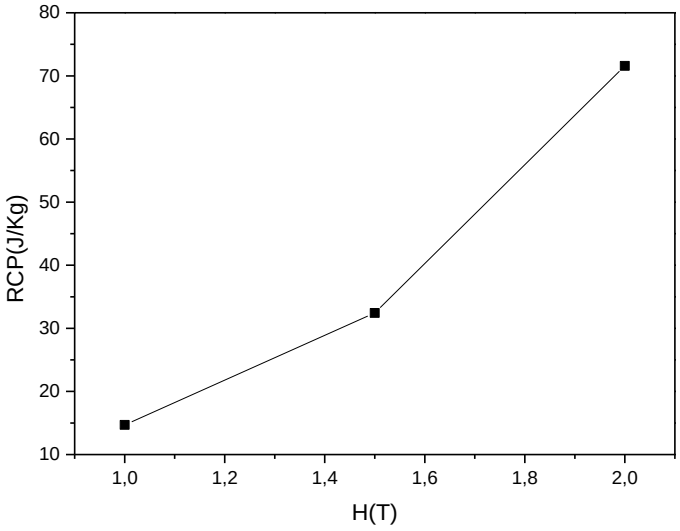

Figure 22: Field dependence of the RCP of TbCu2Si2 compound as a function of the external magnetic field

Conclusion:

The structural, electronic, magnetic and magnetocaloric properties of the intermetallic material $TbCu_2Si_2$ were examined through several methods including: first principle calculations and MC. As a result of Ab-initio calculations, the magnetic moment and exchange coupling interaction are determined as $5.93\mu_B$ and J_1=0.58 meV, J_2=-0.69 meV and J_3= 0.41 meV, respectively. The resulting T_N agrees well with experimental findings. Near T_N, significant MCE value was found, where the max value of ΔS_M^{Max} and RCP are 40.78 J/Kg.K, 71.58 J/kg, respectively, under applied an external magnetic field of h=2.0 T. Their good magnetocaloric properties imply usability of $TbCu_2Si_2$ for the application in magnetic refrigeration.

CHAPTER 4
Magnetic, magnetocaloric and transport properties of the intermetallic LaMn2Si2 compound: A theoretical study

Introduction:

The manipulation of thermoelectric cooling technology has driven significant research activity [79,80], with the goal of converting electricity into cooling or enabling heat pumping through the Peltier effect [81,82]. Thermoelectric coolers (TECs) are repeatedly described as a cooling technology employing thermoelectric modules (TEMs), benefiting several advantages of a noiseless, friendly environment and faster reaction contrary to the compression refrigeration process work with a mechanical motion under the Peltier effect producing nosily cooling equipment [83,84] Over the past years, the huge most research has concentrated on compounds that are auspicious for power generation at medium and high temperatures. Although several material like $YbAl_3$, $Cu_{0.9}Ni_{0.1}AgSe$, $Bi_2Te_{3-x}Se_x$, $Mg_3Bi_{1.25}Sb_{0.75}$, $Bi_{0.905}Sb_{0.095}$, $Bi_{2-x}Sb_xTe_3$, $CePd_{2.95}$, Ce $(Ni_{0.6}Cu_{0.4})_2Al_3$ have emerged which may enrich material for thermoelectric [85]. Together with other related compounds, the family of RMn_2Si_2 material looks very beneficial for research of high-temperature thermoelectric [114-120]. Therefore, Ternary rare earth manganese silicides was synthesized by solid-state reaction methods and arc-melting methods. The crystal structure of RMn_2Si_2 compound was formed by layers of R atoms (R=rare earth) sandwiched by boundless layers of intertwined tetragonal $SiMn_4$ pyramids lateral to (001). Adopting a stoichiometric material, Mn atoms are tetrahedrally adjoining by four Si neighbors thus being tetragonal pyramidally coordinated [121]. Recently, the ternary intermetallic compounds of the RMn_2Si_2 series (R= rare earth, T= transition metal, X= Si or Ge) has had a lot of success in the area of refrigeration, due to the many interesting phenomena that characterize them such as superconductivity, magnetism, mixed valence, heavy fermions and kondo behavior[122]. Previously, research in $LaMn_2Si_2$ found a simple ferromagnet with T_c =306K [123]. Nonetheless, there have been no theoretical reports on the magnetic, thermoelectric and magnetocaloric effects in these alloys to date.

The present chapter intends to explore the magnetic, thermoelectric and magnetocaloric properties of the intermetallic compound $LaMn_2Si_2$, through a combination of Ab-initio calculation and MC. The magnetic properties of the intermetallic compound $LaMn_2Si_2$ were characterized by a second-order transition of FM state to the PM state near $T_C \sim 319K$, while a giant magnetocaloric effect was observed under the application of a magnetic field of h=7.0T. The maximum values of ΔS_M and RCP are $3.34\,J/Kg.K$ and $127.3\,J/K$ for $h = 7.0\,T$, which is about one third of the Gd at 295 K for 5T [113]. Benefiting from non-toxicity, low price, and low density we can suggest this material as a good candidate for magnetic refrigeration applications around the room temperature.

4.1- Structural properties of the intermetallic $LaMn_2Si_2$ compound:

The $LaMn_2Si_2$ intermetallic materials are characterized by a tetragonal crystalline structure similar to the compound $TbCu_2Si_2$, see **Fig. 23.** The computed lattice and atom position parameters are presented below in Table 4. It is apparent that the achieved result agrees well within experimental parameters [123].

	Lattice constant			$d_{Mn\text{-}Si}$(Å)	$d_{Mn\text{-}Mn}$(Å)	$d_{Mn\text{-}La}$(Å)
	a(Å)=b(Å)	c(Å)	z(Si)			
Present work [113]	3.9904	10.382	0.3798	2.4117	2.8216	3.2737
Experimental values [123]	4.1283	10.6632	0.3805	2.4894	2.9191	3.3715

Table 4: Structural parameters of the intermetallic LaMn2Si2 compound

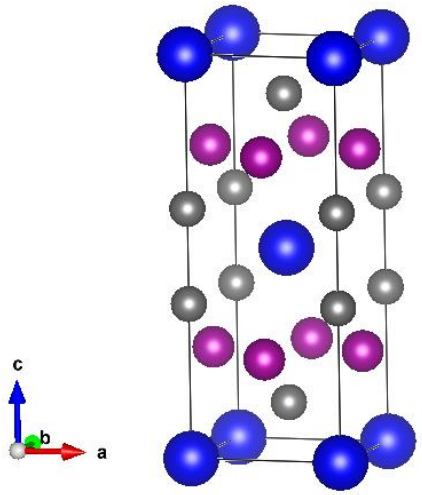

Figure 23: Structure of LaMn2Si2. La, Mn, and Si atoms are situated in blue, magenta, and dark gray, respectively.

4.2- Electronic and magnetic properties of the intermetallic $LaMn_2Si_2$ compound:

The total and partial densities of states for the intermetallic material $LaMn_2Si_2$ are represented in **Fig. 24**. Based on the below figure, it was found a metallic behavior is present for this compound. The largest contribution in total DOS is provided by the Mn atom, whereas the atoms of La and Si are weak contributors in DOS, the hybridisation effect between the states Mn-Si and Mn-La was investigated. The Mn (d) and Si (p) states hybridize mostly near the energy range of -5 eV to -2.0 eV. There exist two probable type of interlayer interaction, which are the super-exchange interaction between Mn-Si-Si-Mn and the Mn-La-Mn.

The band structure of the intermetallic compound $LaMn_2Si_2$ presented along the high symmetry directions **Γ**, **H**, **N**, **Γ**, **P** of the Brillouin zone is shown in **Fig. 25** [124,125].This shows that there is no energy gap in the Fermi level, indicating a metallic attitude of this compound; the SD states are more closely spaced than the SU states at the Fermi level. The band structure of this compound originates mostly from *d* orbitals of Mn atom, containing a low weight of d_{z2} and d_{yz} is associated with the collinear FM phase unstable state of $LaMn_2Si_2$ at 0.0 K.

Also, the following values of the magnetic moment for the atoms of Mn, La and Si were found 2.23μ_B, 0.003μ_B, and -0.007μ_B. The obtained Mn magnetic moment (μ_{eff}=2.23μ_B) matches very well to the experimental value (μ_{eff} = 2.49μ_B) [113].

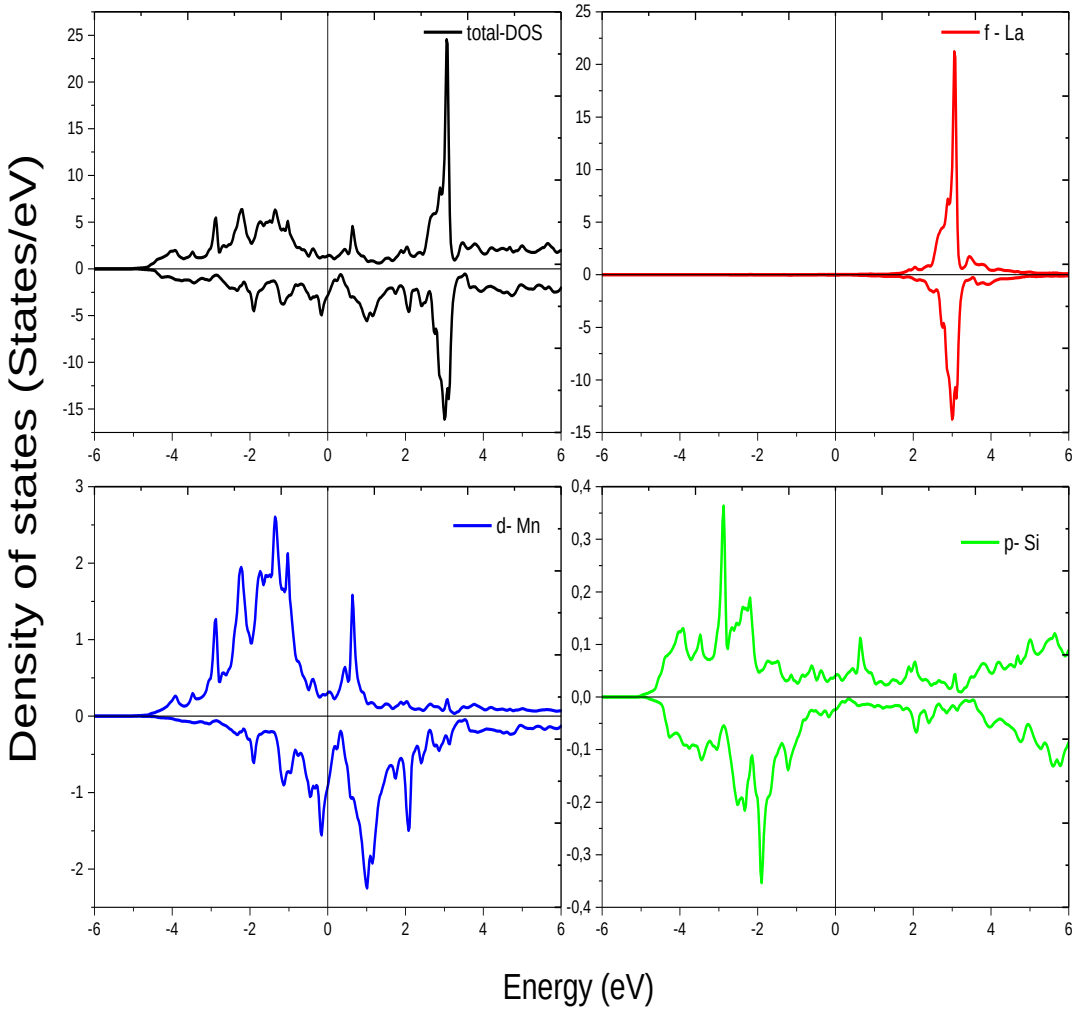

Figure 24: Total and partial densities of states for the intermetallic LaMn2Si2 compound

(a)

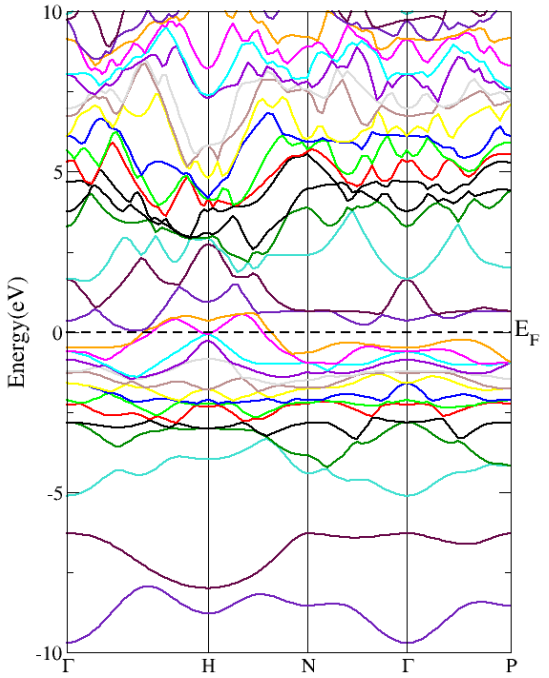

(b)

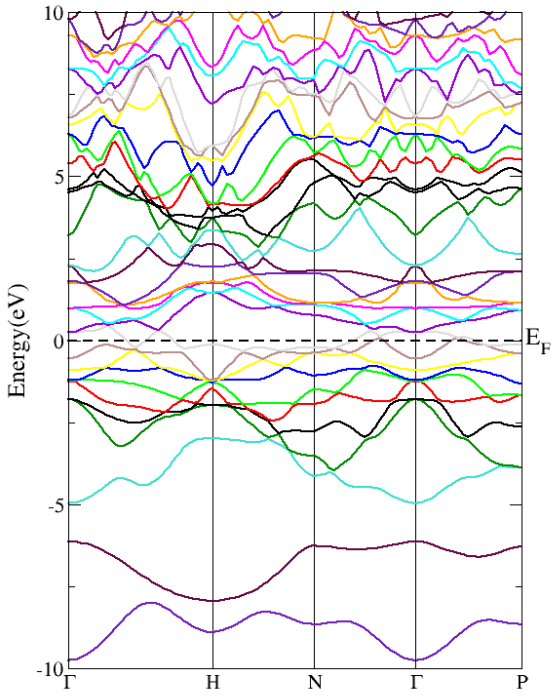

Figure 25: Band structures of LaMn2Si2 compound with GGA approximation. (a) SU and (b) SD.

4.3- Magnetic ground states:

It was found that the quadrupole frequency undergoes a drastic change close to the T_C, associated with a strong reorientation of the spin in relation to the axis crystalline. Since, at low temperatures, these compounds have a NC magnetic structure with the magnetic moments of Mn, ordered in a conical spiral along the c-axis. In the RMn_2X_2 series, it was described that the distance interatomic Mn-Mn, that is, d_{Mn-Mn}, defines whether the compound has a state AFM or FM. For distances greater than $d_{Mn-Mn} > 2.85Å$ will a FM interplanar interaction occurs, but if $d_{Mn-Mn} < 2.85Å$ will lead to AFM interplanar interactions between Mn atoms.

In the first time, we do a comparison between FM states and 3 types of AFM configurations. As can be seen from table 5 the energy of AFM is more stable than FM configuration which approve the hypothesis discuss above.

	Total energy (Ry)
AFM1	-45580.57049802
AFM2	-45580.56680745
AFM3	-45580.57243515
FM	-45580.56189074

Table 5: Magnetic configurations and total energy of each magnetic configuration.

Secondly, we do systematic studies between collinear and noncollinear (see **Fig.26**) we found the NCM more stable than the AFM3 (see **Fig.27**).

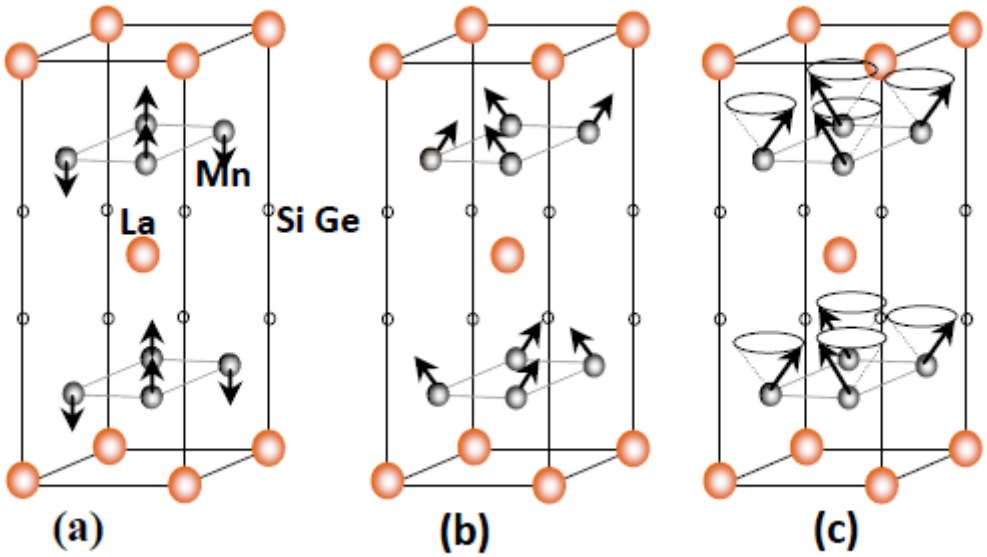

Figure 26: different magnetic structure of the intermetallic LaMn2Si2

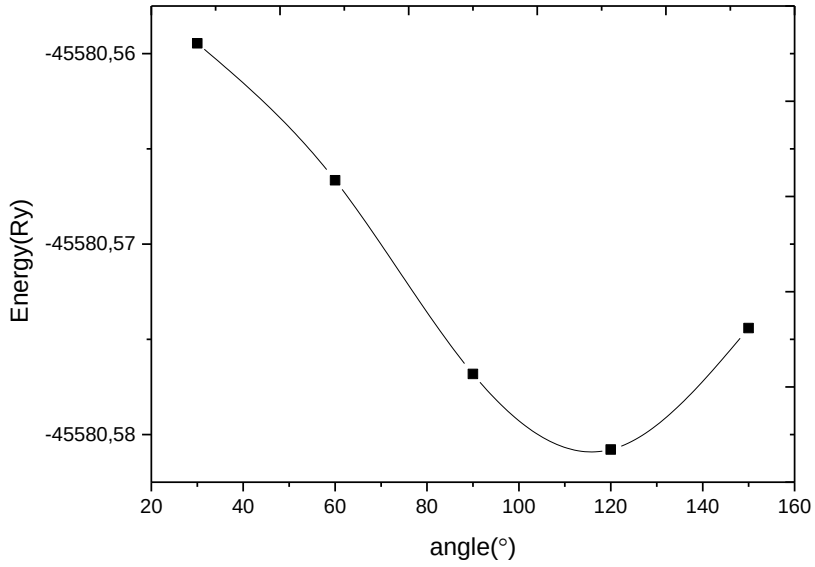

Figure 27: angle dependence of the Energy of the intermetallic LaMn2Si2

4.4- Theory and Model:

The magnetic and magnetocaloric properties of the intermetallic $LaMn_2Si_2$ compound with the effect of temperature are calculated using MC. Contrary to the material treated in the

previous chapter, the material $LaMn_2Si_2$ is stable in the NC state. This requires choosing the Heisenberg model.

In the simulation process, we use the Hamiltonian expressed by [126]:

$$H=\mathcal{H}_{mag} + \mathcal{H}_{AM} + \mathcal{H}_{ext} \tag{4.1}$$

First term is the magnetic Hamiltonian, defined as the following:

$$\mathcal{H}_{mag} = -J_1 \sum_{<i,j>} \overrightarrow{S_i S_j} - J_2 \sum_{<i,k>} \overrightarrow{S_i S_k} \tag{4.2}$$

J_1 and J_2 are the first nearest Mn-Mn neighbour's in-plane and second nearest Mn-Mn neighbour's between planes, respectively, have been studied by using Ab-initio methods of calculation according to the following equation Eq. (4.3) [127]:

$$J_i = \frac{\Delta E_i}{z_i N J S^2 (1-\cos(\theta))} \tag{4.3}$$

where z_i $(i = 1 \text{ and } 2)$ is the number of neighbors, N is the number of magnetic atoms per unit cell. ΔE_i was the difference in the energy value and it was determined from magnetic orientations in which manganese (Mn) atoms rotate by an angle θ from the z axis. These magnetic configurations have been chosen to keep all spatial group symmetry. $\boldsymbol{S}_i$ is a three-dimensional unit vector representing the orientation of the spin of the ^{i}th Mn atom, and <*i*,*j*> refers to nearest neighbor Mn atom pairs $\vec{S}_i = (S_x, S_y, S_z)$.

Where $\vec{S}_i$ is expressed in the spherical presentation as (see **Fig.55**):

$$S_x = \sin\theta \cos\varphi$$

$$S_x = \sin\theta \sin\varphi$$

$$S_z = \cos\theta$$

Where: θ and φ are the angle with the z axis and the polar angle in the xy plane, respectively.

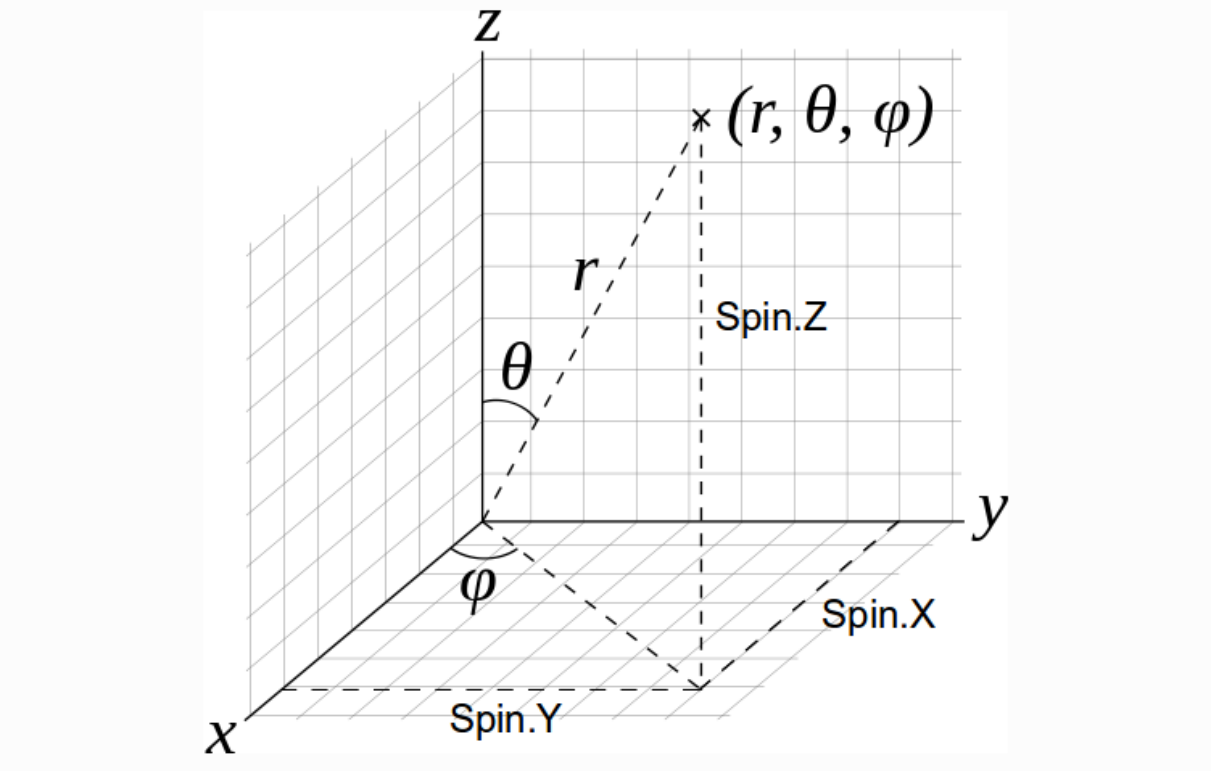

Figure 28: Schema of the spherical presentation of the Spin in the Heisenberg model

On the second terms in the equation (4.1) there is the anisotropic term, which is represented as follows:

$$H_{AM} = -\Delta \sum_i (S_i^z)^2 \tag{4.4}$$

In this case, Δ is the uniaxial anisotropy of single ion, being equal of the energy gap between the lowest and the highest energy position.

The energies of the anisotropy were computed through the program DIPAN that has been imported into WIEN2K. Results are reported in **Table 6**. The easy axis in each case in the [110] and [010] orientations, whereas the hard axis was in the [001] orientation, as would be anticipated from tetragonal symmetry.

Direction			Energy (J/m^3)
X	Y	Z	
0	0	1	-0.4063768 10^{+5}

0	1	0	0.2031884 10^{+5}
1	0	0	0.2031884 10^{+5}
1	1	0	0.2031884 10^{+5}
1	1	1	-0.2673506 10^{+5}
0	1	1	-0.3279163 10^{+5}
1	0	1	-0.3279163 10^{+5}

Table 6: Energies for the different directions of LaMn2Si2

As the last parameter of equation (4.1), it is the external magnetic Hamiltonian:

$$H_{ext} = -\sum_{<i>} \vec{h}\vec{S}_i \quad (4.5)$$

In this equation, h represents the magnetic field for the z-axis.

In this chapter, we have performed the exchange coupling interactions (J_1, J_2) with the following values J_1=298.5meV and J_2=61.77 meV. The magnetic anisotropy (Δ) of the intermetallic $LaMn_2Si_2$ is equal to 7.4849×10^{-2} meV.

4.5- Result and discussion:

The magnetic and magnetocaloric properties of the $LaMn_2Si_2$ intermetallic material have been examined by means of the **MC**. Therefore, both the temperature dependence of magnetization and susceptibility are presented in **Fig. 29**. Our simulations reveal a notable peak in the susceptibility result near T_C=319K. Likewise, there is a maximum value of magnetization occurring along the z-direction, which matches with DFT calculation. Also, it is observed discontinuity near T_C, which is caused by the transitions from the **NC** phase to the AFM collinear phase. However, as observed in Table 7, the T_C determined by MC agrees well with experimental results [128].

Table 7: The comparison between the experimental critical temperature and that obtained by using the MC

	Experimental studies	MC simulations
T_C of $LaMn_2Si_2$ compound	**306 K [128]**	**319 K**

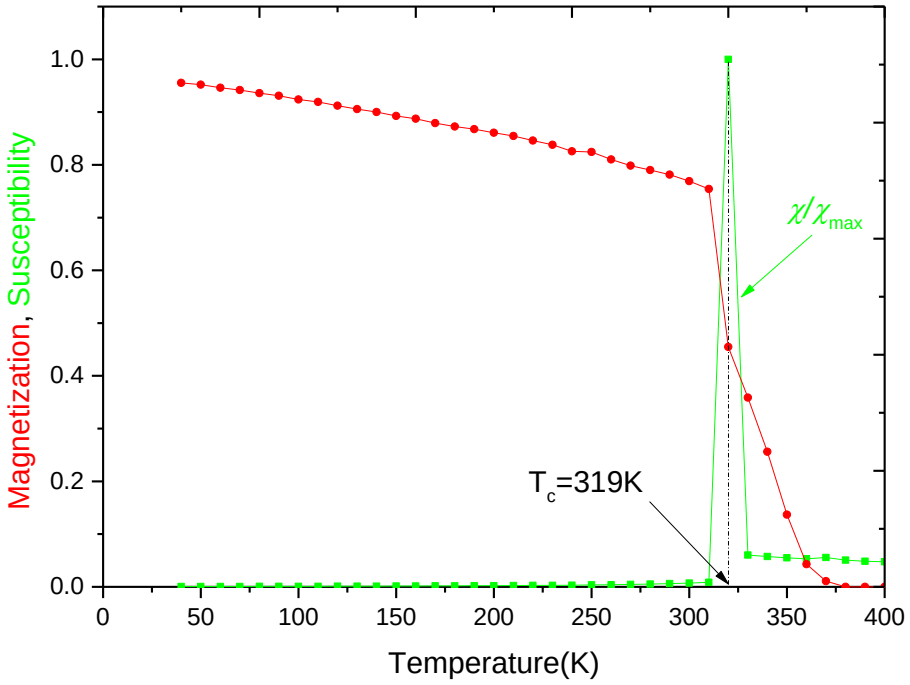

Figure 29: Temperature dependence of the magnetization and susceptibility of the intermetallic LaMn2Si2 compound at h=0.0T

From **Fig. 30**, the temperature dependence of (ΔS_M) at various h scales of 3.0 T to 5.0 T and 7.0 T are given. Thus, there is a noticeable variability seen in ΔSM of near T_C. This may occur in the FM materials as the result of magnetic moments arising from presence of h. As observed upon raising h as a result ΔS_M shifts to 3.34 J/kg. K at h=7.0T. Further to the entropy change a significant factor explaining the performance of a magnetocaloric material is its RCP. The measure of RCP defines the grade of magnetic material for MR applications. Also, it indicates the transfer of heat between the cold and hot sinks under an optimal refrigeration cycle. Figure 31 illustrates the RCP as a function of external magnetic field for

the $LaMn_2Si_2$ compound at different magnetic fields of 3.0 T, 5.0 T and 7.0 T. By increasing h the RCP may exhibit linear curve trend and attain the value of 127.3 J/kg, for h=7.0 T. Our results are similar with other works [129, 130]. The temperature transition was close to the room temperature. Both the maximum ΔSM and RCP values are 3.34 J/kg. K and 127.3J/kg at 7.0T see **Table 8**, it is observed to be approximately a third of Gd at 295 K for 5T. Moreover, our findings are better than those of the 3D-Ising model owing to the complex nature of the NC alloy. This suggests that Heisenberg's anisotropic model is the preferred model for studying this particular kind of alloy.

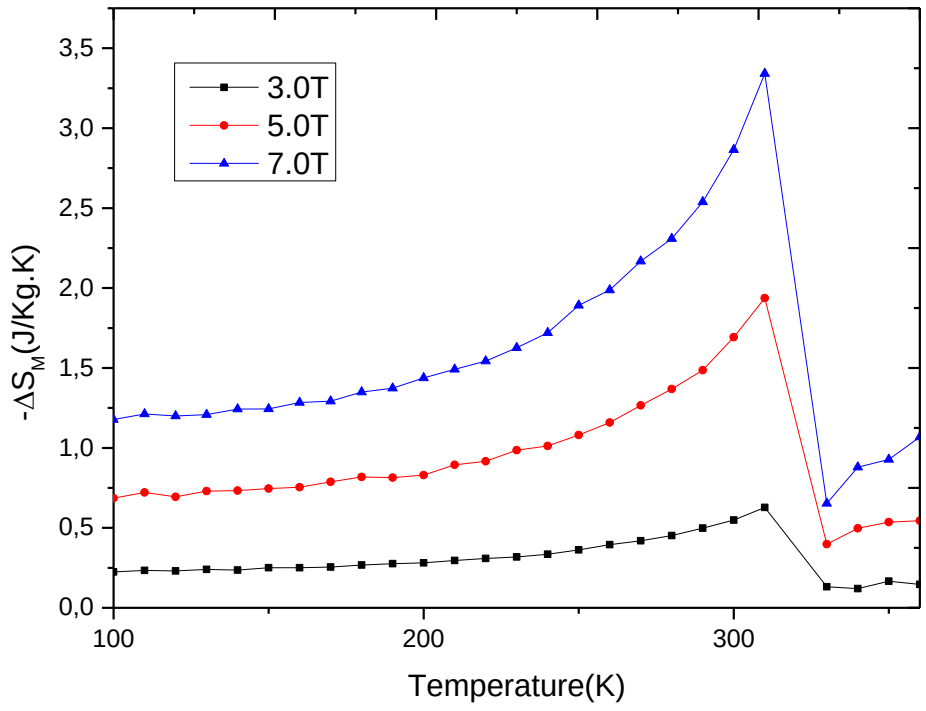

Figure 30:Magnetic entropy change as a function of external Magnetic fields: 3.0 T, 5.0 T, and 7.0 T

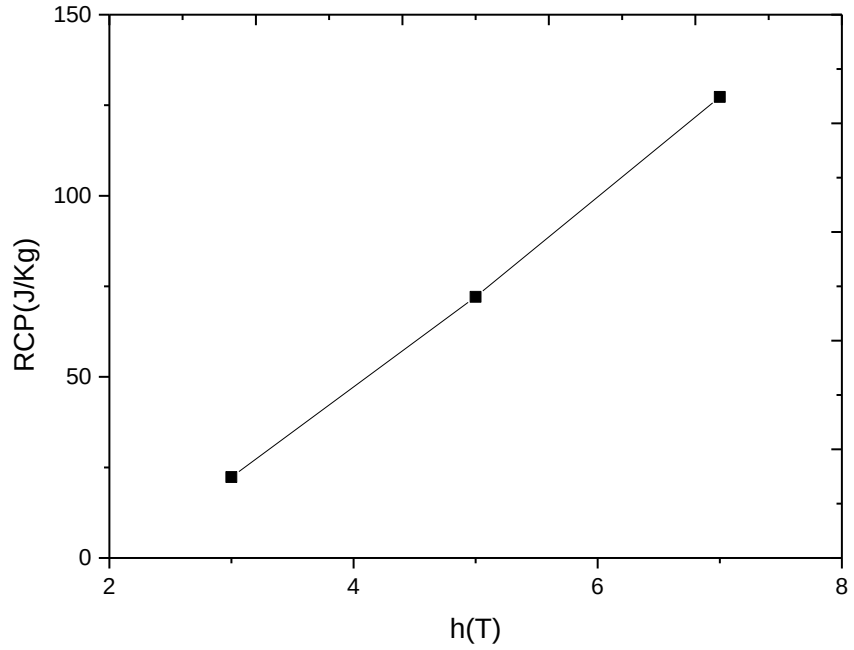

Figure 31: RCP change as a function of the external Magnetic fields: 3.0 T, 5.0 T, and 7.0 T.

	h(T)	T_C(K)	ΔS_M (J/kg.K)	RCP(J/K)	Reference
Gd	5	295	10.2	410	[129]
3D-Ising model	6	311	1.1	82	[130]
Experimental studies	7	306	3.46	154	[123,128]
Present work	7	319	3.34	127.3	This work[113]

Table 8: Comparison between the experimental magnetocaloric properties and those obtained 3D-Ising model and our simulations.

4.6- Boltzmann's transport theory:

The simulated electrical conductivity and Seebeck coefficient calculations may be accomplished with the help of first principles calculations and the Boltzmann transport equation. The most popular simulation software available today is the code BoltzTrap [108].

Additionally, it was first written to employ the energy of the WIEN2k, VASP, and Quantum Espresso codes [109]. The transport of charge arises when there is an electrical field and/or a thermal gradient. This phenomenon may be characterized as follows [110]:

$$J = e\sum f \cdot \boldsymbol{v} = \boldsymbol{\sigma E} \tag{4.6}$$

Where J is the charge flux, e is the electronic charge, f is the charge distribution, σ is the electrical conductivity, E is the electric field and v is the charge velocity. Once the distribution of charge over time and space has been identified, it is possible to identify the flux of charge. The distribution of charge concerning time is illustrated by the following [111]:

$$\frac{\partial f}{\partial t} + \frac{dr}{dt} \cdot \nabla_r f + \frac{dp}{dt} \cdot \nabla_p f = \left(\frac{\partial f}{\partial t}\right)_c \tag{4.7}$$

where r is the position of the electrons; p is the momentum and c, index signifying the collision. The variation of the charge distribution after a collision is illustrated in Equation (4.7).

$$\frac{\partial f}{\partial t} = \frac{f - f_0}{\tau} \tag{4.8}$$

$$f - f_0 = Ce^{-\frac{t}{\tau}} \tag{4.9}$$

From the above mentioned Equations (4.7- 4.9), we extract the following:

$$f = f_0 + e\left(-\frac{\partial f_0}{\partial \varepsilon}\right)\tau v \cdot E \tag{4.10}$$

The conductivity can be expressed by replacing (4.6) in equation (4.10) with the following:

$$\sigma = e^2 \sum \left(-\frac{\partial f_0}{\partial \varepsilon}\right) v^2 \tau \tag{4.11}$$

In the framework of the electronic structure calculations, the following equation can be expressed as a tensor:

$$\sigma(\varepsilon) = \frac{e^2}{N\Omega} \int d\varepsilon \left(-\frac{\partial f_0}{\partial \varepsilon}\right) \sum_{n,k} \tau_{n,k} \vec{v}_{n,k} \vec{v}_{n,k} \delta(\varepsilon - \varepsilon_{n,k}) \tag{4.12}$$

where Ω is the volume of the unit cell, e is the carrier charge, ε is the energy of the group, N is the number of k-points used in the calculation, f_0 is the distribution function Fermi-Dirac distribution function, τ is the relaxation time, ν is the charge group velocity and δ is the delta function [112]. The indices k and n are the crystal momentum and the band index. The velocity ν can be estimated from the band structure with the following relationship:

$$\vec{v}_{n,k} = \frac{1}{\hbar} \frac{\partial \varepsilon_{n,k}}{\partial k} \quad 4.13$$

where ħ is the reduced Planck constant.

In the presence of a temperature difference, the total electric field differs from the Equation (4.6) owing to a field resulting from Seebeck effect. Therefore, the equation (4.6) is now given by the following equation:

$$J = \sigma E - \sigma S \nabla T \quad 4.14$$

And the heat flux (q) that is generated from the difference of the temperature can be characterized as following:

$$J = TJ_S = STJ - \kappa \nabla T \quad 4.15$$

where Js is the entropic flux. Equations (4.14) and (4.15) are called the Onsager [112]. By using the Onsager equations we can obtain the Seebeck coefficient and the electronic thermal conductivity (ke) obtained from Seebeck coefficient and the electronic thermal conductivity (ke) obtained from the calculation of the band structure.

$$S = \frac{eK_B}{N\Omega} \sigma^{-1} \int d\varepsilon \left(\frac{\partial f_0}{\partial \varepsilon}\right) \left(\frac{\varepsilon - \mu}{K_B T}\right) \sum_{n,k} \tau_{n,k} \vec{v}_{n,k} \vec{v}_{n,k} \delta(\varepsilon - \varepsilon_{n,k}) \quad 4.16$$

$$\kappa_e = \frac{K_B^2 T}{N\Omega} \int d\varepsilon \left(-\frac{\partial f_0}{\partial \varepsilon}\right) \left(\frac{\varepsilon - \mu}{K_B T}\right)^2 \sum_{n,k} \tau_{n,k} \vec{v}_{n,k} \vec{v}_{n,k} \delta(\varepsilon - \varepsilon_{n,k}) - T\sigma S^2 \quad 4.17$$

where μ is the chemical potential, and KB the Boltzmann constant.

From the above equations, we can identify the electrical conductivity, the Seebeck coefficient and the electronic thermal conductivity. Only one parameter we do not know yet is the relaxation time value. If we assume that it varies slightly over the energy area considered, that

it remains unchanged, the Seebeck coefficient can be derived from the band structure without using the fitting parameter because the relaxation time constant in the numerator and denominator will disappear. The relaxation time is a function of the band energy in the real materials. Most codes for calculating electric transport properties like BoltzTraP and BoltzWann assess these properties using the constant relaxation time approximation.

4.7- Transport properties of the intermetallic $LaMn_2Si_2$ compound:

The BoltzTraP code [131] with semi-classical Boltzmann theory is employed to compute the transport properties. As observed in Fig. 33, the thermal conductivity grows with increasing temperature and attains the highest value of 6.2×1014 W.m- 1 K-1.s-1at approximately the Curie temperature. Inversely, the electrical conductivity diminishes straight with temperature from .33×1019Ω-1.m-1.s-1 at 50K to 7.51×1019Ω-1.m-1.s-1 at 400K, respectively. It is worth noting that the electrical and thermal conductivity profile makes LaMn2Si2 an adequate material selection for the thermomagnetic generator application. Also, the Seebeck coefficient S (T) as shown, the values of S (T) were revealed as positive, indicating that holes are the dominant carrier in this zone.

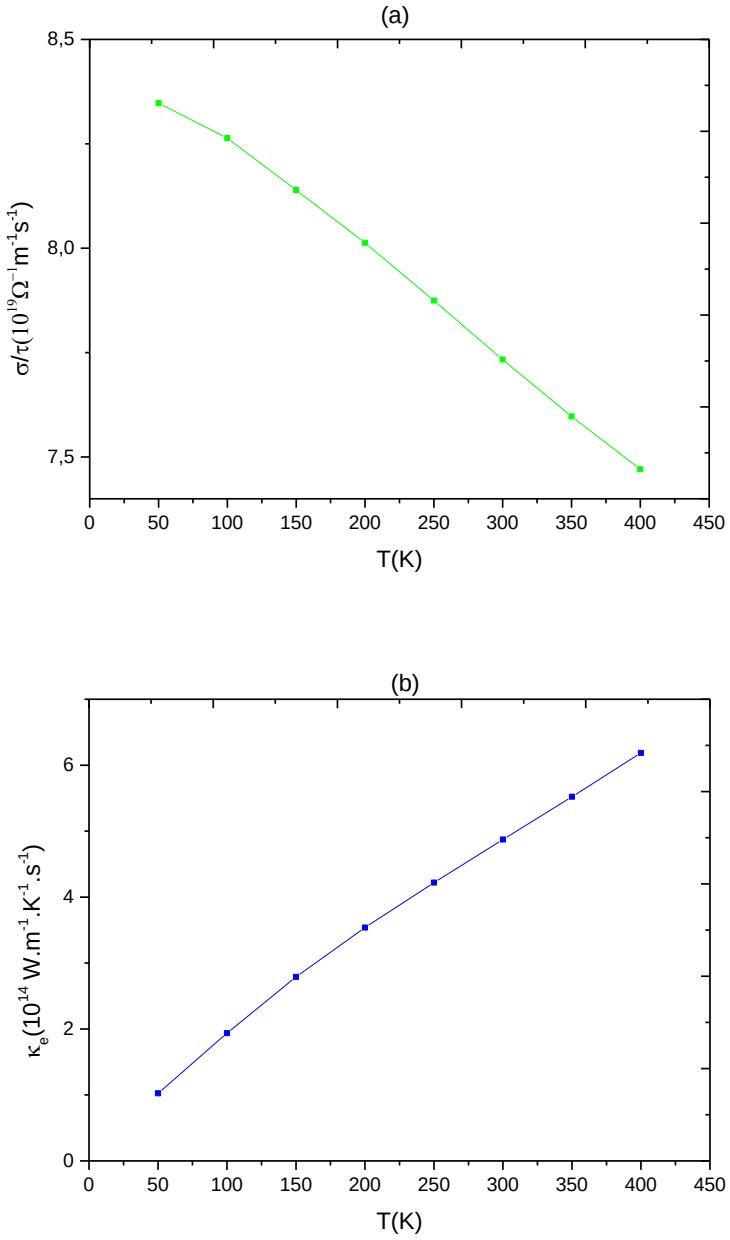

Figure 32:Temperature dependence of: (a) the Electrical and (b) the thermal conductivity of the intermetallic LaMn2Si2 compound.

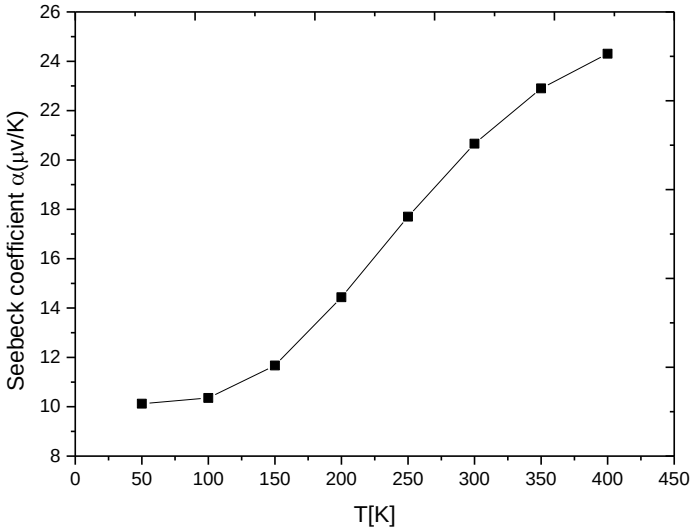

Figure 33: Temperature dependence of Seebeck coefficient of the intermetallic LaMn2Si2 compound.

Conclusions:

This chapter presents the magnetic, magnetocaloric and transport properties of the $LaMn_2Si_2$ intermetallic material by means of several theory approaches including first principle calculations and MC. The exchange coupling interactions and anisotropy values are found to be (J_1=298.35meV, J_2=61.77 meV) and $\Delta = 7.4849\times10^{-2}$ meV from ab-initio calculations. These T_C obtained from the MC are in close conformity with those obtained experimentally. Near T_C, significant magnetocaloric effect has been found, and the maximal value of ΔS_M and RCP are 3.34 J/Kg.K, and 127.3J/kg, respectively, under an external magnetic field h=7.0 T. The interlayer composite $LaMn_2Si_2$ exhibits large magnetocaloric effect, which might be employed in future cooling devices owing to the high MAE. By computing the electrical and thermal conductivity, we have identified this material as an appropriate selection for a thermomagnetic generator.

CHAPTER 5
Strain effect on physical properties of the multiferroic Mn3Sn material: A first-principles calculations

Introduction:

The interest in multiferroic materials has been outstanding for their applicability in electronic devices including actuators, magnetic sensors, tunneling devices, magnetic/FE data storage media, spin-based devices (spintronics), magnetocapacitive devices, nonvolatile memories, random access memories, and novel memory devices. The research conducted into intermetallic materials for their remarkable applications in various areas that include optoelectronics, magnetics, spintronics, and thermoelectrics. [132-136]. Hence, the Mn_3Z (Z=Ga, Ge, and Sn) compounds have been the main attraction owing to several useful features which have never been observed in the zero-field AFM, including the MOKE and the ambient temperature piezoelectric phenomenon. [137-138]. Furthermore, they can be controlled with a magnetic field and can therefore be used for developing AFM spintronics and energy collection technologies [149, 140]. In like manner, the most outstanding of them is the topological AFM Mn_3Z (Z = Ge, Sn), showing large AHE, ANE, large MOKE, TAHE, PHE, THE, and many other abundant and excellent features [141]. The reason for those exceptional characteristics is mainly the non-collinear AFM structure. The Mn_3Sn multiferroic material has a hexagonal AFM structure, with the multilayered MnSn-MnSn. Over $T < T_N \sim 430K$, the combination of AFM and DMI results in the inverse triangular spin structure, precisely, a 120° spin structure with the planar Mn moments having an uniform negative vector chirality as a result of the geometrical frustration [142-145].

The origin of the rivalry of the following interactions especially, the HES, DMI, and MAE should be provided from the non-collinear AFM arrangement [146]. Since the discovery made by Higo et al [147] about a large MOKE, they have found that the noncollinear AFM alloy Mn_3Sn [148], has a large zero-field Kerr rotation angle of about 20 degrees under room temperature, which is comparable with the FM metals. Other authors such as Nyari et al. [149], have studied the weak ferromagnetism in the Mn_3Z (Z =Sn, Ge, and Ga) based on the

application of ab-initio calculations and spin models. They have numerically confirmed the results of Chen et al [150], and additionally studied the noncollinear AFM hexagonal compound Mn_3Ge and Mn_3Sn by considering various planar and non-planar trilateral magnetic arrangements. Furthermore, for this particular case, there were a number of spin-compensated configurations that were expected to disclose an AHE. The non-collinear AFM in the compound Mn_3XN (X = Ga, Zn, Ag, and Ni) is newly discovered to have strong AHE as well as MOKE by means of density functional calculations in conjunction with group theory analysis and tight-binding modeling [151]. Nowadays, the above anticipation were experimentally validated in both Mn_3Sn [152] and Mn_3Ge [153, 154].

This chapter focuses on implementing NCM to explore the effect of the DMI by introducing a strain effect in a thin film for FiM hexagonal Mn_3Sn. Also, the results on the impact of NC magnetism over the evolution of the MOKE are presented

5.1- Structural properties of the intermetallic Mn_3Sn compound:

The material Mn_3Sn solidify into the hexagonal form Ni_3Sn (see **Fig. 32 (a)**) in the subsequent space group (P63/mmc) under lattice properties such as a=5.6650 Å and c=4.5310 Å. The atoms for the Mn and Sn are situated in [0.8392, 0.6784, 0.2500], and $\left[\frac{2}{3},\frac{1}{3},\frac{2}{4}\right]$, respectively.

After that, the parameter used in the calculation is listed in **Table 9**, as can be observed, by raising or lowering the value of the strained parameter, then the volume grows or diminishes. This finding supports the validity of the strain-based procedure. As well, the Mn_3Sn thin film layer lattices in AFM states undergo the above mentioned biaxial strains. Both parameters a and c are depending upon the tensile or compressive percentage within the [-2%, 2%] area. The z- and x-axis metrics are obtained according to the formula below:

$$\varepsilon_{zz} = \frac{c-c_0}{c_0} * 100 \quad (5.1)$$

$$\varepsilon_{xx} = \frac{a+a_0}{a_0} \times 100 \quad (5.2)$$

Where c_0 and a_0 are the optimized lattice parameter of the unstrained system, c and a are the out-of-plane and in-the-plane lattice parameter under ε_{zz} and ε_{xx}.

Also, the surface of the thin film with a thickness of 0.9 nm was displayed in 2×1 (001) slices from the pristine model structure. A 20 Å thickness of vacuum slab along the [001] orientation has been included for each model. The gap layer was sufficiently deep to suppress a periodic boundary condition impact on the [001] direction. For additional information about the geometry of a Mn_3Sn trigonal film, refer to **Fig 29(b)**.

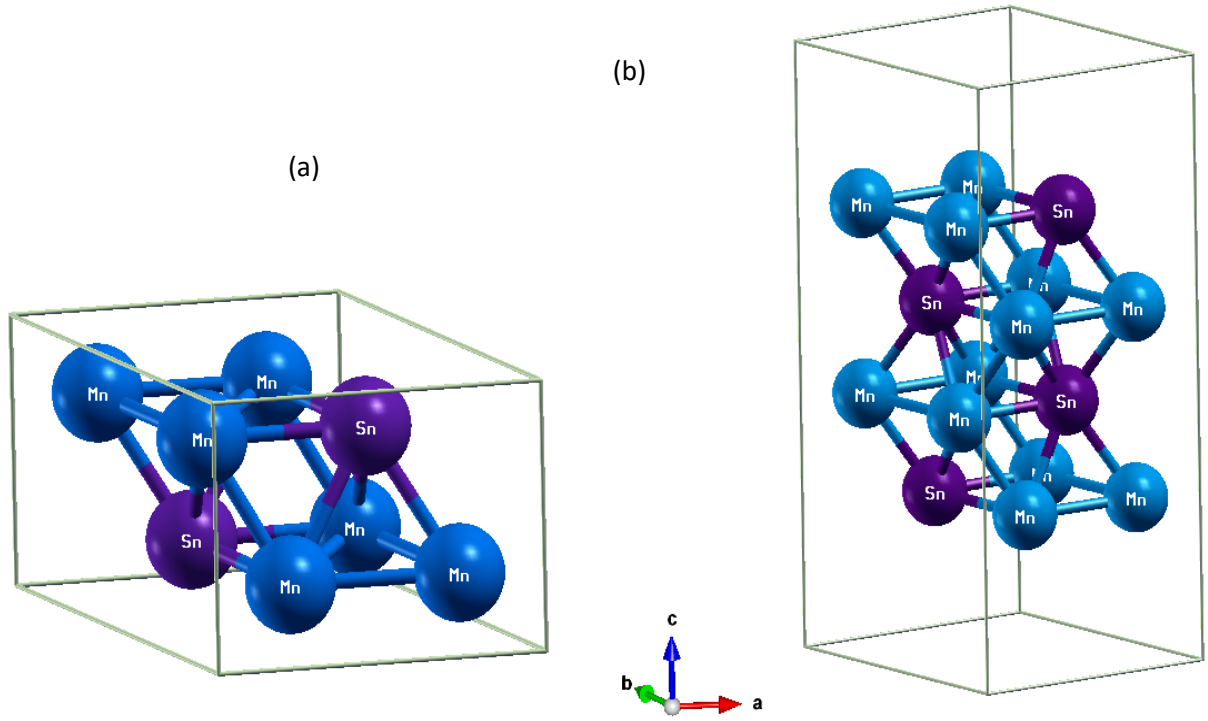

Figure 34:(a) Unit cell structure of Mn3Sn. (b) Side view of the Mn3Sn (001) thin films.

Strain (%)		Parameter a (Å)	Parameter c (Å)	V(Å)^3
0		5.6650	4.5310	145.4098
Tensile	+2.0	5.7783	4.4430	148.2560
	+1.5	5.7499	4.4630	147.5528
	+1.0	5.7216	4.4856	146.8437
	+0.5	5.6933	4.5083	146.1305
Compressive	-0.5	5.6366	4.5536	144.6736
	-1.0	5.6083	4.5763	143.9384
	-1.5	5.5800	4.5989	143.1931
	-2.0	5.5517	4.6216	142.4440

Table 9: Strain effect dependent lattice parameter of antiferromagnetic Mn3Sn compound.

5.2- Electronic and magnetic properties of the intermetallic Mn_3Sn compound:

We now proceed to analyze specifically the electronic structures for the intermetallic Mn_3Sn. **Fig. 33** depicts both the total and partial DOS for AFM structure. The metallic character of the Mn_3Sn is visible. Also the major part of the contribution in the total DOS is primarily coming from Mn-3d orbital. As is apparent from the **Fig.34** and **Fig.35**, both compression & tensile distortion have a slight influence on the DOS.

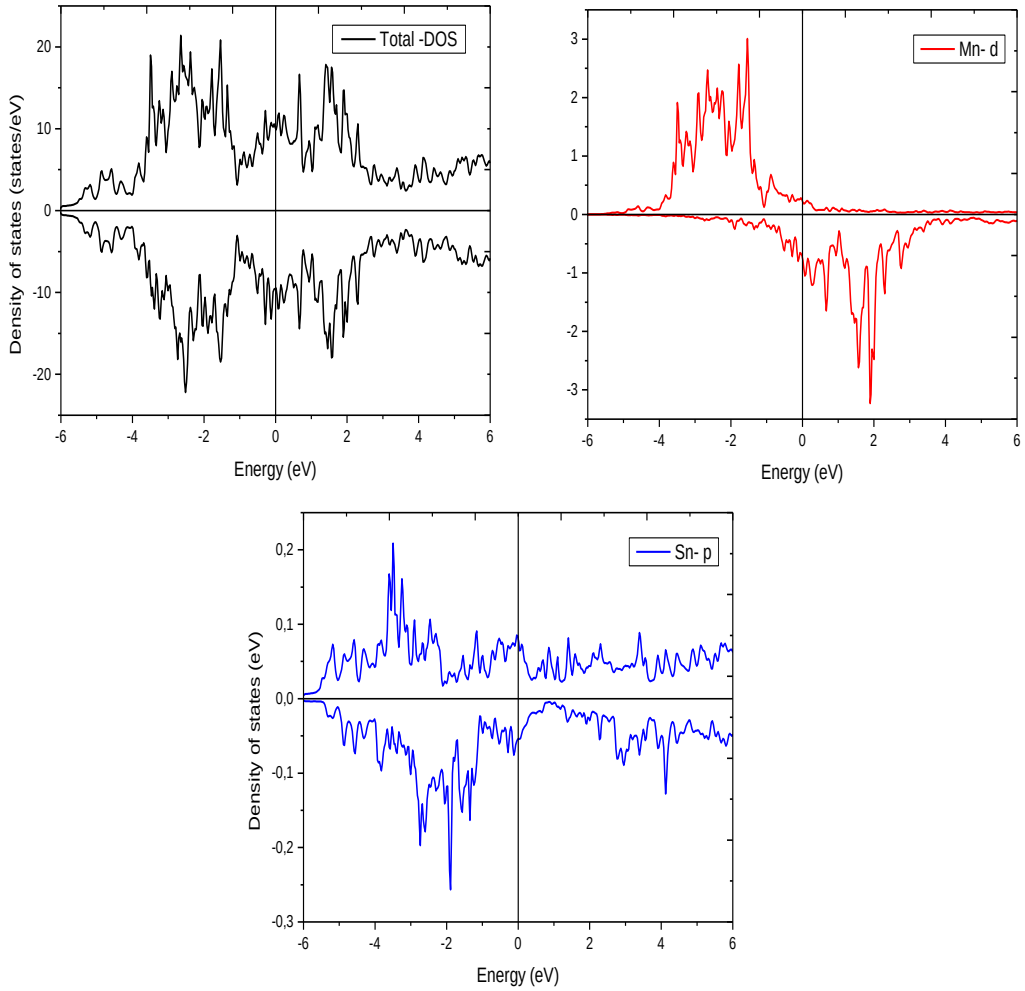

Figure 35: The total and partial DOS for the Mn3Sn compound

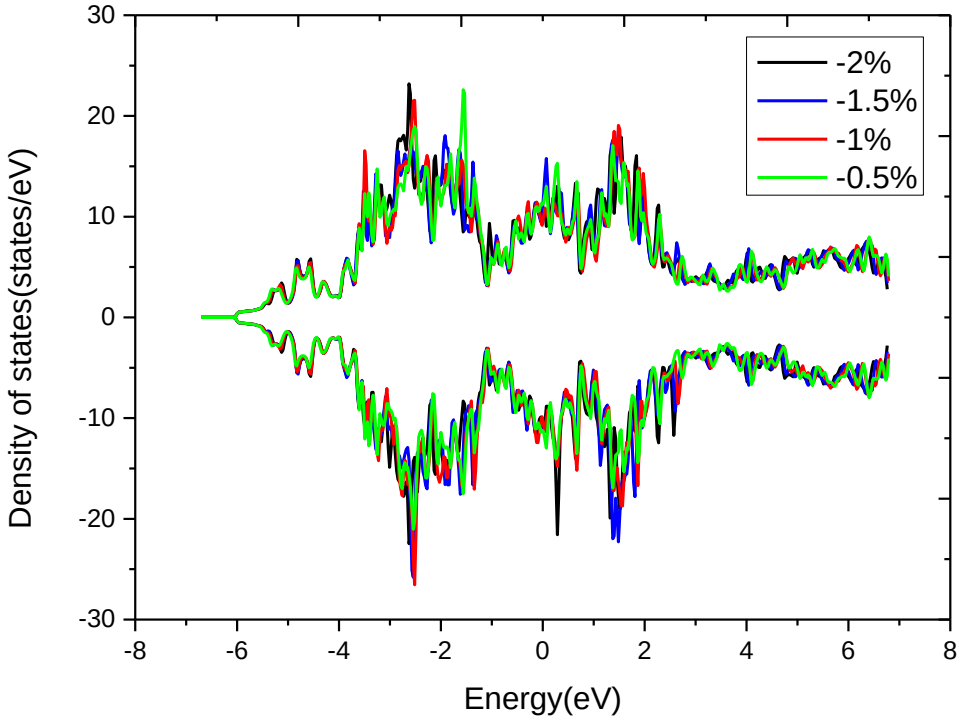

Figure 36: Effect of the compressive strain on the total for the Mn3Sn compound

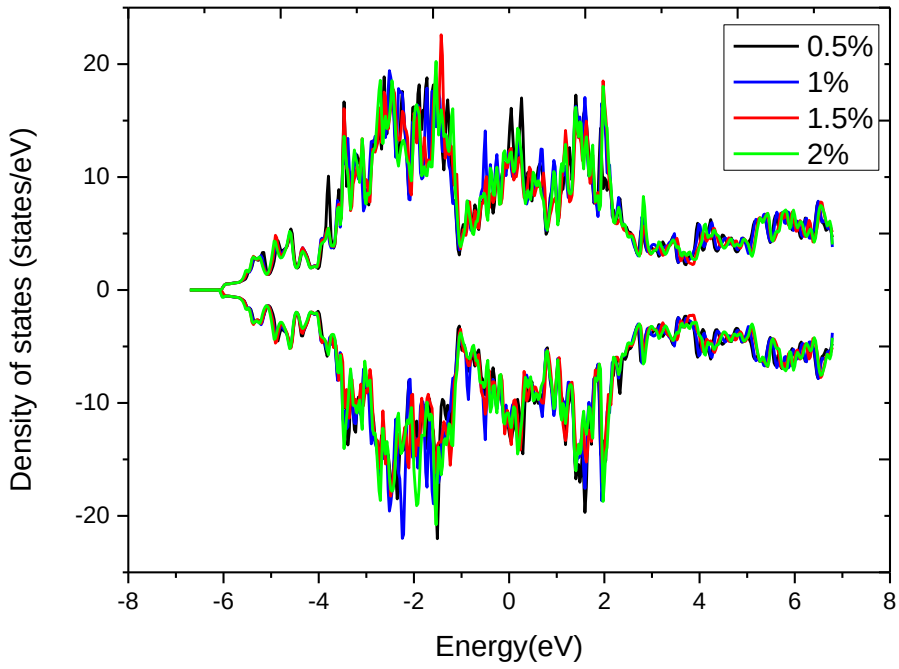

Figure 37: Effect of the tensile strain on the total for the Mn3Sn compound

The values of the magnetic moment μ_{Mn}^{tot} computed for the various manners are tabulated in **Fig. 36**. The compression of lattice parameter leads to increment in the magnetic moment of the Mn in the opposite of expansion that reduces the moment. The resulting value of the magnetic moment is in close accordance with previous research [156].

5.3- Dzyaloshinskii–Moriya interactions (DMI):

In addition to the magnetic interactions previously mentioned, another one appears only in systems of weak symmetries. The DMI allows chirality. Whereas the exchange interaction will only depend on a function of the absolute value of the angle between neighboring spins, the DMI favors a singular spin rotation direction. The above interaction originated in the fifties to describe the magnetization in exotic materials, for example, for α-Fe2O3 [156]. The basis of this argument is based on crystal symmetries. Thus, we can write the interaction according to the following formula:

$$E_{\mathrm{DM}} = \mathbf{D} \cdot (\mathbf{S_1} \times \mathbf{S}_2) \tag{5.3}$$

Where D represents a vector describing the DMI and S_i gives the orientation of the neighbor spins. Then Moriya theorized the interaction [156] and gave the orientation of vector D in the function of the crystal lattice symmetries. This term is almost proportional to exchange interaction and corresponds to antisymmetric exchange coupling.

We initiated the discussions with the fundamental magnetic states. Three kinds of magnetic arrangements have been considered, a FM state, the frustrated AFM (see **Fig. 37**), and four AFM states. The frustrated AFM configurations prove to be the fundamental magnetic state having the lowest energy amongst other magnetic configurations. Moreover, the favorable magnetic structure attained is owed to the presence of electric DMI, see **Figs. 38** and **39**.

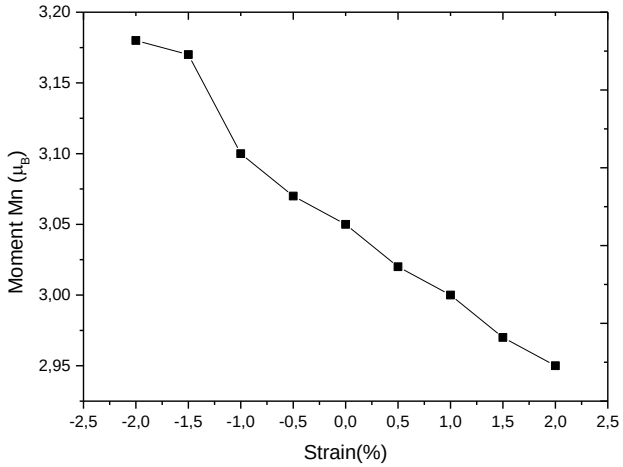

Figure 38: Magnetic moment of AFM Mn3Sn film

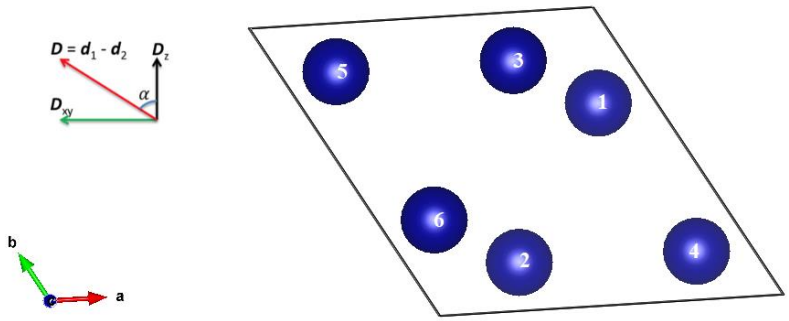

Figure 39: Illustrative figures for magnetic structure and direction of the DM vector.

Now the Hamiltonian for the DMI used in this case has the form:

$$H_{DM}^{1} = D_{xy}(S_1 \times S_5) - D_{xy}(S_2 \times S_6) \tag{5.4}$$

$$H_{DM}^{2} = D_{z}(S_1 \times S_6) - D_{z}(S_2 \times S_5) \tag{5.5}$$

The six possible magnetic structures of Mn_3Sn in a unit cell were examined, two antiparallel domains were chosen from the six types of domains, and the energies were analyzed in different relations of two close unit cells of Mn_3Sn (see **Fig. 38**). The results are shown in **Fig. 39.**

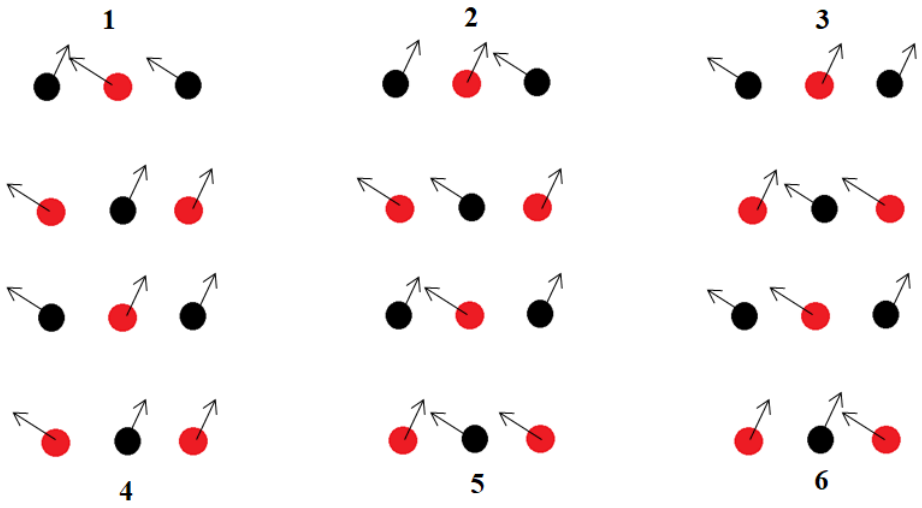

Figure 40: Noncollinear magnetic structures of Mn3Sn, Fmci with i = 0,..., 6, discussed in this contribution.

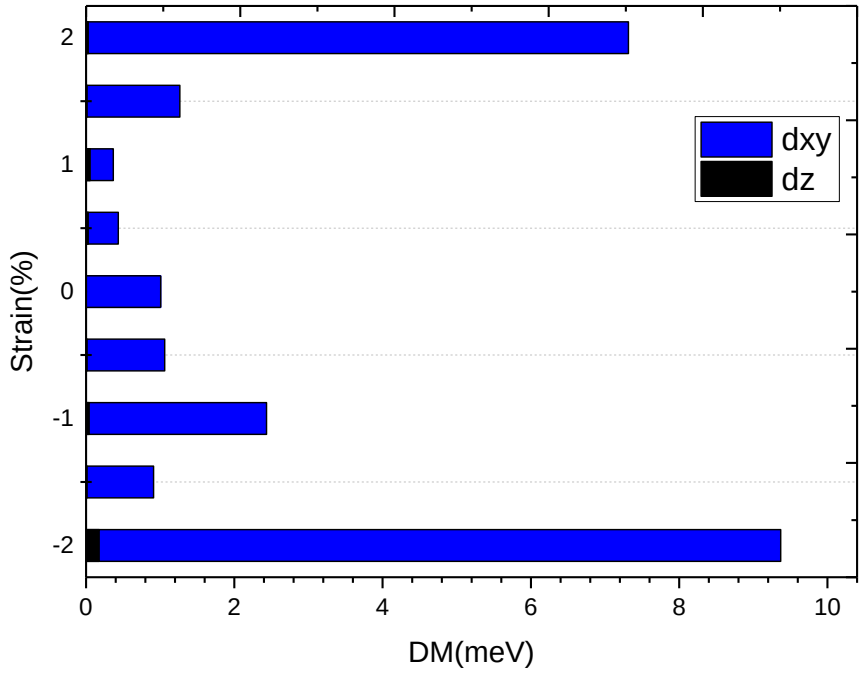

Figure 41: DMI values of AFM Mn3Sn film

As a result, the vector of the DMI shows the greatest amount in the XY axes and the smallest amount along the z axes, which is related to the effect of anisotropy. Through our DFT calculations, it is found that there exist about three different uni-axial anisotropies which coexist on the hard axes [110], [010], and [100], and the easy axes are [001]. We can conclude

that the DM is maximal at the minimum anisotropy. This is required to justify theoretical suggestions which are understood to arise from competition between the DMI and single-ion anisotropy [157]. Also the resulting DM matches well with experimental work [158], on the fact this vector being responsable for triangular spin shape may yield just in-plane moment as the Dij vector need to lie alongside c axis [158]. Also, through the process of raising strain values, there is a sharp upward shift of the DM. This is originated from the piezoelectric effect in Mn_3Sn material [158]. In this way, the strain effect stretches out the FE effect reducing ferromagnetism.

5.4- Phonon calculation of the intermetallic Mn_3Sn compound:

In addition, the phonon dispersion spectra are acquired through the Frozen Phonon Approach that has been developed in PHONOPY code [159, 160] employing the Density Functional Perturbation Theory (DFPT) [161]. The low frequency negative in the acoustic off-plane (ZA) phonon branch near Γ point (see Fig. 42) is linked to structural instability caused by the bending of the two dissimilar metal atoms (Mn/Sn), also reported in some nonmagnetic Janus monolayers [163]. Also it can be observed from **Fig. 42** that there is a direction-dependent swing in phonon spectra. In some measure, this is associated to the NC phenomenon inside the intermetallic compound Mn_3Sn. In the nonmagnetic nomadic step, the dispersion of the phonons involves two hole-type cycles through the different directions about the points Γ-K, and M with high dispersion, which is fairly consistent with the NCM.

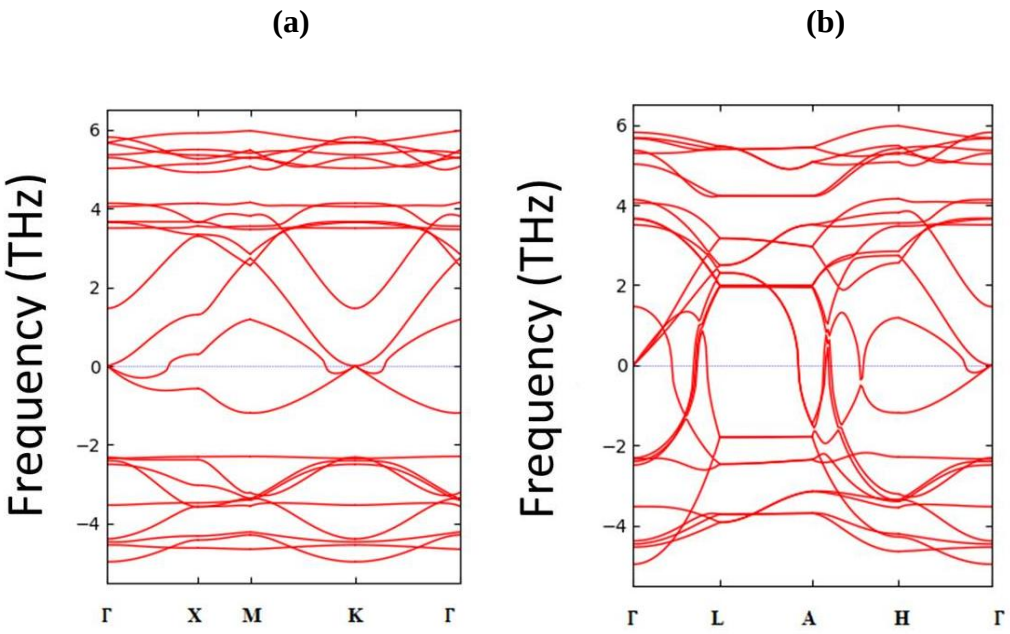

Figure 42: Phonon dispersion of AFM Mn3Sn film

5.5- Ferroelectric properties of the intermetallic Mn_3Sn compound:

To achieve ferroelectrical characteristics, we computed spontaneous polarization (Ps) in each of x, y, and z orientations over the Mn_3Sn thin film employing the berry phase based framework applied on the Wien2k package. Their maximum observed values are found along the z axis (see **Fig. 41**). In contrast, FE matters also exhibit piezoelectricity, meaning the ferroelectricity is tunable upon exposure to strain. The polarization increases in the wake of a biaxial strain, and attains positive values under compressive strain, but with less of a dramatic variation than DMI, A reverse effect has been seen upon applying tensile strain. Here the increase of polarization with applying a compressive strain has been attributed to the decrease in polarization occurring with applying a tensile strain. To gain insight into the source of strain-induced FE transitions in Mn_3Sn intermetallic, we make a comparison with the phonon dispersion, in which FE distortion may be understood through the imaginary phase at point Γ and is abolished under low pressure. One of the major factors explaining the origin of ferroelectricity is the spontaneous symmetry rupture resulting from the opposite vertical shifts

of bimetallic atoms. FE-PE transitions were simulated, disclosing that polarization can be switched by an external perpendicular electrical field. Notably, such FE metals have odd electrons within a unit cell, wherein the conductive electrons predominantly disperse over a surface side, while both ionic and electrical contribution to polarization originate from the opposite side, leading to coexistence of both ferroelectricity and metallicity [164]. Additionally, the occurrence of ferroelectricity in the Weyl semimetal may be related to the layered structure and high electronic anisotropy of the semimetal.

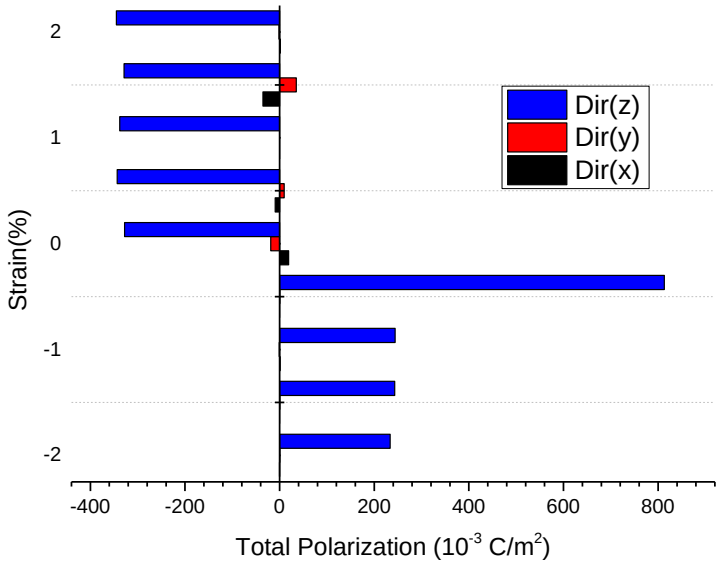

Figure 43: Spontaneous polarization as function as strain effect of AFM Mn3Sn film

5.6- Optical and magneto-optical properties of the intermetallic Mn_3Sn compound:

An investigation of the optical properties was undertaken with consideration of the Ezz and Exy polarization directions, which are considered to be Exx=Eyy=Ezz and Exy=Exz=Eyz based on hexagonal symmetry. Under such case, the absorptive part of the optical conductivity tensor (real diagonal elements and imaginary off-diagonal elements) owed to inter-band transition can be achieved via KK transformation by means of Linear Responsive

theory and the common formulation for both diagonal and off-diagonal elements of the tensor , $\sigma^1_{\alpha\alpha}$ and $\sigma^2_{\alpha\beta}$ [165], respectively.

$$\sigma^1_{\alpha\alpha}(\omega) = \frac{ie^2}{\hbar m^2}\sum_{n\acute{n}} \frac{1}{\omega_{\acute{n}n}}\left(\left(\frac{\langle n|P_\alpha|\acute{n}\rangle\langle\acute{n}|P_\alpha|n\rangle}{\omega-\omega_{\acute{n}n}+i\Gamma} + \frac{\langle n|P_\alpha|\acute{n}\rangle\langle\acute{n}|P_\alpha|n\rangle}{\omega+\omega_{\acute{n}n}+i\Gamma}\right)\right) \tag{5.6}$$

$$\sigma^2_{\alpha\beta}(\omega) = \frac{ie^2}{\hbar m^2}\sum_{n\acute{n}} \frac{1}{\omega_{\acute{n}n}}\left(\left(\frac{\langle n|P_\alpha|\acute{n}\rangle\langle\acute{n}|P_\beta|n\rangle}{\omega-\omega_{\acute{n}n}+i\Gamma} + \frac{\langle n|P_\beta|\acute{n}\rangle\langle\acute{n}|P_\alpha|n\rangle}{\omega+\omega_{\acute{n}n}+i\Gamma}\right)\right) \tag{5.7}$$

According to this formula, which is commonly known as the Kubo equation α, β are Cartesian coordinate indices, and e, m are the electron charge and mass, respectively. ω is the frequency of the incoming electromagnetic radiation, $\hbar\omega_{n\acute{n}}$ is the energy difference between the initial and final one-particle states $|n\rangle$ and $|n'\rangle$, $(P_x, P_y, P_z) = P$ is the momentum operator, and Γ is inversely proportional to the lifetime τ of the excited state.

The complex Kerr angle of a specimen with rotational symmetry higher than 3 times for polar shapes can easily be written as follows [166]:

$$\theta_K \cong \Re\left(\frac{\sigma_{xy}(\omega)}{\sigma_{zz}(\omega)\sqrt{1-\frac{4\pi i}{\omega}\sigma_{zz}(\omega)}}\right) \tag{5.8}$$

This provides ample proof of the fact of the Kerr rotation - as well as the Kerr ellipticity - which is directly correlated with the off-diagonal element $\sigma_{xy}(\omega)$ of the tensor of the conductivity.

Such symmetry restrictions apply only to calculations of NR and SR. In those instances, the components SP and SD can be assessed individually, where the respective real parts of them are derived from the KK transformation (see below). In the MO case, the symmetry is diminished from the influence of magnetic induction and the loss of inverse time symmetry resulting from SOC. The later results in non-diagonal antisymmetric constituents. The respective imaginary components are once to be determined with the help of the KK analysis. As a result, the absorptive parts of optical conductivities of diagonal (σ^1_{zz}) and off-diagonal (σ^2_{xy}) of the Mn_3Sn compound are shown in **Fig. 42**. It is obvious that the diagonal σ^1_{zz} has

precisely an identical form like σ_{xy}^{2} although σ_{zz}^{1} is superior rather then σ_{xy}^{2}. As well, the distortion factor of thin films has a slight influence on optical conductivity. It means that all these phenomena of gyromagnetics and MO occurring in the well-known situation will also exist in the non-collinear Mn_3Sn AFM case. [167].

After some discussion about the magnetic and optical properties of the Mn_3Sn alloys, we next focus attention on the MO characteristics of these alloys. From complex Kerr angle diagrams displayed in the **Fig. 43**, their main features are shown as below. Based on this Figure, we may notice a slight wobble near 0 degree, which is assignable to KK equation. The same behavior is found for undeformed thin films, One may see here that Kerr rotation angles (θK) have the highest in the AFM as compared to FM state These findings arise from a noncollinear AFM character of Mn_3Sn, being similar to behavior seen on the Mn_3Ir compound [168]. Alternatively, reasonable theoretical or experimental progress reveals that systems like NC and AFM can display a substantial AHE response under zero applied magnetic fields, inspite of null magnetization. [168]. Given that the AHE has similar symmetry requisites as MOKE [169], it is feasible that this same AFM category may show Kerr rotation. Hence, its recent discovery by experiment that there is a strong AHE within NC Mn_3Sn AFM and its soft magnetic field exposure answer [150] shows some promise for potentially an important MOKE feature.

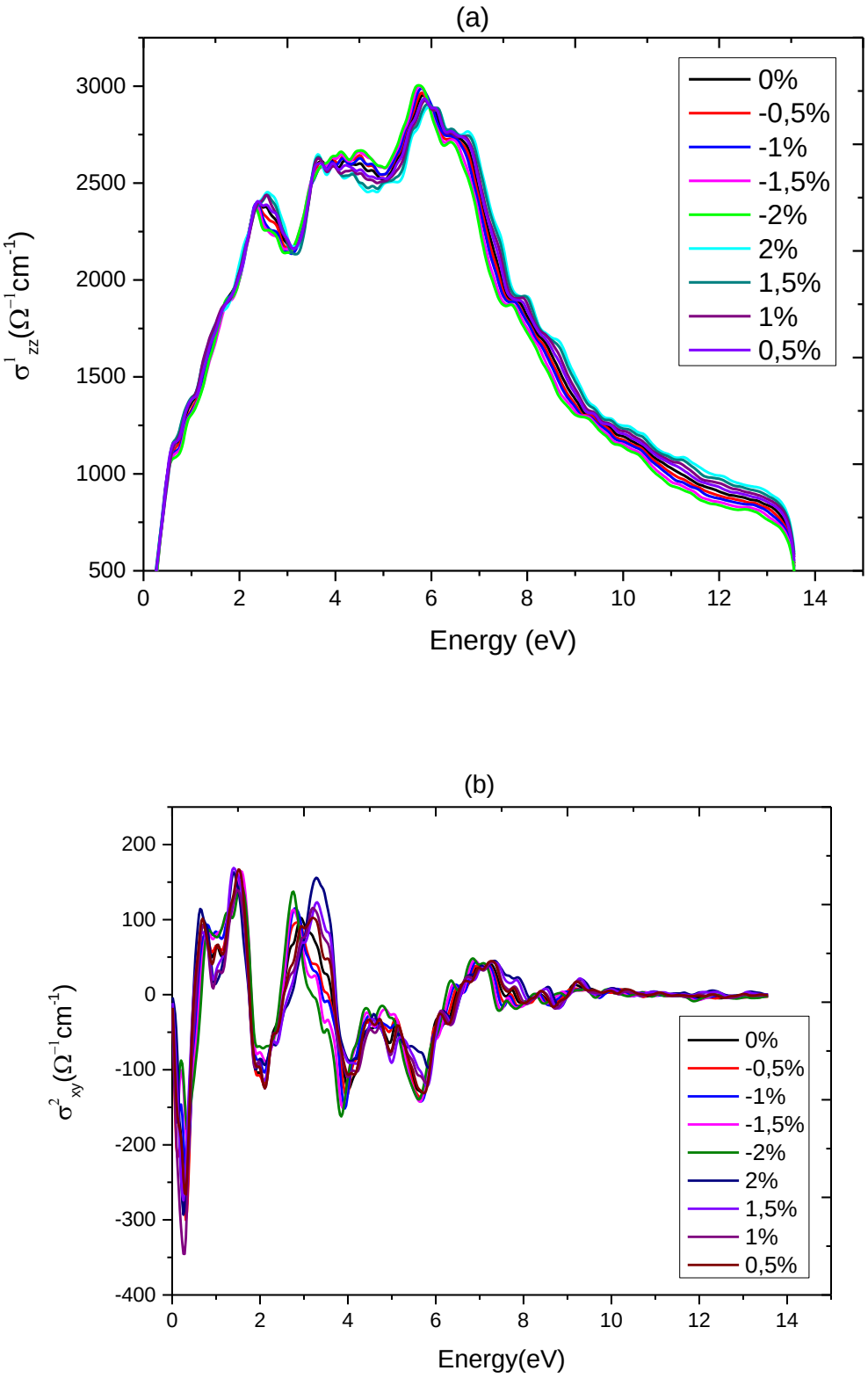

Figure 44: Energy dependence of the optical conductivity in AFM Mn3Sn film: (a) diagonal (σ1zz) and (b) off-diagonal (σ2xy).

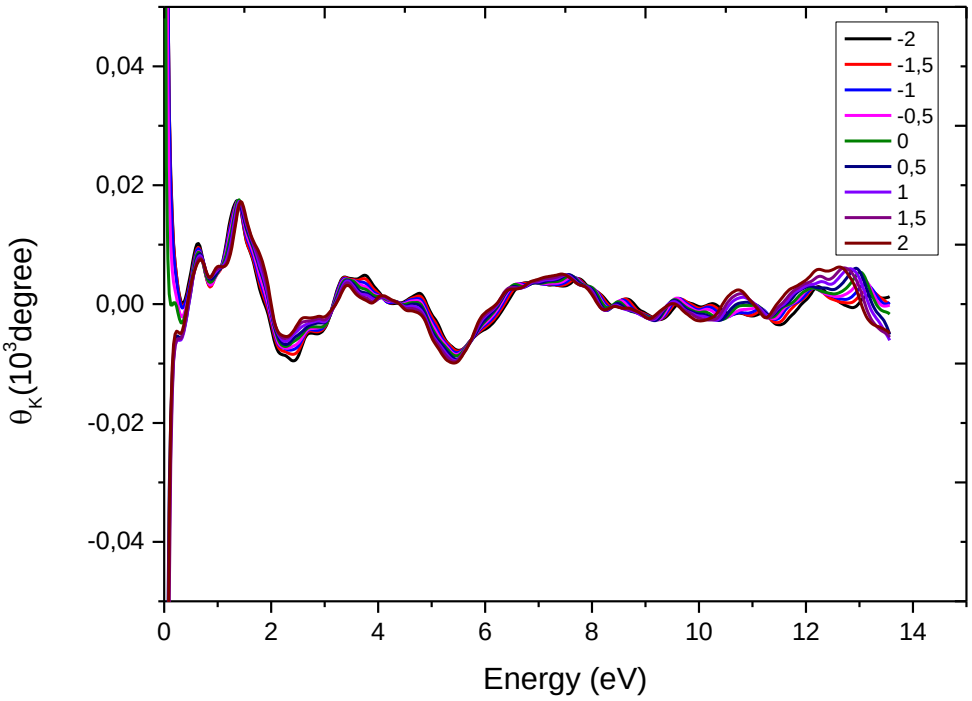

Figure 45: MO spectra of AFM Mn3Sn film

Conclusion:

Briefly, we investigate the impact made by tensile and compressive strain in the electronic structure, magnetic, FE, optical and MO properties of Mn_3Sn compound employing first principles calculations. As well, this composite is a prime subject for studying DMI Vector, primarily related to non-collinear magnetism behavior arising from the tight breathing kagome structure of Sn atoms in the middle of the hexagon Mn atoms. Also, on the introduction of deformation effects into the thin film, it affects the DMI and the optical properties. Lastly, the connection between non-collinear and optical properties have been explored and on the basis of this, it is concluded that the interaction DM were responsible for the co-existence of ferroelectricity and MO in the Mn_3Sn hexagon complex material.

General conclusion:

Intermetallic « RT_2X_2 » and « Mn_3Z » have been considered as promising candidates to replace rare earth manganite $RMnO_3$ or RMn_2O_5 in room or low temperature magnetic refrigeration applications. Also, the magnetic weyl semimetal Mn_3Sn has appealing prospect for spintronic to replace the half metallic FM oxides such as CrO_2 and $SrFeMoO_6$ due to their various crystal structures and magnetic properties for design of reliable high-density memories.

The main objective of this thesis was the combination of theoretical studies on the structural, electronic and magnetic properties of the Chiral intermetallic materials. We have sought to understand the origin of the noncollinear structure of those materials by studying their structural, electronic and magnetic properties using different numerical tools such as DFT, NC, phonon calculations, and MC.

Indeed, we started our thesis work by studies the structural, electronic, magnetic, and magnetocaloric properties of intermetallic $TbCu_2Si_2$ compound using several theoretical methods such as: First principal calculations and MC. Through, the Ab-initio calculations, the values of magnetic moment and the exchange coupling interactions are found to be $5.93\mu_B$ and J_1=0.58 meV, J_2=-0.69 meV and J_3= 0.41 meV, respectively. The T_N obtained is in a good agreement with the experimental results. Around T_N, a large MCE is found, the maximal values of ΔS_M^{Max} and RCP are 40.78 J/Kg.K, 71.58 J/kg, respectively, under applied external magnetic field of h=2.0 T. The good magnetocaloric properties indicate the applicability of $TbCu_2Si_2$ for the magnetic refrigeration around T_N.

On the other hand, the magnetic, magnetocaloric, and transport properties of the intermetallic $LaMn_2Si_2$ compound are studied by using several theoretical methods such as first-principle

calculations and MC. Moreover, the exchange coupling interactions and anisotropy values are (J_1=298.35meV, J_2=61.77 meV) and Δ= 7.4849×10^{-2} meV, respectively by using ab-initio calculations. The T_C obtained using MC is in good agreement with the experimental results. Around T_C, a large magnetocaloric effect is found, and the maximal values of ΔS_M and RCP are 3.34 J/Kg.K, and 127.3J/kg respectively, under an applied external magnetic field equal to 7.0 T. The intermetallic $LaMn_2Si_2$ compound shows the large magnetocaloric effect, which can be used for future cooling devices due to the large MAE. By calculation of the electrical and thermal conductivity, we found that this compound is an appropriate choice for a thermomagnetic generator.

The last chapter of this thesis concerns the effect of tensile and compressive strains on the electronic structure, magnetic, FE, optic, and MO properties of the Mn_3Sn compound are investigated by using the first-principles calculations. Also, this compound has an important candidate to study the DMI, it's due to the presence of noncollinear magnetism behavior associated with the kagome lattice from close-packed breathing with Sn atoms at the center of Mn hexagonal. Moreover, the introduction of the strain effect on the thin-film affects the DM interactions and optical properties. Finally, the relationship between noncollinear and optical properties was investigated and we conclude that the DMI was responsible for the coexistence of Ferroelectricity and MO in the hexagonal Mn_3Sn compound.

Bibliography :

[1] Koehler, W.C., 1965. Magnetic Properties of Rare-Earth Metals and Alloys. Journal of Applied Physics 36, 1078–1087. https://doi.org/10.1063/1.1714108

[2] Szlawska, M., Majewicz, M., Kaczorowski, D., 2016. Ferromagnetic ordering in single-crystalline U2RhSi3 with fully ordered crystal structure. Journal of Alloys and Compounds 662, 208–212. https://doi.org/10.1016/j.jallcom.2015.11.232

[3] Petrovic, C., Pagliuso, P.G., Hundley, M.F., Movshovich, R., Sarrao, J.L., Thompson, J.D., Fisk, Z., Monthoux, P., 2001. Heavy-fermion superconductivity in $CeCoIn_5$ at 2.3 K. J. Phys.: Condens. Matter 13, L337–L342. https://doi.org/10.1088/0953-8984/13/17/103

[4] Steglich, F., Aarts, J., Bredl, C.D., Lieke, W., Meschede, D., Franz, W., Schäfer, H., 1979. Superconductivity in the Presence of Strong Pauli Paramagnetism: Ce Cu 2 Si 2. Phys. Rev. Lett. 43, 1892–1896. https://doi.org/10.1103/PhysRevLett.43.1892

[5] Ban, Z., Sikirica, M., 1965. The crystal structure of ternary silicides ThM_2Si_2 (M = Cr, Mn, Fe, Co, Ni and Cu). Acta Cryst 18, 594–599. https://doi.org/10.1107/S0365110X6500141X

[6] Eisenmann, B., May, N., Müller, W., Schäfer, H., 1972. Eine neue strukturelle Variante des $BaAl_4$ -Typs: Der $CaBe_2Ge_2$ -Typ / A New Structural Variant of the $BaAl_4$ -Type: The $CaBe_2Ge_2$ -Type. Zeitschrift für Naturforschung B 27, 1155–1157. https://doi.org/10.1515/znb-1972-1008

[7] Marchand, R., Jeitschko, W., 1978. Ternary lanthanoid-transition metal pnictides with ThCr2Si2-type structure. Journal of Solid State Chemistry 24, 351–357. https://doi.org/10.1016/0022-4596(78)90026-9

[8] Rogl, P., 1984. Chapter 51 Phase equilibria in ternary and higher order systems with rare earth elements and silicon, in: Handbook on the Physics and Chemistry of Rare Earths. Elsevier, pp. 1–264. https://doi.org/10.1016/S0168-1273(84)07004-5

[9] SzytuŁa, A., Ptasiewicz-Bak, H., Leciejewicz, J., BaŻela, W., 1989. Magnetic ordering in RCoSi2 (R = Tb, Dy, Ho) compounds. Journal of Magnetism and Magnetic Materials 80, 189–194. https://doi.org/10.1016/0304-8853(89)90116-9

[10] Szytula, A., 1992. Magnetic properties of 1:2:2 rare-earth and actinide intermetallics. Journal of Alloys and Compounds 181, 123–134. https://doi.org/10.1016/0925-8388(92)90304-R

[11] Campbell, I.A., 1972. Indirect exchange for rare earths in metals. J. Phys. F: Met. Phys. 2, L47–L50. https://doi.org/10.1088/0305-4608/2/3/004

[12] Sanada, N., Yoshioka, T., Watanuki, R., Suzuki, K., 2012. Elastic Constants of $NdCu_2Ge_2$. J. Phys.: Conf. Ser. 400, 032078. https://doi.org/10.1088/1742-6596/400/3/032078

[13] Zener, C., 1951. Interaction between the d -Shells in the Transition Metals. II. Ferromagnetic Compounds of Manganese with Perovskite Structure. Phys. Rev. 82, 403–405. https://doi.org/10.1103/PhysRev.82.403

[14] de Gennes, P.-G., 1960. Effects of Double Exchange in Magnetic Crystals. Phys. Rev. 118, 141–154. https://doi.org/10.1103/PhysRev.118.141

[15] Ruderman, M.A., Kittel, C., 1954. Indirect Exchange Coupling of Nuclear Magnetic Moments by Conduction Electrons. Phys. Rev. 96, 99–102. https://doi.org/10.1103/PhysRev.96.99

[16] Kasuya, T., 1956. A Theory of Metallic Ferro- and Antiferromagnetism on Zener's Model. Progress of Theoretical Physics 16, 45–57. https://doi.org/10.1143/PTP.16.45

[17] Yosida, K., 1957. Magnetic Properties of Cu-Mn Alloys. Phys. Rev. 106, 893–898. https://doi.org/10.1103/PhysRev.106.893

[18] Blundell, S., Thouless, D., 2003. *Magnetism in Condensed Matter*. American Journal of Physics 71, 94–95. https://doi.org/10.1119/1.1522704

[19] CAMPBELL, I. A. Journal of Physics F. vol. 2, p. L47 – L50 (1972);

[20] BROOKS, MSS.; Eriksson Olle and Borje Johansson. Journal of Physics: Condensed Matter, vol. 1, p. 5861 – 5874 (1989);

[21] A.P. Guimaraes, in: Magnetism and Magnetic Resonance in Solids, John Wesley & Sons Inc, 1998, pp. 47–49.

[22] Krén, E., Kádár, G., 1970. Neutron diffraction study of Mn3Ga. Solid State Communications 8, 1653–1655. https://doi.org/10.1016/0038-1098(70)90484-9

[23] Zimmer, G.J., Krén, E., 1973. Magnetic Structure of DO19 Type Compunds. AIP Conference Proceedings 10, 1379–1383. https://doi.org/10.1063/1.2946799

[24] Zhang, Y., Sun, Y., Yang, H., Železný, J., Parkin, S.P.P., Felser, C., Yan, B., 2017. Strong anisotropic anomalous Hall effect and spin Hall effect in the chiral antiferromagnetic compounds Mn3X (X=Ge, Sn, Ga, Ir, Rh, and Pt). Phys. Rev. B 95, 075128. https://doi.org/10.1103/PhysRevB.95.075128

[25] Tomiyoshi, S., Yamaguchi, Y., Nagamiya, T., 1983. Triangular spin configuration and weak ferromagnetism of Mn3Ge. Journal of Magnetism and Magnetic Materials 31–34, 629–630. https://doi.org/10.1016/0304-8853(83)90610-8

[26] Tomiyoshi, S., Yamaguchi, Y., 1982. Magnetic Structure and Weak Ferromagnetism of Mn3Sn Studied by Polarized Neutron Diffraction. Journal of the Physical Society of Japan 51, 2478–2486. https://doi.org/10.1143/JPSJ.51.2478

[27] P J Brown, V Nunez, F Tasset, J B Forsyth, P Radhakrishna, 1990. Determination of the magnetic structure of Mn3Sn using generalized neutron polarization analysis. Journal of Physics: Condensed Matter 2, 9409. https://doi.org/10.1088/0953-8984/2/47/015

[28] Radhakrishna, P., Cable, J.W., 1992. Magnetic excitations in the triangular antiferromagnet Mn3Sn. Journal of Magnetism and Magnetic Materials 104–107, 1065–1066. https://doi.org/10.1016/0304-8853(92)90492-7

[29] Cable, J.W., Wakabayashi, N., Radhakrishna, P., 1993. Magnetic excitations in the triangular antiferromagnets Mn3Sn and Mn3Ge. Phys. Rev. B 48, 6159–6166. https://doi.org/10.1103/PhysRevB.48.6159

[30] Kübler, J., William, A.R., Sommers, C.B., 1983. Formation and coupling of magnetic moments in Heusler alloys. Phys. Rev. B 28, 1745–1755. https://doi.org/10.1103/PhysRevB.28.1745

[31] Wurmehl, S., Kandpal, H.C., Fecher, G.H., Felser, C., 2006. Valence electron rules for prediction of half-metallic compensated-ferrimagnetic behaviour of Heusler compounds with complete spin polarization. Journal of Physics: Condensed Matter 18, 6171. https://doi.org/10.1088/0953-8984/18/27/001

[32] Winterlik, J., Chadov, S., Gupta, A., Alijani, V., Gasi, T., Filsinger, K., Balke, B., Fecher, G.H., Jenkins, C.A., Casper, F., Kübler, J., Liu, G.-D., Gao, L., Parkin, S.S.P., Felser, C., 2012. Design Scheme of New Tetragonal Heusler Compounds for Spin-Transfer Torque Applications and its Experimental Realization. Advanced Materials 24, 6283–6287. https://doi.org/10.1002/adma.201201879

[33] Ikeda, S., Miura, K., Yamamoto, H., Mizunuma, K., Gan, H.D., Endo, M., Kanai, S., Hayakawa, J., Matsukura, F., Ohno, H., 2010. A perpendicular-anisotropy CoFeB–MgO magnetic tunnel junction. Nature Materials 9, 721–724. https://doi.org/10.1038/nmat2804

[34] J. M. Seminario, “An introduction to density functional theory in chemistry,”in *Modern Density Functional Theory* (J. Seminario and P. Politzer, eds.), vol. 2 of *Theoretical and Computational Chemistry*, pp. 1-27, Elsevier, 1995.

[35] C. Daniel, “Density functional theories and coordination chemistry,” in *Reference Module in Chemistry, Molecular Sciences and Chemical Engineering*, Elsevier, 2020.

[36] J. M. Combes, P. Duclos, and R. Seiler, “*The Born-Oppenheimer Approximation”*, pp. 185-213. Boston, MA: Springer US, 1981.

[37] F. Reines and H. W. Sobel, “Test of the pauli exclusion principle for atomic electrons” *Phys. Rev. Lett.*, vol. 32, pp. 954-954, Apr 1974.

[38] A. Görling, “ Density-functional theory beyond the hohenberg-kohn theorem,” *Phys.Rev. A*, vol. 59, pp. 3359-3374, May 1999

[39] W. Kohn and L. J. Sham, “Self-consistent equations including exchange and correlation effects,” *Phys. Rev.*, vol. 140, pp. A1133-A1138, Nov 1965.

[40] S. Kurth, M. Marques, M. Lüders, and E. K. U. Gross, “Local density approximation for superconductors,” *Phys. Rev. Lett.*, vol. 83, pp. 2628-2631, Sep 1999. https://doi.org/10.1021/jp960669l

[41] Z. Wu and R. E. Cohen, “More accurate generalized gradient approximation for solids,” *Phys. Rev. B*, vol. 73, p. 235116, Jun 2006.

[42] H. J. F. Jansen and A. J. Freeman, “Total-energy full-potential linearized augmented-plane-wave method for bulk solids: Electronic and structural properties of tungsten,” *Phys. Rev. B*, vol. 30, pp. 561-569, Jul 1984.

[43] E. Sjöstedt, L. Nordstr¨om, and D. Singh, “An alternative way of linearizing the augmented plane-wave method,” *Solid State Communications*, vol. 114, no. 1, pp. 15- 20, 2000.

[44] Coey, J.M.D., 1987. Noncollinear spin structures. Can. J. Phys. 65, 1210–1232. https://doi.org/10.1139/p87-197

[45] Keffer, F., 1966. Spin Waves, in: Wijn, H.P.J. (Ed.), Ferromagnetism / Ferromagnetismus. Springer Berlin Heidelberg, Berlin, Heidelberg, pp. 1–273. https://doi.org/10.1007/978-3-642-46035-7_1

[46] Hohenberg, P., Kohn, W., 1964. Inhomogeneous Electron Gas. Phys. Rev. 136, B864–B871. https://doi.org/10.1103/PhysRev.136.B864

[47] Kohn, W., 1996. Density Functional and Density Matrix Method Scaling Linearly with the Number of Atoms. Phys. Rev. Lett. 76, 3168–3171. https://doi.org/10.1103/PhysRevLett.76.3168

[48] J B Staunton, 1994. The electronic structure of magnetic transition metallic materials. Reports on Progress in Physics 57, 1289. https://doi.org/10.1088/0034-4885/57/12/002

[49] B L Gyorffy, A J Pindor, J Staunton, G M Stocks, H Winter, 1985. A first-principles theory of ferromagnetic phase transitions in metals. Journal of Physics F: Metal Physics 15, 1337. https://doi.org/10.1088/0305-4608/15/6/018

[50] Marchand, R., Jeitschko, W., 1978. Ternary lanthanoid-transition metal pnictides with ThCr2Si2-type structure. Journal of Solid State Chemistry 24, 351–357. https://doi.org/10.1016/0022-4596(78)90026-9

[51] Sandratskii, L.M., Guletskii, P.G., 1989. Energy band structure of BBC iron at finite temperatures. Journal of Magnetism and Magnetic Materials 79, 306–320. https://doi.org/10.1016/0304-8853(89)90185-6

[52] J Sticht, K-H Höck, J Kübler, 1989. Non-collinear itinerant magnetism: the case of Mn3Sn. Journal of Physics: Condensed Matter 1, 8155. https://doi.org/10.1088/0953-8984/1/43/016

[53] Y Tsunoda, 1989. Spin-density wave in cubic γ-Fe and γ-Fe100-xCox precipitates in Cu. Journal of Physics: Condensed Matter 1, 10427. https://doi.org/10.1088/0953-8984/1/51/015

[54] O N Mryasov, A I Liechtenstein, L M Sandratskii, V A Gubanov, 1991. Magnetic structure of FCC iron. Journal of Physics: Condensed Matter 3, 7683. https://doi.org/10.1088/0953-8984/3/39/013

[55] Uhl, M., Sandratskii, L.M., Kübler, J., 1992. Electronic and magnetic states of γ-Fe. Journal of Magnetism and Magnetic Materials 103, 314–324. https://doi.org/10.1016/0304-8853(92)90202-Y

[56] Lorenz, R., Hafner, J., Jaswal, S.S., Sellmyer, D.J., 1995. Disorder and Noncollinear Magnetism in Permanent-Magnet Materials with the ThMn12 Structure. Phys. Rev. Lett. 74, 3688–3691. https://doi.org/10.1103/PhysRevLett.74.3688

[57] Liebs, M., Hummler, K., Fähnle, M., 1995. Influence of structural disorder on magnetic order: An ab initio study of amorphous Fe, Co, and Ni. Phys. Rev. B 51, 8664–8667. https://doi.org/10.1103/PhysRevB.51.8664

[58] A. V. Smirnov, A. M. Bratkovsky, 1996. Non-collinear magnetism in Al-Mn topologically disordered systems. Europhysics Letters 33, 527. https://doi.org/10.1209/epl/i1996-00373-4

[59] A. Vega, D. Stoeffler, H. Dreyssé, C. Demangeat, 1995. Magnetic-Order Transition in Thin Fe Overlayers on Cr: Role of the Interfacial Roughness. Europhysics Letters 31, 561. https://doi.org/10.1209/0295-5075/31/9/010

[60] Kudrnovsky, J., Turek, I., Drchal, V., Masek, J., Maca, F., & Weinberger, P. (2003). Ab initio study of Curie temperatures of diluted III-V magnetic semiconductors. *arXiv*. https://doi.org/10.48550/arXiv.cond-mat/0302441

[61] Antropov, V.P., Katsnelson, M.I., van Schilfgaarde, M., Harmon, B.N., 1995. Ab-Initio Spin Dynamics in Magnets. Phys. Rev. Lett. 75, 729–732. https://doi.org/10.1103/PhysRevLett.75.729

[62] U von Barth, L Hedin, 1972. A local exchange-correlation potential for the spin polarized case. i. Journal of Physics C: Solid State Physics 5, 1629. https://doi.org/10.1088/0022-3719/5/13/012

[63] Williams, A.R., Kübler, J., Gelatt, C.D., 1979. Cohesive properties of metallic compounds: Augmented-spherical-wave calculations. Phys. Rev. B 19, 6094–6118. https://doi.org/10.1103/PhysRevB.19.6094

[64] Kohn, W., Rostoker, N., 1954. Solution of the Schrodinger Equation in Periodic Lattices with an Application to Metallic Lithium. Phys. Rev. 94, 1111–1120. https://doi.org/10.1103/PhysRev.94.1111

[65] Dederichs, P.H., Blügel, S., Zeller, R., Akai, H., 1984. Ground States of Constrained Systems: Application to Cerium Impurities. Phys. Rev. Lett. 53, 2512–2515. https://doi.org/10.1103/PhysRevLett.53.2512

[66] L M Sandratskii, E N Kuvaldin, 1991. Band-theory approach to the study of local magnetization fluctuations in Fe and Ni. Journal of Physics: Condensed Matter 3, 7663. https://doi.org/10.1088/0953-8984/3/39/012

[67] K Schwarz, P Mohn, 1984. Itinerant metamagnetism in YCO2. Journal of Physics F: Metal Physics 14, L129. https://doi.org/10.1088/0305-4608/14/7/008

[68] A K Rajagopal, 1978. Inhomogeneous relativistic electron gas. Journal of Physics C: Solid State Physics 11, L943. https://doi.org/10.1088/0022-3719/11/24/002

[69] A H MacDonald, S H Vosko, 1979. A relativistic density functional formalism. Journal of Physics C: Solid State Physics 12, 2977. https://doi.org/10.1088/0022-3719/12/15/007

[70] Eschrig, H., Seifert, G., Ziesche, P., 1985. Current density functional theory of quantum electrodynamics. Solid State Communications 56, 777–780. https://doi.org/10.1016/0038-1098(85)90307-2

[71] Sandratskii, L.M., Kübler, J., Zahn, P., Mertig, I., 1994. Electronic structure, magnetic, and Fermi-surface properties of ${\mathrm{UPd}}_{2}$${\mathrm{Al}}_{3}$. Phys. Rev. B 50, 15834–15842. https://doi.org/10.1103/PhysRevB.50.15834

[72] A H MacDonald, W E Picket, D D Koelling, 1980. A linearised relativistic augmented-plane-wave method utilising approximate pure spin basis functions. Journal of Physics C: Solid State Physics 13, 2675. https://doi.org/10.1088/0022-3719/13/14/009

[73] O Eriksson, B Johansson, M S S Brooks, 1989. Meta-magnetism in UCoAl. Journal of Physics: Condensed Matter 1, 4005. https://doi.org/10.1088/0953-8984/1/25/012

[74] Binder, K., 1972. Statistical mechanics of finite three-dimensional Ising models. Physica 62, 508–526. https://doi.org/10.1016/0031-8914(72)90237-6

[75] Metropolis, N., Rosenbluth, A.W., Rosenbluth, M.N., Teller, A.H., Teller, E., 1953. Equation of State Calculations by Fast Computing Machines. J. Chem. Phys. 21, 1087–1092. https://doi.org/10.1063/1.1699114

[76] Jordan, H.F., Fosdick, L.D., 1968. Three-Particle Effects in the Pair Distribution Function for He4Gas. Phys. Rev. 171, 128–149. https://doi.org/10.1103/PhysRev.171.128

[77] Spanier, J., 2010. Monte Carlo Methods, in: Azmy, Y., Sartori, E. (Eds.), Nuclear Computational Science: A Century in Review. Springer Netherlands, Dordrecht, pp. 117–165. https://doi.org/10.1007/978-90-481-3411-3_3

[78] Glauber, R.J., 1963. Time-Dependent Statistics of the Ising Model. J. Math. Phys. 4, 294–307. https://doi.org/10.1063/1.1703954

[79] Garces, E., van Blommestein, K., Anthony, J., Hillegas-Elting, J., Daim, T., Yoon, B.-S., 2017. Technology domain analysis: A case of energy-efficient advanced commercial refrigeration technologies. Sustainable Production and Consumption 12, 221–233. https://doi.org/10.1016/j.spc.2017.08.002

[80] Chen, X., Omer, S., Worall, M., Riffat, S., 2013. Recent developments in ejector refrigeration technologies. Renewable and Sustainable Energy Reviews 19, 629–651. https://doi.org/10.1016/j.rser.2012.11.028

[81] Romero Gómez, J., Ferreiro Garcia, R., Carbia Carril, J., Romero Gómez, M., 2013. Experimental analysis of a reciprocating magnetic refrigeration prototype. International Journal of Refrigeration 36, 1388–1398. https://doi.org/10.1016/j.ijrefrig.2013.01.008

[82] Benedict, M.A., Sherif, S.A., Schroeder, M., Beers, D.G., 2017. The impact of magnetocaloric properties on refrigeration performance and machine design. International Journal of Refrigeration 74, 576–583. https://doi.org/10.1016/j.ijrefrig.2016.12.004

[83] Romero Gómez, J., Ferreiro Garcia, R., De Miguel Catoira, A., Romero Gómez, M., 2013. Magnetocaloric effect: A review of the thermodynamic cycles in magnetic refrigeration. Renewable and Sustainable Energy Reviews 17, 74–82. https://doi.org/10.1016/j.rser.2012.09.027

[84] Franco, V., Blázquez, J.S., Ipus, J.J., Law, J.Y., Moreno-Ramírez, L.M., Conde, A., 2018. Magnetocaloric effect: From materials research to refrigeration devices. Progress in Materials Science 93, 112–232. https://doi.org/10.1016/j.pmatsci.2017.10.005

[85] Brück, E., 2005. Developments in magnetocaloric refrigeration. Journal of Physics D: Applied Physics 38, R381. https://doi.org/10.1088/0022-3727/38/23/R01

[86] Phan, M.-H., Yu, S.-C., 2007. Review of the magnetocaloric effect in manganite materials. Journal of Magnetism and Magnetic Materials 308, 325–340. https://doi.org/10.1016/j.jmmm.2006.07.025

[87] Ouyang, Z.W., Wang, F.W., Hang, Q., Liu, W.F., Liu, G.Y., Lynn, J.W., Liang, J.K., Rao, G.H., 2005. Temperature dependent neutron powder diffraction study of the Laves phase compound TbCo2. Journal of Alloys and Compounds 390, 21–25. https://doi.org/10.1016/j.jallcom.2004.08.028

[88] Liu, X.B., Altounian, Z., 2006. Magnetocaloric effect in Mn5Ge3−xSix pseudobinary compounds. Journal of Applied Physics 99, 08Q101. https://doi.org/10.1063/1.2148332

[89] Long, Y., Zhang, Z.Y., Wen, D., Wu, G.H., Ye, R.C., Chang, Y.Q., Wan, F.R., 2005. Phase transition processes and magnetocaloric effects in the Heusler alloys NiMnGa with concurrence of magnetic and structural phase transition. Journal of Applied Physics 98, 046102. https://doi.org/10.1063/1.1991995

[90] Ennassiri, N., Tahiri, N., El Bounagui, O., Ez-Zahraouy, H., Benyoussef, A., 2018. Structural, electronic, magnetic, and magnetocaloric properties in metallic antiperovskite compound Mn3GaC. Materials Research Bulletin 98, 335–339. https://doi.org/10.1016/j.materresbull.2017.10.029

[91] Ennassiri, N., Tahiri, N., El Bounagui, O., Ez-Zahraouy, H., Benyoussef, A., 2018. Magnetic, magnetocaloric and transport properties in AlCMn3 antiperovskite compound. Journal of Alloys and Compounds 741, 1196–1202. https://doi.org/10.1016/j.jallcom.2018.01.223

[92] Emre, B., Aksoy, S., Posth, O., Acet, M., Duman, E., Lindner, J., Elerman, Y., 2008. Antiferromagnetic-ferromagnetic crossover in La0.5Pr0.5Mn2Si2 and its consequences on magnetoelastic and magnetocaloric properties. Phys. Rev. B 78, 144408. https://doi.org/10.1103/PhysRevB.78.144408

[93] Szytuła, A., Leciejewicz, J., 1989. Chapter 83 Magnetic properties of ternary intermetallic compounds of the RT2X2 type, in: Handbook on the Physics and Chemistry of Rare Earths. Elsevier, pp. 133–211. https://doi.org/10.1016/S0168-1273(89)12007-8

[94] Bazine, W., Tahiri, N., El Bounagui, O., Ez-Zahraouy, H., Benyoussef, A., 2019. Structural, electronic, magnetic, and magnetocaloric properties in intermetallic compound TbCu2Si2. Journal of Magnetism and Magnetic Materials 481, 72–76. https://doi.org/10.1016/j.jmmm.2019.02.095

[95] Samanta, T., Das, I., Banerjee, S., 2007. Giant magnetocaloric effect in antiferromagnetic ErRu2Si2 compound. Appl. Phys. Lett. 91, 152506. https://doi.org/10.1063/1.2798594

[96] Kumar, P., Suresh, K.G., Nigam, A.K., Magnus, A., Coelho, A.A., Gama, S., 2008. Pressure-induced changes in the magnetic and magnetocaloric properties of RMn2Ge2 (R=Sm, Gd). Phys. Rev. B 77, 224427. https://doi.org/10.1103/PhysRevB.77.224427

[97] Wada, H., Tanabe, Y., Hagiwara, K., Shiga, M., 2000. Magnetic phase transition and magnetocaloric effect of DyMn2Ge2. Journal of Magnetism and Magnetic Materials 218, 203–210. https://doi.org/10.1016/S0304-8853(00)00410-8

[98] Li, L., Hu, G., Umehara, I., Huo, D., Hutchison, W.D., Namiki, T., Nishimura, K., 2013. Magnetic properties and magnetocaloric effect of GdCr2Si2 compound under hydrostatic pressure. Journal of Alloys and Compounds 575, 1–4. https://doi.org/10.1016/j.jallcom.2013.04.081

[99] Li, L., Hu, G., Umehara, I., Huo, D., Hutchison, W.D., Namiki, T., Nishimura, K., 2013. Magnetic properties and magnetocaloric effect of GdCr2Si2 compound under hydrostatic pressure. Journal of Alloys and Compounds 575, 1–4. https://doi.org/10.1016/j.jallcom.2013.04.081

[100] Mo, Z.-J., Shen, J., Yan, L.-Q., Gao, X.-Q., Wang, L.-C., Tang, C.-C., Wu, J.-F., Sun, J., Shen, B.-G., 2014. Magnetic properties and magnetocaloric effect in the RCu2Si2 and RCu2Ge2 (R = Ho, Er) compounds. Journal of Applied Physics 115, 073905. https://doi.org/10.1063/1.4864419

[101] Gschneidner, K.A., Pecharsky, V.K., Tsokol, A.O., 2005. Recent developments in magnetocaloric materials. Reports on Progress in Physics 68, 1479. https://doi.org/10.1088/0034-4885/68/6/R04

[102] Aray, Y., Rodriguez, J., Vega, D., 2002. An implementation of the atoms in molecules theory to the FPLAPW method. Computer Physics Communications 143, 199–212. https://doi.org/10.1016/S0010-4655(01)00428-3

[103] Gao, G.Y., Yao, K.L., Şaşıoğlu, E., Sandratskii, L.M., Liu, Z.L., Jiang, J.L., 2007. Half-metallic ferromagnetism in zinc-blende CaC , SrC , and BaC from first principles. Phys. Rev. B 75, 174442. https://doi.org/10.1103/PhysRevB.75.174442

[104] Perdew, J.P., Burke, K., Ernzerhof, M., 1996. Generalized Gradient Approximation Made Simple. Phys. Rev. Lett. 77, 3865–3868. https://doi.org/10.1103/PhysRevLett.77.3865

[105] Pinto, H., Melamud, M., Kuznietz, M., Shaked, H., 1985. Magnetic structures in the ternary RM 2 X 2 compounds (*R=Gd* to Tm; *M=Fe* , Co, Ni, or Cu; *X=Si* or Ge). Phys. Rev. B 31, 508–515. https://doi.org/10.1103/PhysRevB.31.508

[106] Baran, S., Bałanda, M., Gondek, Ł., Hoser, A., Nenkov, K., Penc, B., Szytuła, A., 2010. Nature of magnetic phase transitions in TbCu2X2 (X=Si, Ge) and HoCu2Si2 compounds. Journal of Alloys and Compounds 507, 16–20. https://doi.org/10.1016/j.jallcom.2010.07.167

[107] Paramanik, T., Das, K., Samanta, T., Das, I., 2015. Generation of magnetic phase diagram of HoRu2Si2 using magnetocaloric effect. Journal of Magnetism and Magnetic Materials 381, 168–172. https://doi.org/10.1016/j.jmmm.2014.12.080

[108] GKH. Madsen, and DJ. Singh, “BoltzTraP. A Code for Calculating Band-Structure Dependent Quantities,” *Comput Phys Commun*, **175** [1] 67-71 (2006).

[109] G. Kresse, and J. Furthmüller, “Efficiency of Ab-Initio Total Energy Calculations for Metals and Semiconductors Using a Plane-Wave Basis Set,” *Comput Mater Sci*, **6** [1] 15-50 (1996).

[110] G. Pizzi, D. Volja, B. Kozinsky, M. Fornari, and N. Marzari, “BoltzWann: A code for the Evaluation of Thermoelectric and Electronic Transport Properties with a

Maximally-Localized Wannier Functions Basis," *Comp Phys Comm*, **185** [1] 422-29 (2014).

[111] GS. Nolas, J. Sharp, and HJ. Goldsmid, Thermoelectrics: Basic Principles and New Materials Developments; Springer-Verlag, Heidelberg, (2001).

[112] MW. Oh, DM. Wee, SD. Park, BS. Kim, and HW. Lee, "Electronic Structure and Thermoelectric Transport Properties of AgTlTe: First-Principles Calculations," *Phys Rev B*, **77** [16] 165119(2008).

[113] W. Bazine, N. Tahiri, O. El Bounagui & H. Ez-Zahraouy (2022) Magnetic, magnetocaloric and thermoelectric properties of the intermetallic $LaMn_2Si_2$ compound: a theoretical study, Phase Transitions, 95:5, 387-397.

[114] Emre B, Aksoy S, Posth O, et al. Antiferromagnetic-ferromagnetic crossover in $La_{0.5}Pr_{0.5}Mn_2Si_2$ and its consequences on magnetoelastic and magnetocaloric properties. Phys. Rev. B. 2008;78:144408.

[115] Samanta T, Das I, Banerjee S. Giant magnetocaloric effect in antiferromagnetic $ErRu_2Si_2$ compound. Appl. Phys. Lett. 2007;91:152506.

[116] Kumar P, Suresh KG, Nigam AK, et al. Pressure-induced changes in the magnetic and magnetocaloric properties of RMn_2Ge_2 (R=Sm,Gd). Phys. Rev. B. 2008;77:224427.

[117] Wada H, Tanabe Y, Hagiwara K, et al. Magnetic phase transition and magnetocaloric effect of $DyMn_2Ge_2$. J. Magn. Magn. Mater. 2000;218:203-210.

[118] Lingwei L, Guanghui H, Umehara I, et al. Magnetic properties and magnetocaloric effect of $GdCr_2Si_2$ compound under hydrostatic pressure. J. Alloys Comp. 2013;575:1-4.

[119] Maji B, Ray MK, Suresh KG, et al. Large exchange bias and magnetocaloric effect in $TbMn_2Si_2$. J. Appl. Phys. 2014;116:213913.

[120] Mo ZJ, Shen J, Yan LQ, et al. Magnetic properties and magnetocaloric effect in the RCu_2Si_2 and RCu_2Ge_2 (R=Ho, Er) compounds. J. Appl. Phys. 2014;115:073905.

[121] Gerasimov EG, Kurkin, MI, Korolyov AV, et al. Magnetic anisotropy and ferro-antiferromagnetic phase transition in $LaMn_2Si_2$. Physica B: Condens. Matter. 2002;322:297-305.

[122] Di Napoli S, Bihlmayer G, Blügel S, et al. Noncollinear magnetism in $LaMn_2Ge_2$ and $LaMn_2Si_2$ compounds. J. Magn. Magn. Mater. 2004;272–276:E265-E266.

[123] Pandey S, Siruguri V, Rawat R. Effect of Tb substitution in naturally layered LaMn2Si2: magnetic, magnetocaloric, magnetoresistance and neutron diffraction study. J. Phys.: Condens. Matter. 2020;32:035807.

[124] Perdew JP, Burke K, Ernzerhof M. Generalized Gradient Approximation Made Simple. Phys. Rev. Lett. 1996;77:3865.

[125] Laskowski R, Blaha P. Magnetic structure and electric-field gradients of uranium dioxide: An ab initio study. Phys. Rev. B. 2004;69:140408.

[126] Sabi Takou D, Karimou M, Hontinfinde F, et al. Anisotropic Heisenberg model for the mixed spin-3/2 and spin-1/2 under random crystal field. Condens. Matter Phys. 2021;24:13704.

[127] Siberchicot B, Jobic S, Carteaux V, et al. Band Structure Calculations of Ferromagnetic Chromium Tellurides $CrSiTe_3$ and $CrGeTe_3$. J. Phys. Chem. 1996;100:5863-5867.

[128] Hofmann M, Campbell SJ, Kennedy, SJ, et al. A neutron diffraction study of $LaMn_2Si_2$ (10–473 K). J. Magn. Magn. Mater. 1997;176:279–287.

[129] Gschneidner Jr KA, Pecharsky VK, Tsokol AO. Recent developments in magnetocaloric materials. Prog. Phys. 2005;68:1479.

[130] Bhowmik TK. Observation of the magnetic criticality and the magnetocaloric effect in $LaMn_2Si_2$ in the vicinity of the phase transition around the room temperature. Phys. Lett. A. 2021;419:127724.

[131] Madsen GKH, Schwarz K, Singh D. BoltzTraP. A code for calculating band-structure dependent quantities. Comput. Phys. Comm. 2006;175:67-71.

[132] J. F. Scott, Nat Mater, 6 (2007) 256.

[133] N. A. Hill, Annual Review of Materials Research, 32 (2002) 1.

[134] A. A. Mukhin, A. M. Kuzmenko, V. Y. Ivanov, A. G. Pimenov, A. M. Shuvaev, V. E. Dziom, Physics-Uspekhi, 58 (2015) 993.

[135] C. A. F. Vaz , J. Phy. Cond. Matter, 24 (2012) 333201.

[136] S. Cheng, C. Bin, P. Jingjing, M. Haijun, P. Feng, Chinese Physics B, 25 (2016) 067502.

[137] A. H. MacDonald, M. Tsoi, Phil. Trans. R. Soc. A369 (2011) 3098.

[138] M. Kimata, H. Chen, K. Kondou, S. Sugimoto, P. K. Muduli, M. Ikhlas, Y. Omori, T. Tomita, A. H. MacDonald, S. Nakatsuji, Y. Otani, Nature 565 (2019) 627.

[139] E. Kren, and G. Kadar, Solid State Commun. 8 (1970)1653.

[140] G. J. Zimmer, and E. Kren, AIP Conf. Proc. 5 (1971) 513.

[141] G. Kadar, and E. Kren, Int. J. Magn. 1 (1971) 143.

[142] T. Ohoyama, K. Yasukochi, and K. Kanematsu, J. Phys.Soc. Japan 16 (1961) 352.

[143] B. Balke, G. H. Fecher, J. Winterlik, and C. Felser, Appl. Phys. Lett. 90 (2007) 152504.

[144] S. Tomiyoshi, and Y. Yamaguchi. J. Phys. Soc. Jpn. 51 (1982) 2478.

[145] J. Sticht, K. H. Höck, and J. Kübler, J. Phys. Condens. Matter 1 (1989) 8155.

[146] P. J. Brown, V. Nunez, F. Tasset, J. B. Forsyth, and P. Radhakrishna, J. Phys. Condens. Matter 2 (1990) 9409.

[147] Yang Cheng, Sisheng Yu, Menglin Zhu, Jinwoo Hwang, and Fengyuan Yang, APL Materials 9 (2021) 051121.

[148] Tomoya Higo, Huiyuan Man, Daniel B. Gopman, and Liang Wu, Nature Photonics 12 (2018) 73.

[149] S. Nakatsuji, N. Kiyohara, and T. Higo, Nature 527 (2015) 212.

[150] B. Nyári , A. Deák , and L. Szunyogh, Physical Review B 100 (2019) 144412.

[151] Taishi Chen, Takahiro Tomita, Susumu Minami, Mingxuan Fu, Takashi Koretsune, Motoharu Kitatani, Ikhlas Muhammad, Daisuke Nishio-Hamane, Rieko Ishii, Fumiyuki Ishii, Ryotaro Arita, and Satoru Nakatsuji. Nat Commun. 12 (2021) 572.

[152] X. Zhou, J.-P.Hanke, W. Feng, F. Li, G.-Y.Guo, Y. Yao, S. Blügel, and Y. Mokrousov, Phys. Rev. B 99 (2019) 104428.

[153] N. Kiyohara, T. Tomita, and S. Nakatsuji, Phys. Rev. Applied 5 (2016) 064009.

[154] A. K. Nayak, J. E. Fischer, Y. Sun, B. Yan, J. Karel, A. C. Komarek, C. Shekhar, N. Kumar, W. Schnelle, J. Kübler, C.Felser, and S. S. P. Parkin, Sci. Adv. 2 (2016) e1501870.

[155] W. Bazine, N. Tahiri, O. El Bounagui & H. Ez-Zahraouy (2022) Strain effect on physical properties of the multiferroic Mn_3Sn material: a first-principles calculations, Philosophical Magazine.

[156] H. J. Xiang, E. J. Kan, Su-Huai Wei, M.-H.Whangbo, and X. G. Gong, Phys. Rev. B 84 (2011) 224429.

[157] T. Nagamiya, S. Tomiyoshi, and Y. Yamaguchi, Solid State Commun. 42 (1982) 385.

[158] A. Markou, J. M. Taylor, A. Kalache, P. Werner, S. S. P. Parkin, and C. Felser. Phys. Rev. Materials 2 (2018) 051001.

[159] Z. Q. Liu, H. Chen, J. M. Wang, J. H. Liu, K. Wang, Z. X. Feng, H. Yan, X. R. Wang, C. B. Jiang, J. M. D. Coey, A. H. MacDonald, Nat. Electron 1 (2018) 172.

[160] A. Togo, F. Oba, and I. Tanaka, Phys. Rev. B 78 (2008) 134106.

[161] A. Togo and I. Tanaka, Scr. Mater. 108 (2015) 1.

[162] S. Baroni, S. de Gironcoli, A. Dal Corso, and P. Giannozzi, Rev. Mod. Phys. 73 (2001) 515.

[163] Y. C. Cheng, Z. Y. Zhu, M. Tahir, and U. Schwingenschlögl, Europhys. Lett.102 (2013) 57001.

[164] P. W. Anderson and E. I. Blount, Phys. Rev. Lett. 14 (1965) 217.

[165] Anna Delin, Optics Communications 167 (1999) 105.

[166] F. J. Kahn, P. S. Pershan, and J. P. Remeika, Phys. Rev. 186 (1969) 891.

[167] M. Seemann, D. Ködderitzsch, S.Wimmer, and H. Ebert, Phys. Rev. B 92 (2015) 155138.

[168] W. Feng, G. Y. Guo,J. Zhou, Y. Yao, Q. Niu, Phys. Rev. B 92 (2015)144426.

[169] M. Ikhlas, T. Tomita, T. Koretsune, M-To Suzuki, D. Nishio-Hamane, R. Arita, Y. Otani, S. Nakatsuji. Nat. Phys. 13 (2017) 1085.